Die approbierte Originalversion dieser Dissertation ist in der Hauptbibliothek der Technischen Universität Wien aufgestellt und zugänglich.
http://www.ub.tuwien.ac.at

The approved original version of this thesis is available at the main library of the Vienna University of Technology.
http://www.ub.tuwien.ac.at/eng

TECHNISCHE UNIVERSITÄT WIEN

FAKULTÄT FÜR ELEKTROTECHNIK UND INFORMATIONSTECHNIK

INSTITUT FÜR MIKROELEKTRONIK

Characterization of electrically active defects at III–N/dielectric interfaces

Dissertation ausgeführt zum Zwecke der Erlangung des akademischen Grades
einer Doktorin der technischen Wissenschaften

von

Roberta Stradiotto

Matrikelnummer: 1327715

unter der Anleitung von

Prof. Tibor Grasser

Dr. Gregor Pobegen

Villach, November 2016

TECHNISCHE UNIVERSITÄT WIEN

FACULTY OF ELECTRICAL ENGINEERING AND INFORMATION TECHNOLOGY

INSTITUTE FOR MICROELECTRONICS

Characterization of electrically active defects at III–N/dielectric interfaces

Dissertation submitted in partial fulfillment of the requirements for the degree of Doctor of Philosophy in Engineering Sciences

by

Roberta Stradiotto

in collaboration with

KAI GmbH - Kompetenzzentrum für Automobil- und Industrieelektronik in Villach, Austria

Infineon Technologies AG in Villach, Austria

under the supervision of

Prof. Tibor Grasser

Dr. Gregor Pobegen

Villach, November 2016

Contents

Abstract **i**

Kurzfassung **iii**

Acknowledgements **v**

1 Introduction **1**

1.1 Fundamentals 1

1.1.1 The GaN buffer: crystal structure, polarization, growth 2

1.1.2 The GaN/AlGaN interface: 2DEG creation, surface donor states 4

1.1.3 GaN–based devices: the high electron mobility transistor 6

1.2 Defects in GaN/AlGaN MIS–HEMTs 7

1.2.1 Reliability issues of GaN–based devices 7

1.2.2 Activation energy and thermodynamic energy level of defects 8

1.2.3 Bulk defects 11

1.2.4 Defects at the interface with a dielectric 12

1.3 Goal of this thesis 17

2 Experimental aspects **19**

2.1 Sample preparation 19

2.2 Measurement setup 21

2.3 Fast measurement with a lock–in amplifier 23

2.3.1 Functional description 23

2.3.2 Impedance measurement 25

2.3.3 Sampling measurement 27

2.4 Setup for opto–electrical characterization 29

2.4.1 Light source 29

2.4.2 Monochromator 30

2.4.3 Light transmission 32

2.4.4 Light intensity 34

3 Methodologies for electrical characterization of interface defects in GaN–based MIS–HEMTs **37**
3.1 The main established methods and their limitations 37
3.1.1 The equivalent circuit model 38
3.1.2 The Terman or high frequency method 41
3.1.3 The conductance method 46
3.2 Impedance characteristics of GaN/AlGaN MIS structures 50
3.2.1 The role of the AlGaN barrier 50
3.2.2 Dependence on measurement parameters 52
3.3 Voltage shift methods 57
3.3.1 The measurement–stress–measurement (MSM) method 58
3.3.2 The capacitance–on-the-fly (C–OTF) method 60

4 Modeling of charge trapping phenomena **65**
4.1 The Shockley–Read–Hall (SRH) model 65
4.2 The non–radiative multiphonon (NMP) model 67
4.2.1 Constant τ_0, single activation energy 69
4.2.2 Constant τ_0, distributed activation energy 70
4.2.3 Non–constant τ_0 71
4.3 Extraction of the activation energy and τ_0 from experimental data 73
4.3.1 Extracting single–valued activation energies 74
4.3.2 Extracting distributed activation energies 75
4.3.3 Effects of a non–constant τ_0 77

5 Electrical characterization of interface defects in GaN–based MIS–HEMTs **81**
5.1 Results on devices with standard interface 81
5.1.1 Comparison of experimental methods 82
5.1.2 Effect of forward gate bias stress 84
5.1.3 Evaluation of the interface trap density 86
5.2 Results on devices with fluorinated interfaces 87
5.2.1 Effect of fluorination on device behavior 88
5.2.2 Evaluation of the interface trap density 91

6 Opto–electrical characterization of defects **95**
6.1 Effect of light on GaN/AlGaN test structures 95
6.1.1 The DLOS experiment 95
6.1.2 C and Mg impurities characterized with O–DLTS 98
6.2 Effect of light on MIS structures 99
6.2.1 Exposed CV characteristics of SiC devices 99

6.2.2 Exposed CV characteristics of GaN devices 101
6.3 Effect of light on GaN/AlGaN MIS–HEMTs 102
6.3.1 DLOS on standard MIS–HEMTs 102
6.3.2 Thin gold contacts on MIS–HEMTs for optical characterization 103
6.3.3 DLOS on MIS–HEMTs with thin gold contacts 105

7 Conclusions **109**

Bibliography **111**

Curriculum Vitae **121**

Abstract

WIDE BANDGAP SEMICONDUCTORS have recently attracted the interest of academic researchers and the semiconductor industry. In fact, their superior material parameters with respect to silicon allow for a series of significant improvements. In particular, composite GaN/AlGaN semiconductors offer a large breakdown field and a good thermal conductivity together with a high electron mobility, for which they have become the best candidates for power electronics and high frequency switching applications. Possible targets that would benefit of the advantages of GaN–based devices include efficient power supplies, DC/DC converters and AC/DC adapters, as well as the field of radars and telecommunications.

Nevertheless, several issues still constitute a challenge to the development of a mature GaN–based technology. Besides the difficulties of growing a high–quality GaN material, point defects at interfaces play a major role in terms of reliability. In the present thesis, we investigate the threshold voltage instability under forward gate bias of GaN–based transistors, which is due to the defects located at the III–N/dielectric interface. Our goal is to characterize these trap levels and propose a valid physical model to explain the behavior observed on our test structures. We perform electrical measurements as well as a combination of electrical and optical experiments, by integrating an existing setup with a system capable of exposing the device under test to monochromatic light.

The main results of this work are the development of characterization methods and their application to various GaN/AlGaN/SiN transistors. In the first place, we find that most of the established characterization techniques for interface traps, particularly those based on the analysis of the impedance characteristics, are inappropriate for GaN/AlGaN devices. As a consequence, we develop an experimental method that allows to evaluate the amount of threshold voltage shift during the application of a positive gate bias stress accurately and precisely. The data measured in this way is interpreted according to a physical model for charge exchange based on non–radiative multiphonon transitions. The experimental results show that the standard AlGaN/SiN interface has a density of traps per unit area and energy of about 10^{13} cm^{-2} eV^{-1}, and the activation energy for electron trapping at these defects is distributed at least from 0.1 eV to 0.8 eV. This can be explained with the disordered nature of the AlGaN/SiN

interface. On the other hand, a completely different trapping behavior is observed in devices whose AlGaN surface has been cleaned with a fluorine plasma process before the deposition of the dielectric. In this case, we find defects with a very narrow distribution of activation energy around 0.32 eV, and a density of 8×10^{13} cm^{-2} eV^{-1}. This result implies that the fluorine radical plays an active role in the passivation of the native defects, substituting them with a new trap level having very different properties.

Kurzfassung

HALBLEITER MIT BREITER BANDLÜCKE haben in den letzten Jahren verstärkt das Interesse der Halbleiterindustrie wie auch der angewandten Forschung auf sich gezogen. Aufgrund ihrer theoretisch überlegenen Materialeigenschaften gegenüber Silizium erlauben sie eine Verbesserung der Eigenschaften der daraus gefertigten Bauelemente. Die Zusammensetzung von Galliumnitrid (GaN) und Aluminiumgalliumnitrid (AlGaN) erlaubt einerseits eine hohe Durchbruchsspannung und eine gute thermische Leitfähigkeit und andererseits eine ausgezeichnete Elektronenbeweglichkeit. Diese einzigartige Kombination macht GaN/AlGaN zu einem bestens geeigneten Materialsystem für Leistungselektronik- und Hochfrequenzanwendungen wie z.B. Schaltnetzteile, Radar und Datenübertragung.

Zur vollständigen Ausschöpfung der Qualitäten des Halbleiters müssen aber noch einige Herausforderungen bewältigt werden. Neben den Problematiken die sich aus der Qualität des GaN Grundmaterials ergibt, spielen Defekte an der Grenzfläche zu Dielektrika eine entscheidende Rolle. In dieser Arbeit wird die Instabilität der Einsatzspannung unter Spannungsbelastung von GaN Transistoren näher untersucht. Diese Instabilität hat ihren Ursprung in der elektrischen Beladung von elektrisch aktiven Defekten an der GaN/Dielektrikum Grenzfläche. Das konkrete Ziel dieser Arbeit ist die adäquate Messung sowie die Entwicklung eines physikalischen Modells für die beobachteten Ladungsaustauschphänomene. Verwendet wurden dabei elektrische sowie optische Messverfahren, wobei ein vorhandener Versuchsaufbau um eine monochromatische Lichtquelle erweitert wurde.

Das zentrale Ergebnis der vorliegenden Arbeit ist die vollständige Entwicklung von geeigneten Charakterisierungsmethoden sowie deren Anwendung auf GaN/AlGaN/SiN Transistoren. Zuerst wurden etablierte Messmethoden zur Charakterisierung von Grenzflächenzuständen basierend auf Impedanzmessungen als nicht geeignet für GaN basierte Bauelemente identifiziert. Aus diesem Grund wurde eine experimentelle Methode entwickelt, welche die Grenzflächenzustandsdichte während der Belastung mit hoher Genauigkeit bestimmt. Die so gewonnenen Daten werden im Rahmen eines Modells interpretiert, welches Ladungstransferprozesse mit nicht strahlenden ubergangen berücksichtigt. Die experimentellen Ergebnisse zeigen, dass AlGaN/SiN Grenzfläche eine Defektdichte im Bereich von $10^{13}\,\mathrm{cm}^{-2}\,\mathrm{eV}^{-1}$ hat und die Aktivierungsenergie für den Elektroneneinfang zumindest zwischen 0.1 eV und 0.8 eV ver-

teilt ist. Der mikroskopische Ursprung dieser breiten Verteilung ist mutmasslich auf die unregelmässige atomare Struktur der Grenzfläche zurückzuführen. Jedoch kann die Grenzfläche fundamental durch eine spezielle Reinigung der AlGaN Oberfläche mit Fluor vor dem Abscheiden des Dielektrikums verändert werden. In einem so präparierten Bauelement sind dann nur noch eine Art von Defekten zu messen, welche eine schmale Verteilung der Aktivierungsenergien um 0.32 eV und eine Dichte von $8 \times 10^{13}\,\mathrm{cm}^{-2}\,\mathrm{eV}^{-1}$ besitzen. Dies verdeutlicht, dass das Fluor Radikal eine wichtige Rolle in der Passivierung der nativen Defekte an der AlGaN Oberfläche hat und eine neue elektrisch aktive Störstelle verursacht die komplett andere Eigenschaften besitzt.

Acknowledgement

I WOULD LIKE to sincerely thank my supervisors at KAI GmbH and at Infineon Technologies, Gregor Pobegen and Clemens Ostermaier, as well as my academic supervisor Tibor Grasser of the Microelectronics Institute at the TU Wien for the constant support, motivation and the fruitful discussions during the entire duration of my doctoral project. Your competence and your enthusiasm have guided me throughout my research experience, from the establishment of the experimental setup to the realization of this doctoral thesis. I wish to thank also Prof. Gaudenzio Meneghesso of University of Padova for being part of the examination committee.

I thank the colleagues at KAI GmbH, Infineon Technologies and the Vienna University of Technology for being always friendly and helpful, for giving me precious suggestions and for being open to exchange ideas and different point of views.

Last but not least, I am very grateful to my partner Marco, to my family and to all the friends who have always been taking care of me and supported me in many ways.

VORREI ringraziare di cuore i miei supervisori al KAI GmbH e ad Infineon Technologies, Gregor Pobegen e Clemens Ostermaier, ed anche il mio supervisore accademico Tibor Grasser dell'Istituto di Microelettronica dell'Università Tecnica di Vienna per il costante sostegno, l'incessante motivazione e per le interessanti discussioni tenute durante l'intero corso della mio progetto di dottorato. La vostra competenza e il vostro entusiasmo mi hanno guidata attraverso la mia esperienza di ricerca, dal lavoro in laboratorio alla realizzazione di questa tesi di dottorato. Sono grata anche al Prof. Gaudenzio Meneghesso, che ha accettato di fare parte della commissione d'esame.

Ringrazio i colleghi del KAI GmbH, di Infineon Technologies e dell'Università Tecnica di Vienna per riuscire sempre a creare un ambiente amichevole e costruttivo. Grazie per tutti i suggerimenti che mi avete dato, e per essere sempre disponibili a scambiare opinioni e punti di vista differenti.

Infine, vorrei esprimere tutta la mia gratitudine al mio partner, Marco, alla mia famiglia e a tutti gli amici che mi sono stati accanto, dandomi tutto il supporto di cui ho avuto bisogno.

Ich erkläre hiermit an Eides statt, dass ich die vorliegende Arbeit selbständig sowie ohne unzulässige Hilfe Dritter und ohne Benutzung anderer als der angegebenen Hilfsmittel angefertigt habe. Die aus anderen Quellen direkt oder indirekt übernommenen Daten und Konzepte sind unter Angabe der Quelle gekennzeichnet.

I hereby declare that I have written the present thesis independently, without assistance from external parties and without use of other resources than those indicated. The ideas taken directly or indirectly from external sources (including electronic sources) are acknowledged in the text.

Villach, November 2016

This work was jointly funded by the Austrian Research Promotion Agency (FFG, Project No. 854247) and the Carinthian Economic Promotion Fund (KWF, contract KWF-1521|28101|40388).

1

Introduction

THIS CHAPTER is dedicated to lay the foundation for the present work. We start with a review of the GaN–based devices properties, from the advantages in power applications to the physical working principles of the high electron mobility transistor (HEMT). We also present a brief summary on device fabrication and its challenges. Then we focus on the effect of defects, in particular those arising at the interface with the dielectric in composite metal–insulator–semiconductor (MIS) HEMTs. Finally, we determine the objective of the present work and we give an overview of how the thesis is organized throughout the following chapters.

1.1 Fundamentals

Wide bandgap semiconductors have become one of the main research subjects of the semiconductor industry in the past years. In particular, GaN and SiC are today the best candidates to substitute silicon in certain applications because of their superior material parameters, as we can see from Table 1.1.

		Si	SiC	GaN
E_g	in eV	1.1	3.2	3.4
$\mathscr{E}_{BD}$	in $MV\,cm^{-1}$	0.3	3	3.3
Θ	in $W\,cm^{-1}\,K^{-1}$	1.5	3.3	1.3
v_{sat}	in $10^7\,cm\,s^{-1}$	1	2	2.5*
μ	in $cm\,s^{-1}$	1350	600	2000*

*Table 1.1. Comparison of some material parameters for silicon, four–layer hexagonal (4H) SiC and GaN (from [1]). The values marked with * are for a composite GaN/AlGaN structure.*

In the first place, a large bandgap results in a high breakdown electric field $\mathscr{E}_{\mathrm{BD}}$, thus allowing higher operating voltages than silicon. Together with a good thermal conductivity Θ, this is a clear advantage for power applications as power supplies, DC/DC converters and AC/DC adapters [2].

Furthermore, composite GaN/AlGaN devices can achieve high intrinsic speed because of the large saturation velocity v_{sat} combined with an excellent electron mobility μ. As a consequence, their performance in terms of operating frequency is superior to both silicon and GaAs. This opens a series of opportunities in the field of RF electronics, like telecommunications and radar applications [3].

In the rest of this section we discuss in detail the properties of the material, the advantages of GaN/AlGaN heterostructures and the fundamental characteristics of GaN–based devices.

1.1.1 The GaN buffer: crystal structure, polarization, growth

All group–III nitrides like GaN can crystallize in three structures: zincblende, rocksalt and wurtzite, the latter being thermodynamically stable at ambient temperatures [4, 5]. The GaN wafers used in this thesis have a wurtzite structure. The unit cell is hexagonal and it consists of two interpenetrating hexagonal closed packed sublattices, as shown in Fig. 1.1. The first sublattice is formed by the cations, and the other by the anions. Their spatial separation along the vertical c axis results in a spontaneous polarization field in this direction.

The GaN buffer is usually grown using metal–organic chemical vapor deposition (MOCVD) or molecular beam epitaxy (MBE) on different kinds of substrates: sapphire, silicon carbide and silicon. All these materials have different lattice constants and thermal expansion coefficients compared to GaN, and this can cause strong strain effects in the GaN bulk. The best match

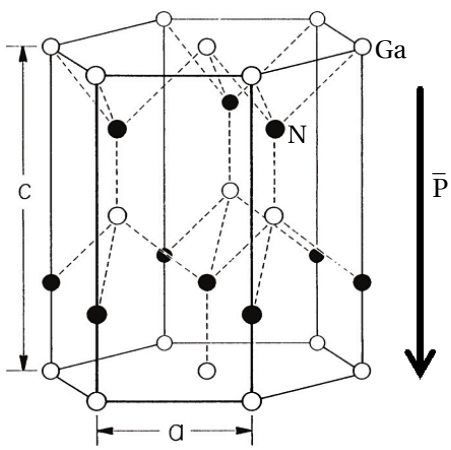

Figure 1.1. The wurtzite crystal structure of GaN and alloys like AlGaN. The distance between the cation and anion sublattice results in a spontaneous polarization field along the c axis. (Illustration adapted from [6].)

in this sense is 6H–SiC (3.5% lattice mismatch), which furthermore offers an excellent thermal conductivity, possibly allowing an efficient heat dissipation for power devices. However, the very high price limits the use of this substrate, in favor of the cheaper and widely available silicon (17% lattice mismatch). In fact, a 2–inches SiC wafer can cost up to 500$, while a Si wafer with the same dimensions costs between 20$ and 50$, depending on the doping [7]. Silicon wafers are fabricated in a wide range of sizes and are already in use in semiconductor industries. In this way, the implementation of GaN devices on a Si substrate would benefit from all the existing facilities and processing environments, and the integration of GaN structures on silicon chips would be possible as well.

Still, one of the main challenges for GaN–based device fabrication is to grow a high–quality GaN buffer. In fact, the first epilayer grown on any substrate contains a large concentration of dislocations, clearly visible in transmission electron microscope (TEM) cross-sections [5]. The dislocation density decreases in the layer above this region, where the GaN continues to grow in a columnar fashion. An image of a GaN sample surface is shown in Fig. 1.2a. The columns develop along the *c* direction, displaying some relative twist and tilt (illustrated in Fig. 1.2b), until in the top part of the film the structure becomes more ordered. The quality of the GaN bulk depends on the growth parameters as temperature, pressure as well as the thickness of the nucleation layer. This influences the density of threading dislocations and other defects in the buffer, which can be electrically relevant during device operation.

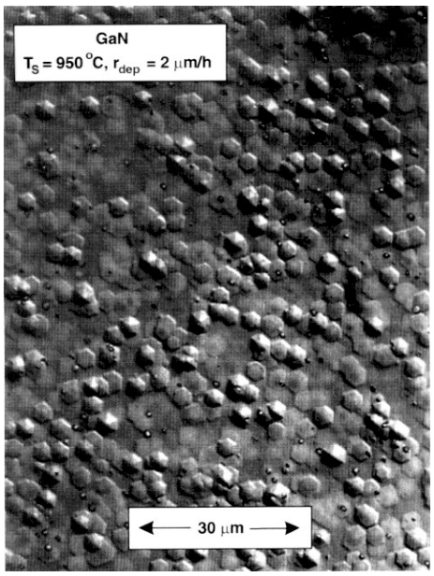

(a)

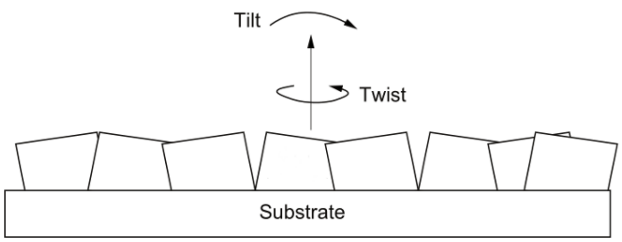

(b)

Figure 1.2. (a) Optical microscope image of the surface of a MOCVD grown sample. A mosaic structure of hexagonal crystals of about 3 μm is clearly visible (from [4]). (b) Schematic illustration of the GaN columnar growth (from [5]).

1.1.2 The GaN/AlGaN interface: 2DEG creation, surface donor states

In an AlGaN alloy, some of the gallium atoms are substituted by aluminum. Since the sizes of these two atoms are different, the lattice constant a of the AlGaN crystal structure is smaller than that of GaN. In fact, in GaN $a = 3.19$ Å while for AlN $a = 3.11$ Å [2]. The AlGaN lattice constant takes a value in between, depending on the aluminum content. For this reason, a thin AlGaN layer grown on a thick GaN layer is subject to a certain amount of tensile strain. As a consequence of the crystal structure stretch, a piezoelectric polarization field is created, which sums up to the spontaneous polarization of the AlGaN layer. The discontinuity of the polarization field at the GaN/AlGaN interfaces results in the creation of a two–dimensional sheet of charge, the *two–dimensional electron gas* (2DEG). The band diagram of such a heterostructure is shown in Fig. 1.3. The polarization fields cause a large discontinuity at the GaN/AlGaN interface, pushing the conduction edge below the Fermi level. In this way, a triangular quantum well is formed. Here, electrons must have discrete energy values along the c direction, therefore their motion is confined to a two–dimensional plane parallel to the interface.

The thin AlGaN layer can accommodate the lattice mismatch by tensile strain up to a certain maximum thickness. For example, the critical thickness is 80 nm for an AlGaN layer with 20% of aluminum, and it decreases to 10 nm for 60% aluminum content [9]. Above this value the strain cannot be sustained anymore and the material relaxes, going back to its original lattice constant. This results in the creation of dislocations, compromising the material qua-

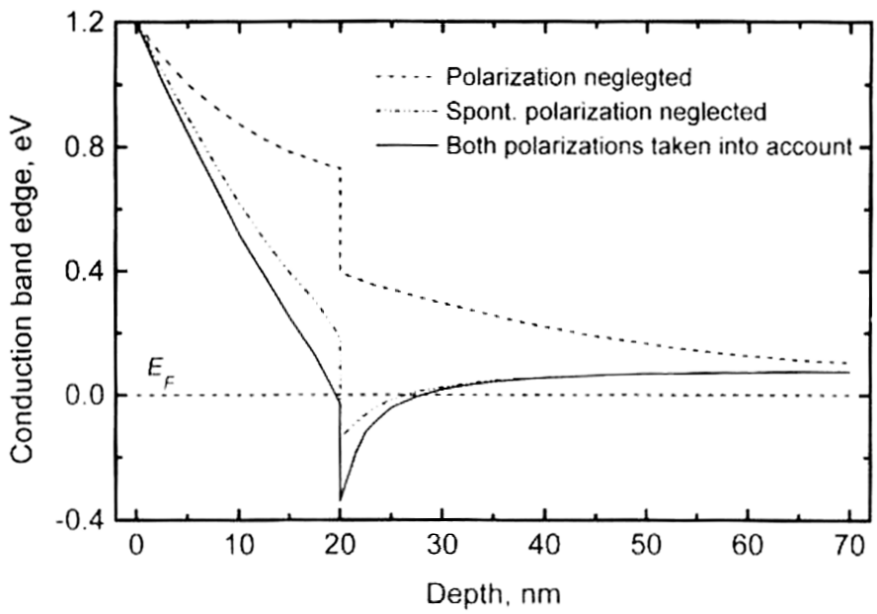

Figure 1.3. Calculated conduction band edge diagram, neglecting or considering the spontaneous and piezoelectric polarizations. The structure consists of an AlGaN layer of 20 nm above a 50 nm thick GaN buffer (from [8]).

lity. The critical thickness depends on the aluminum content: the higher the percentage, the smaller the thickness of the layer which can tolerate the lattice mismatch.

The electron gas at the GaN/AlGaN interface offers very high electron density (about 2×10^{13} cm^{-2}) and mobility (2000 $cm\,s^{-1}$) with no intentional doping, qualities that have attracted the interest of semiconductor device manufacturers and many research groups. Nevertheless, the exact origin of the 2DEG is not yet completely understood. The polarization charges at the GaN/AlGaN interface and at the AlGaN surface constitute a dipole, whose net charge must be zero. Because of the nature of polarization charges, they cannot be the source of the free electrons in the 2DEG, which must therefore be found elsewhere. The currently most accepted model is the *surface donor state* model, introduced by Ibbetson at al. [10]. In this picture, donor states at the AlGaN surface are considered the source of electrons for the 2DEG. These states would be energetically located inside the AlGaN bandgap, and would contribute to the electron gas when they rise above the Fermi level. On the contrary, if they are below the Fermi level, there are no electrons at the GaN/AlGaN interface. Since the electric field throughout the AlGaN layer remains constant, by changing the AlGaN layer thickness the position of the surface state with respect to the Fermi level changes as well. This is illustrated in Fig. 1.4a and b. This is confirmed by experiments, as shown in Fig. 1.4c: below a certain critical thickness, no electron gas is formed.

In conclusion, the AlGaN layer must be thick enough in order to allow the existence of the electron gas, but beyond a certain thickness the material would relax and develop many defects like dislocations. Therefore a trade–off between these two limits must be found. In this thesis we use structures with an AlGaN layer thickness between 20 and 30 nm.

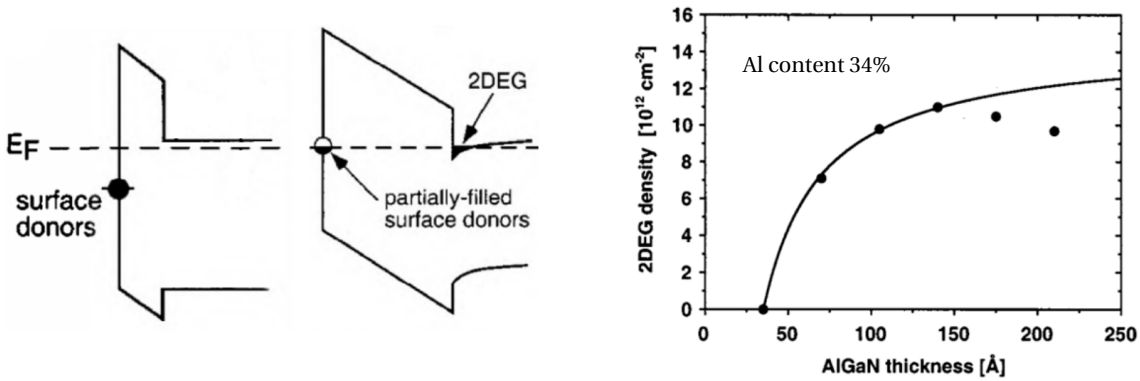

(a) (b) (c)

Figure 1.4. The donor state model: the surface states are neutral below the Fermi level (a) and positively charged when above (b). The AlGaN thickness determines the position of the donors with respect to the Fermi level. This explains the critical thickness observed in experimental data (c): solid markers are measured data and the line is calculated from the model (from [10]).

1.1.3 GaN–based devices: the high electron mobility transistor

The two–dimensional electron gas originated at the GaN/AlGaN interface can be used for the fabrication of field effect transistors (FETs). This type of device is a heterojunction FET (HFET) and it is usually called *high electron mobility transistor* (HEMT), because of the high mobility achieved by the electrons in the 2DEG.

Two ohmic contacts are in direct connection with the 2DEG, which therefore constitutes the channel between source and drain. The top gate contact can be realized directly above the AlGaN as a Schottky contact (HEMT device), or with a dielectric layer in between (MIS–HEMT device). In both cases this contact regulates the flow of the electrons in the channel, from the full saturation current down to zero, when the 2DEG is depleted. The insertion of the dielectric allows to suppress the parasitic leakage currents through the gate stack [11]. The structure of an insulated gate HEMT (MIS–HEMT) is schematically shown in Fig. 1.5.

Since the channel is formed as a consequence of the polarization properties of the heterojunction, these devices are *normally on*. This means that they must be turned off by the application of a negative gate voltage. Especially in power applications, transistors with normally off characteristics are preferred. The reasons include safety during operation at high voltage or high power densities, lower driving power consumption and compatibility with existing driving circuits. Several modified device design concepts and processes during fabrication allow to push the threshold voltage to positive values, for example fluorine implantation [12], the use of p–type GaN for the gate contact [13] or the recess of the Schottky gate [14]. As an alternative, normally on transistors can be used in cascode configuration [15].

In this work we use normally on MIS–HEMTs in order to investigate the defects at the AlGaN/dielectric interface and their contribution to device degradation through charge trapping. In this way we keep the complexity of the structures to a minimum and we focus on the properties of interface states inherent to the system.

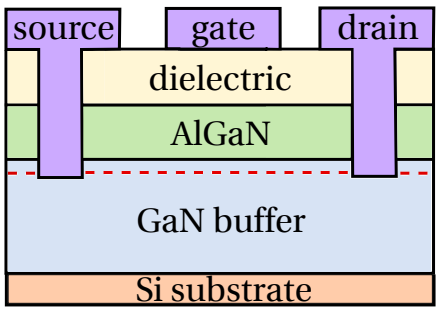

Figure 1.5. Schematic illustration of a MIS–HEMT structure.

1.2 Defects in GaN/AlGaN MIS–HEMTs

The first GaN–based devices are nowadays available on the market, however there is still a number of issues to be investigated in order to achieve a comprehensive understanding of all their failure mechanisms. In particular, reliability is a major concern, as charge trapping phenomena result in severe drift effects.

In the following, we introduce the most important reliability issues for GaN–based HEMT and MIS–HEMT structures, and then we focus on the two main areas where defects play a role for the device degradation: bulk defects and interface states, giving an overview of the state–of–the–art.

1.2.1 Reliability issues of GaN–based devices

The main problem of GaN–based devices today is to guarantee high–performance during operation together with a high level of stability, especially in their dynamic response. The primary cause is to be found in charge trapping phenomena.

One of the major issues is the *current collapse* effect, i.e., the recoverable decrease of the drain current during operation, after a gate or drain voltage change [16, 17]. An example is shown in Fig. 1.6a. This phenomenon is studied by performing single– or double–pulsed drain current measurements, during which the drain current is monitored in on state after the application of a stress transient, usually in off state [18, 19]. The analysis of the time evolution of the drain current during recovery allows to extract some properties of the defects responsible for charge trapping.

Trapping of 2DEG electrons can take place at different locations within the device structure. One possibility is at or below the gate stack, which means charge injection in the substrate, or trapping in the AlGaN layer or the GaN buffer. Even though the material quality has been con-

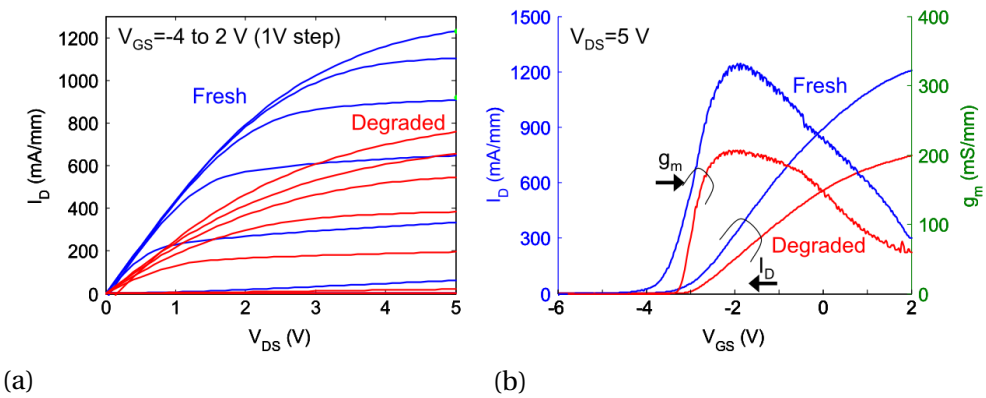

(a) (b)

Figure 1.6. Degradation of the drain current over drain voltage (a) and over gate voltage (b) after a stress transient where the gate bias is stepped from −10 to −50 V, at a drain bias of 0 V. A comparison with fresh device output (a) and transfer characteristics (b) is shown (from [16]).

stantly improving over the years, the main source of defects is still the GaN substrate, namely the deeper GaN layers. The reason is the need for a progressive change in lattice constant because of the non–native substrate (in our case, silicon), which leads to dislocations in the bulk material, or the use of dopants which may act like charge trapping sites as well. This results in as a negative drift of the threshold voltage after stress in off state (at negative gate biases), which causes the whole transfer characteristic to shift towards more negative values of gate bias [20].

Another effect related to the current collapse is the degradation of the dynamic on–resistance, also visible as g_m transconductance reduction (Fig. 1.6b). This can be due to charge trapping at the surface in the access region [21], because of defects at the surface or close to the passivation layer [22]. Another phenomenon responsible for the reduction of on–resistance is hot electron degradation. This happens when the drain voltage is high and very large electric fields are present. Hot electrons can generate traps in the access region, thus damaging the material structure and leading to the degradation of the electron mobility [17]. Since the on–resistance is the most critical parameter for switching applications, further investigations aimed to understand and reduce this problem are of primary importance [23].

A further source of degradation can be due to the piezoelectric qualities of GaN and AlGaN. If a large electric field is applied, the material would experience a certain amount of stress. This may eventually lead to the formation of electrically active crystallographic defects [16].

Finally, device breakdown can occur as a consequence of defect generation under large electric fields. If the density of defects rises so much to form a percolation path, conduction takes place primarily along this conductive way. This leads to catastrophic gate leakage current in the case of vertical breakdown of a GaN HEMT, or to current flowing out of the source terminal if the percolation path is formed between drain and source [23]. Investigations over a large number of Schottky devices show that the time dependence of gate breakdown follows a Weibull distribution [24].

1.2.2 Activation energy and thermodynamic energy level of defects

At this point, it is necessary to introduce some physical concepts about charge exchange mechanisms, and to define the activation energy of a defect for trapping and detrapping events. Depending on the model and the degree of simplification used, the activation energy can be defined in different ways. Unfortunately, this might lead to a misinterpretation of its physical meaning. For this reason, we present here briefly the non–radiative, multiphonon model for charge exchange, in contrast to the Shockley–Read–Hall (SRH) theory. Both models are discussed in more detail in Chapter 4.

The trapping (or detrapping) of an electron (or hole) results in the change of the charge state of a defect site present in the device under test. The transition between two charge states corresponds to a transition between two different configurations of the defect. Each configuration is defined by a certain equilibrium position of the atoms constituting the defect, which

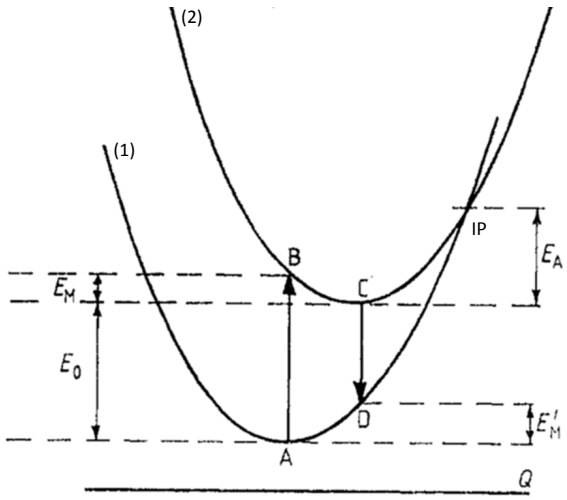

Figure 1.7. Illustration of a two–level system, for example a defect site that can be empty (1) or filled (2). Some possible transitions are indicated: the direct transition from 1 to 2 through optical energy absorption (A to B) and the transition from 2 to 1 with emission of optical energy during photoluminescence (C to D). The non–radiative, multiphonon transition between the two states takes place through the intersection point, IP (adapted from [25]).

is given by the result of all the quantum–mechanical repulsive and attractive forces. Furthermore, in the Born–Oppenheimer approximation the atoms vibrate around their equilibrium positions depending on the temperature. We can therefore describe each status of the system, for example an empty and a filled trap level, as harmonic oscillators along a certain reaction coordinate Q, as shown in Fig. 1.7 [25]. The equilibrium energy and the coordinate Q of the two configurations of the defect are different: in fact, the spatial arrangement of the atoms constituting the trap site changes according to its charge state, since the bonds to the captured or emitted electron must be created or destroyed. The difference between the minimum of the two parabolas is called the zero phonon energy, E_0. However, in order to make the transition possible, some excess energy must be supplied to the system. The absorption of optical energy results in vertical transitions in the diagram of Fig. 1.7, according to the Franck–Condon principle [26]. Therefore, an amount of optical energy equal to $E_0 + E_M$ is necessary for the transition from state 1 to state 2. The difference with E_0 is the relaxation energy E_M, also called Franck–Condon shift. It can be expressed as the product of the Huang–Rhys factor S_0 and the effective phonon energy $\hbar\omega$: $E_M = S_0\,\hbar\omega$. Furthermore, the energy $E_t^{opt} = E_0 - E_M{}'$ is released during the transition from 2 to 1 with a photoluminescence experiment. On the other hand, in absence of electromagnetic radiation the transition between the two states is mediated by phonons. For this reason, in a semi–classical approximation a non–radiative multiphonon (NMP) transition must take place through the intersection point (IP). In this way, the activation energy for the transitions between the two configurations is defined. For example, a transition from state 2 to 1 in Fig. 1.7 requires the activation energy E_A to be provided by phonons.

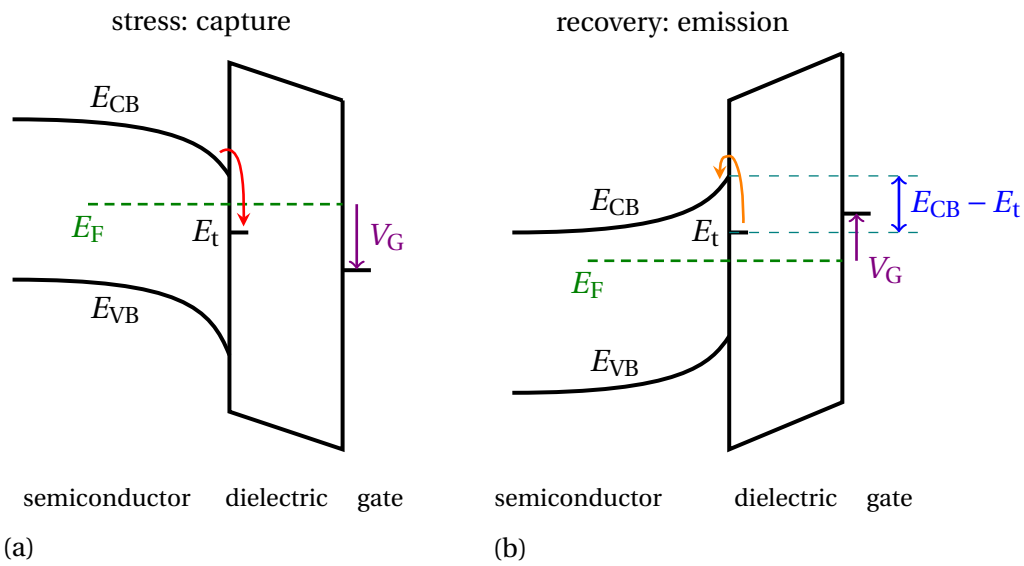

Figure 1.8. Illustration of the thermodynamic energy level of a defect acting as an acceptor trap level, E_t, at the interface between the semiconductor and the dielectric in a MIS structure during accumulation (a) and depletion (b). According to the SRH model, the energy $E_{CB} - E_t$ alone defines the activation energy for charge exchange.

Another important concept is the thermodynamic energy level of a trap state, E_t, namely its position inside the semiconductor (or dielectric) bandgap, as shown in Fig. 1.8. In this way we can determine the position of the defect relative to the Fermi level, E_F. If E_t lays below E_F, then an electron can be trapped (or a hole emitted). On the contrary, if $E_t > E_F$ an electron can be emitted (or a hole trapped). However, according to the SRH model the thermodynamic energy defines the activation energy for capture and emission as well. As shown in Fig. 1.8 in the case of electrons, there is an energy barrier only for emission, given by the difference between E_t and the edge of the conduction band, E_{CB}. In addition to other limitations that are discussed in Chapters 3 and 4, the SRH picture implies that "shallow" states, i.e., defects located close to the conduction band, must have a small activation energy, while "deep" states, located far from E_{CB}, must have a large E_A. On the contrary, experimental evidence has proven the existence of "shallow" trap states in silicon MOSFETs, responsible for negative bias temperature instability (NBTI), with very large activation energy [27].

In the following sections and in the rest of the thesis, we use the definition of activation energy derived from the NMP theory. In the case of electrical measurements, the activation energy is E_A, the difference between the equilibrium energy of the initial state and that at the intersection point. On the other hand, the activation energy measured with experimental techniques involving light absorption, like the deep level optical spectroscopy (DLOS), is the optical activation energy E_t^{opt}.

1.2.3 Bulk defects

The need for a foreign substrate to grow the GaN buffer impacts the material quality, leading to dislocations, vacancies and other lattice irregularities. In addition, impurities like carbon and oxygen are usually found in the GaN bulk, as they are incorporated during growth [28]. For this reason we talk about *unintentionally doped* (UID) GaN. In particular, carbon is an amphoteric dopant (i.e., it can act both as a donor or as an acceptor) that can substitute one nitrogen atom (C_N) in n–type GaN, or a gallium atom (C_{Ga}) in p–type GaN [29, 30].

Some of these defects have been simulated with *ab initio* calculations, as well as investigated with a number of experimental techniques. Electronic structure and formation energies of the defects can be obtained with quantum molecular dynamics and the density functional theory approach [29, 31], that allow to draw a picture of the possible configurations when one atom is missing, or the probability for dopants to substitute a Ga or N atom. These values can then be compared with experimental results. Among the numerous possible experimental techniques we find luminescence investigations [30] or scanning capacitance microscopy, a technique based on contact mode atomic force microscopy (AFM) [28]. However, the most important and widely used methods are deep level transient spectroscopy (DLTS) [32], and its variation including optical excitation known as deep level optical spectroscopy (DLOS) [33]. While DLTS investigations allow to excite defects with activation energies up to 1 or 1.5 eV, monochromatic light can access states with activation energies in the order of the semiconductor bandgap (for GaN, E_g =3.39 eV, equivalent to ultraviolet radiation at 365 nm).

A number of studies have been carried out on bulk materials (GaN and AlGaN with various aluminum content and grown in different ways) and on fully–processed devices. While some defects have been identified, for other observed energy levels the root cause is still unknown, or more than one possible candidate has been suggested.

Several defect levels have been measured in bulk GaN by various authors [20]. We summarize the most important for the present work in Table 1.2. The levels with relatively small activation energies have been related to defects intrinsic in the material, or caused by common impurities like carbon and oxygen [36, 37]. The 2.6 eV level has been measured by many research groups, which agree in identifying its root cause as a gallium vacancy, V_{Ga}, or a complex of one V_{Ga} with one or two hydrogen atoms [34]. The 3.22 eV and 3.28 eV defects are typical of the MOCVD and of the MBE growth methods, respectively [35]. The difference here is the dominant acceptor level, which is Mg in MOCVD and C in MBE. Therefore, the two activation energies can be associated with the respective dopant.

Bulk AlGaN samples show some other typical energy level, like the 3.11 eV cation (gallium in GaN, Al or Ga in AlGaN) vacancy and the 3.9 eV magnesium or carbon substitutional defect [34, 37]. We note that the same type of defect has a different activation energy when it is found in the GaN bulk or in the AlGaN layer [35].

Activation energy	Samples	Interpretation(s)
0.25 eV	GaN	N vacancy
0.6 eV	GaN, GaN/AlGaN HEMT	V_{Ga}–O complex, N vacancy, N antisite
0.9 eV	GaN	N interstitial, gallium vacancy
1.28–1.35 eV	GaN	C interstitial
2.3 eV	GaN/AlGaN HEMT	in the gate stack
2.6 eV	GaN	gallium vacancy, V_{Ga}–H or V_{Ga}–2H complex
3.11 eV	AlGaN	gallium vacancy
3.22 eV	GaN, GaN/AlGaN HEMT	Mg_N substitutional
3.28–3.3 eV	GaN, GaN/AlGaN HEMT	C_N substitutional
3.7 eV	GaN/AlGaN HEMT	Mg or C substitutional in AlGaN
3.85–3.93 eV	AlGaN	Mg or C substitutional

Table 1.2. Summary of some of the most frequently measured defect activation energies with the DLTS and DLOS methods (from [20, 34, 35]).

Finally, most of the levels typical of GaN and AlGaN bulk material can be measured in GaN/AlGaN Schottky HEMTs as well. Still, there are some additional defects which arise only in the fully–processed devices. Among them, the 2.3 eV and the 3.7 eV levels should be located somewhere in the gate stack rather than in the access region [34, 35].

1.2.4 Defects at the interface with a dielectric

The use of a dielectric on top of the AlGaN layer effectively prevents gate leakage currents, in comparison with Schottky devices [11]. The new interface between AlGaN and the insulator, however, in most cases is far from perfect, thus giving rise to interface and near interface defects. It is also not clear what the exact impact on the surface donor states is.

The very first challenge in untangling this problem is to characterize the interface states. In the past decades, many methods have been proposed and some of them are nowadays established techniques for the characterization of silicon MOS devices and MOSFETs. The most widely used methods are based on the response of the device to a superposition of small– and large–signal excitation, with an impedance measurement. The density of interface states can be extracted from the capacitance characteristic of the device (the capacitance–voltage, or CV curve) with the Terman method, or from the device conductance as a function of the small–signal frequency with the conductance method [38]. These standard methods can be used as comparison tools, i.e., to evaluate the relative amount of defects within different samples. Nevertheless, since the portion of accessible defects depends on measurement parameters like frequency of the small–signal and temperature [39], care should be taken in comparing defect densities extracted with different techniques and parameters. For the same reason, it is essen-

tial to optimize the experimental window. For example, if the probing frequency is too high, states with relatively long characteristic time constant would not be able to respond to the applied AC signal. On the other hand, temperature has the effect of decreasing the time constant of the defects, whose response can therefore be accelerated in order to become measurable within the chosen frequency range.

What makes GaN–based devices more challenging to characterize is the wide bandgap of these materials. In fact, part of the defects have very large activation energies, and they cannot be activated with electrical measurements at feasible temperatures. A solution to this problem is to provide energy by optical excitation, i.e., by exposing the devices to light. When the photon energy matches the bandgap of the material, band–to–band generation and recombination is possible. This is the concept behind the UV–assisted CV method [40]. A comparison of the capacitance characteristic of a GaN MIS device before and after illumination with light of 365 nm wavelength (or 3.39 eV, the GaN bandgap) highlights the presence of defects with large activation energies. However, for the same reasons as explained above, discrepancies might be found when comparing results achieved with different methods [41]. The window of accessible defects with the various techniques might be very different, therefore it is problematic to give a conclusive answer about the number of active defects present at the interface with the dielectric.

Most importantly, a further complication arises in the case of composite GaN/AlGaN MIS structures or MIS–HEMTs. In fact, the AlGaN barrier introduces a new frequency response, which can mask or at least superimposes to that of the interface defects. The methods mentioned above rely on a certain model of the MIS stack, which has been developed for simple metal–insulator–semiconductor devices. The presence of a layer with similar bandgap as GaN between the semiconductor and the dielectric instead gives rise to a dynamic response of its own. Assuming the simple model to be valid can be too rough an approximation for the calculation of the interface defect density. Adopting such assumption allows to estimate the density of defects from CV measurements [42, 43], conductance measurements [44] and UV–assisted CV measurements on GaN/AlGaN structures [45]. An example is given in Fig. 1.9a and b. However, device simulations have shown that the mere presence of the AlGaN layer, without any additional interface defect, would be sufficient to explain the observed frequency dispersion, allowing a very good fit to experimental data [46], as shown in Fig. 1.9c. Therefore, neglecting the barrier dynamic response would lead to major inaccuracies in the determination of the defect density. In particular, it has been proven that the barrier effect dominates for short times and low applied positive gate voltage [47]. In this case, the characteristic time constant is only that of the transport of the electrons from the 2DEG towards the interface with the dielectric. For longer times and larger applied positive bias, the characteristic time constant is the combination of the two arising from the transport through the barrier and the subsequent trapping into defects. More details about the role of the barrier are discussed in Section 3.1.

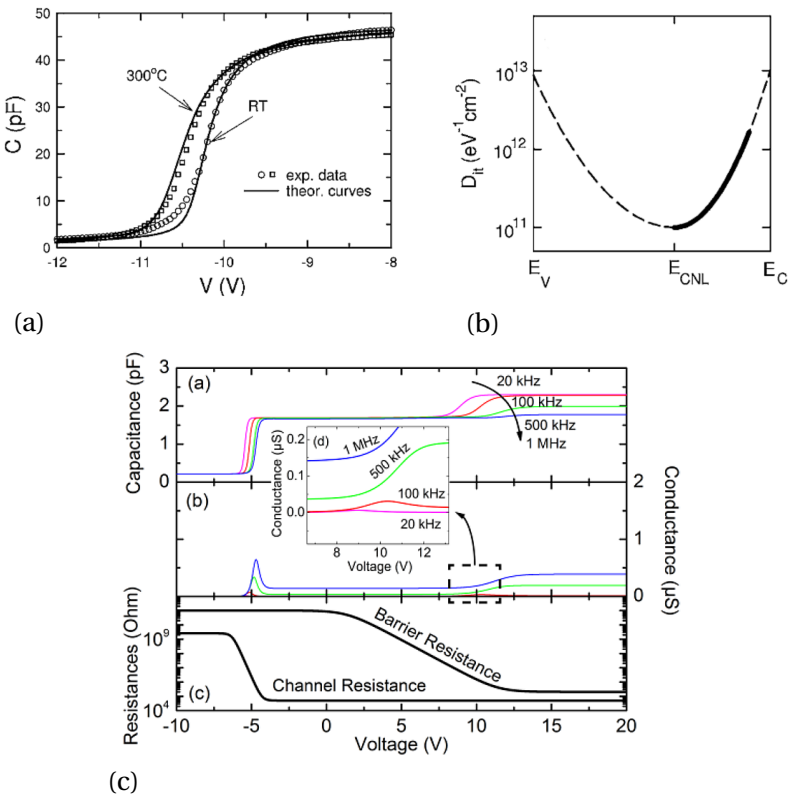

Figure 1.9. (a) A good fit of the CV curves of GaN/AlGaN MIS–HEMTs can be performed assuming a model which includes a major contribution of the interface defects. (b) The density of interface traps can be therefore estimated as D_{it} as a the best fitting curve (from [42]). (c) On the other hand, good agreement with experimental data is found by fitting the impedance characteristics without interface traps, by considering the response of the AlGaN barrier to the small–signal excitation only (from [46]).

In order to investigate the interface defects, methods based on stress and recovery transients can be applied. While a stress at negative gate bias highlights the contribution of defects from the buffer, with a positive gate voltage the 2DEG effectively shields the gate stack from what lies underneath. The effect of a transient at forward gate bias is a shift to more positive gate voltage of the transfer characteristic of the MOSFET, or of the capacitance characteristic of a MIS structure [48]. This reflects a certain amount of charge being trapped from the channel into defects during stress. By assuming the trap states to be located at the interface between the AlGaN barrier and the dielectric, the density of active defects is

$$\Delta N_{it} = \frac{Q_{trapped}}{q} = \frac{C_{diel}}{q}\Delta V \tag{1.1}$$

where $Q_{trapped}$ is the total amount of trapped charge, C_{diel} the dielectric capacitance, q the elementary charge and ΔV the amount of right drift of the device characteristic. This method can also be combined with optical excitation [49, 50] in order to access states with very large activation energies.

Results from stress and recovery experiments indicate a very large amount of accessible states at the interface with the dielectric. Several measurements on GaN/AlGaN MIS–HEMTs with various barrier and dielectric thickness and different insulator materials (SiO_2, Si_3N_4, HfO_2, Al_2O_3) have been compared [51], revealing that the amount of trapped charge responsible for the positive ΔV approaches the theoretical limit of the maximum number of charges available at the interface, which is given by $Q_{\text{trapped}}^{\text{max}} = C_{\text{diel}} V_{\text{gate}}$, the product of dielectric capacitance and applied gate bias, as shown in Fig. 1.10. The larger the dielectric constant, the larger the amount of trapped electrons for the same stress conditions, therefore the density of defects appears to be larger than the density of available electrons in the vicinity of the AlGaN/dielectric interface.

The temporal evolution of the amount of positive drift during stress and recovery allows to understand some of the defect's properties. For example, the characteristic time constant can be extracted from this kind of measurements. By assuming a physical model for charge trapping, we can calculate from the time constants the activation energy, the defect density and other characteristics of the trap levels, which might contribute to their identification. A broad study of the trapping behavior in GaN/AlGaN MIS–HEMTs under forward gate bias stress indicates that all devices show a linear degradation as a function of the logarithm of time, both during stress and recovery [52], as shown in Fig. 1.11. Similarly to what has been concluded for silicon, this behavior cannot be explained by a unique trap site with a specific time constant [53], but by an ensemble of defects with associated time constant distributed from very short (100 ns) to very large (10 ks) values.

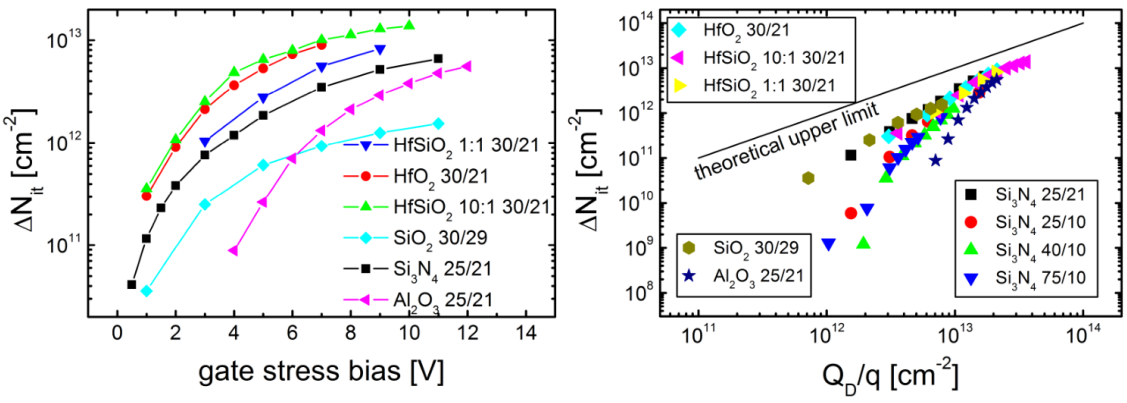

(a) (b)

Figure 1.10. (a) The amount of trapped charge increases with stress bias, V_{gate}, and with the dielectric constant. (b) The amount of charge present at the gate is $Q_D = C_{\text{diel}} V_{\text{gate}}$, and it represents the maximum amount of charge that can be trapped at the AlGaN/dielectric interface. The amount of traps responsible for the ΔV shift get very close to the upper limit in all cases considered in this study (from [51]).

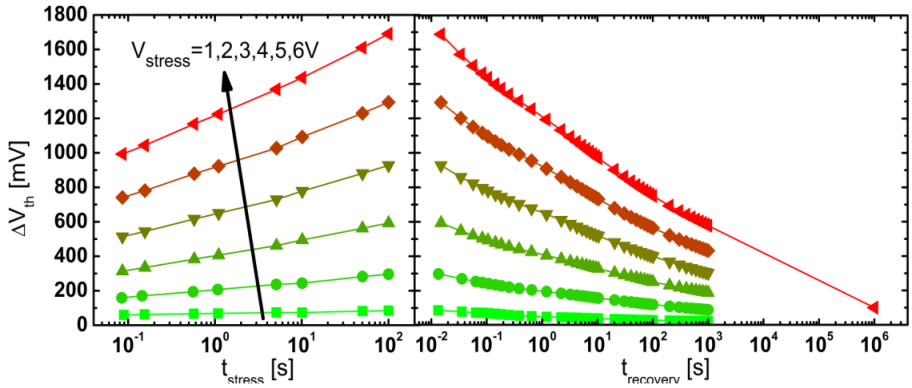

Figure 1.11. Typical behavior of the threshold voltage shift of GaN/AlGaN MIS–HEMTs during (left panel) and after (right panel) forward bias stress (from [52]).

Very recently, a novel surface treatment to the AlGaN layer has been applied before the deposition of the dielectric. This process involving fluorine results in a slightly different 2DEG density at the GaN/AlGaN interface, but also in a fundamentally different trapping behavior at the AlGaN/dielectric interface [54]. In fact, these structures show a relatively high density of defects with a single characteristic time constant of about 100 µs at room temperature. This result indicates that the native surface donor states can be modified with certain chemical processes, and this might be the key to obtain more reliable and stable devices in terms of positive gate bias degradation in future.

A question that still needs a satisfactory answer regards the identity and possible interplay of the surface donor states, responsible for the 2DEG formation, and the states that cause positive ΔV shift under forward bias stress. In particular, the exact properties of the surface donor states can be of fundamental importance. In fact, if we assume that they originate from "deep" defects, i.e., defects with large activation energy and long time constants, they should be usually inactive and apparently stable under normal conditions, but they might still emit one electron causing a negative shift of the device characteristic. As a consequence, the threshold voltage would also change to a more negative value. This is potentially hazardous in terms of the final application, because it might result in an unintentional device turn–on.

Further investigations are therefore required in order to fully understand the dynamics of charge trapping and the origin of the 2DEG, which are the driving questions of the present thesis. The charge trapping dynamics will be addressed with further positive gate bias measurements, focusing in particular on the methodology for a reliable characterization method. The question about the origin of the 2DEG can be investigated in two directions: with stress and recovery experiments at very high temperatures, or with the aid of optical excitation. In this work we develop an optical setup that integrates the existing electrical characterization system, allowing to perform measurements under monochromatic light exposure and thus giving us access to defect states with large activation energy.

1.3 Goal of this thesis

In this thesis we address the problem of defects at the AlGaN/dielectric interface. We illustrate here the contents, giving an overview of its structure and a short summary of each chapter.

The present Chapter 1 introduces the subject, gives the motivation for the work, an overview on the state–of–the–art of the research in this field and summarizes the fundamental facts that will be used in the following chapters.

We present some experimental details in Chapter 2, including a description of the typical sample preparation and the setup used for the measurements. Two more detailed sections regard the introduction of a lock–in amplifier for fast impedance measurements, and the integration of the electrical probe station system with an optical setup for opto–electrical characterization.

In Chapter 3 we discuss the role of the AlGaN barrier in GaN/AlGaN MIS–HEMTs and the challenges that it represents in impedance measurements. We develop an alternative methodology for interface trap characterization based on stress and recovery transients, proposing two techniques which focus on the device response during stress (the on–the–fly technique) and during recovery (the measurement–stress–measurement technique).

Chapter 4 summarizes the theoretical considerations which allow to extract the interesting defect properties from the experimental data. We focus especially on the concept of activation energy, and we perform some simulations to explore the effect of different physical mechanisms on the final, measurable ΔV.

In Chapter 5 we apply the electrical characterization methods presented in Chapter 3 and we analyze the data according to the theory introduced in Chapter 4. A physical interpretation of the trapping mechanisms in standard GaN/AlGaN HEMTs is discussed, in comparison with that of fluorinated devices with modified native surface donor states.

Finally, in Chapter 6 we present the results obtained with the optical setup. We discuss the challenges of this characterization method applied to GaN/AlGaN MIS–HEMTs, we give an overview of the basic theoretical considerations in order to analyze the data, and we perform DLOS measurements to study the trap levels with very large activation energy present in our devices.

2

Experimental aspects

EXPERIMENTAL INSTRUMENTATION AND SAMPLES used in this work are the focus of the present chapter. We describe how the test structures under investigation in our studies are prepared. We highlight the significant variations among them and explain the concept behind our choices. Furthermore, we present the experimental equipment that is used for all measurements reported in this thesis. Special attention is given to the new features that have been added in the course of this work. First, a new software for communication with the instruments has been coded in LabView. Secondly, a lock–in amplifier has been installed for impedance measurements, with the special intention of measuring fast transients. Finally, an optical setup has been integrated to the existing electrical characterization system in order to benefit from the advantages of monochromatic light excitation on our test structures.

2.1 Sample preparation

The test structures in use in this thesis are GaN–based devices grown on silicon. The growth process consists in the deposition of an AlN nucleation layer on the Si(111) surface, followed by several AlGaN layers with different aluminum content. This serves to tune the lattice constant until the residual strain is minimized. In this way a low defect density, unintentionally doped (UID) GaN layer can be realized by metal organic vapor deposition (MOCVD), with a state–of–the–art procedure [55]. The AlGaN barrier is also grown by MOCVD by adding the desired aluminum content, which is 20% or 25% in the test structures used in this work, with a thickness between 20 and 30 nm. The dielectric layer is then deposited on top of the barrier. Different materials can be used, for example silica (SiO_2), silicon nitride (Si_3N_4, abbreviated as SiN), hafnium oxide (HfO_2) or aluminum oxide (Al_2O_3). In our experiments we use devices with silicon nitride insulation only. Finally, the aluminum gate contact is deposited onto the dielectric, and for MIS–HEMTs the source and drain contacts are made by etching the dielectric and AlGaN with a plasma process. The shape of the gate contact is most of the times circular,

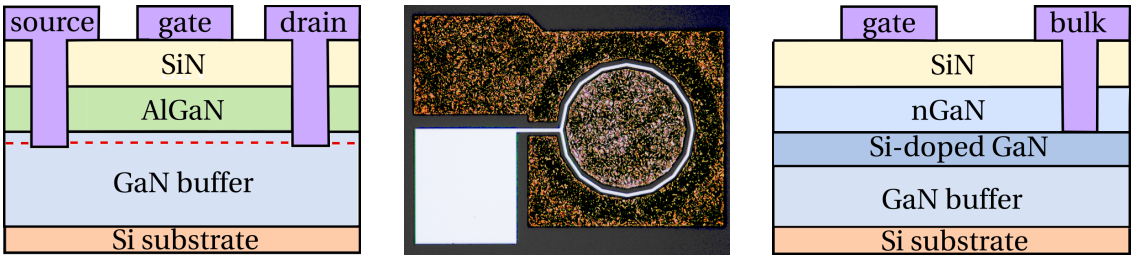

(a) (b) (c)

Figure 2.1. (a) Typical cross–section of a GaN/AlGaN MIS–HEMT, (b) the top view with an optical microscope (gate in white, source and drain are the circular area and the pad above that of the gate) and (c) the GaN–only MIS structure with a silicon doped layer buried in the buffer. In this illustration the layers are not to scale and the nucleation layer on top of the silicon substrate is not shown.

or a comb–like structure for having different perimeter–to–area ratios. Fig. 2.1a and b show a schematic cross–section of a GaN/AlGaN MIS–HEMT, and a top view picture taken with an optical microscope.

Most of the devices used for the characterization of interface defects have a uniform UID GaN buffer. However, in order to investigate the role of the barrier, some wafers without the AlGaN layer have been fabricated. In this way the 2DEG cannot be formed, and the carriers are supplied from a 10^{18} cm^{-3} silicon doped GaN layer buried into the buffer. This particular sample is schematically illustrated in Fig. 2.1c. Other variations in the buffer include doping with carbon (C:GaN) or magnesium (Mg:GaN). These devices have been used for DLOS experiment in the course of the initialization of the optical setup.

Other structures have been developed specifically for opto–electrical characterization. A limiting characteristic of regular GaN–based devices fabricated at Infineon Technologies in Villach is the composition of the gate contact, which consists of about 500 nm of aluminum, which reflects most of the incident light. In fact, this material is used to realize the gratings of monochromators, where the aim is to maximize the reflectance. In order to allow enough light to penetrate through the metal contact and efficiently illuminate the active gate area, gold contacts as thin as 5 nm have been made. To guarantee a better adhesion on the dielectric material, a 3 nm layer of titanium can be inserted below the gold. Both metals can be evaporated on the wafers and structured with a lithography process. We choose these materials because their absorption coefficient is one order of magnitude smaller than that of aluminum [56], as we will discuss in detail in Section 6.3.2. In fact, thin Ti and Au layers are the best choice for this kind of application and are used in many other studies [40, 43, 45, 49].

2.2 Measurement setup

The experimental facilities at the KAI GmbH laboratory include a Süss MicroTec on–wafer probe station for electrical characterization of the devices. The system is mounted on a vibration isolated platform and protected by a shield box. The sample under test is placed on a thermostatic chuck, hold in place by a vacuum pump and it can be contacted with DC probes using a Motic PSM1000 optical microscope (see Fig. 2.2). An ATT P40 temperature control unit allows to heat up or cool down the sample. The user can set the chuck temperature between –60 °C and 200 °C. A dry air flow across the wafer surface ensures that no moisture is retained onto the devices, which would lead to the creation of a frozen water layer at temperatures lower than 0 °C.

Various instruments can perform a range of different measurements: current–voltage (IV), capacitance–voltage (CV), pulse generation and time–domain (transient) measurement. An Agilent B1500A parameter analyzer features ten module slots for source monitor units (SMUs), an impedance bridge Agilent 4294A is dedicated to impedance measurements and an Agilent E5250A switching matrix allows to manage the connections between the instruments and the needles in the probe station through triaxial cables. When coaxial cables must be used, as for impedance measurements, proper adapters are used.

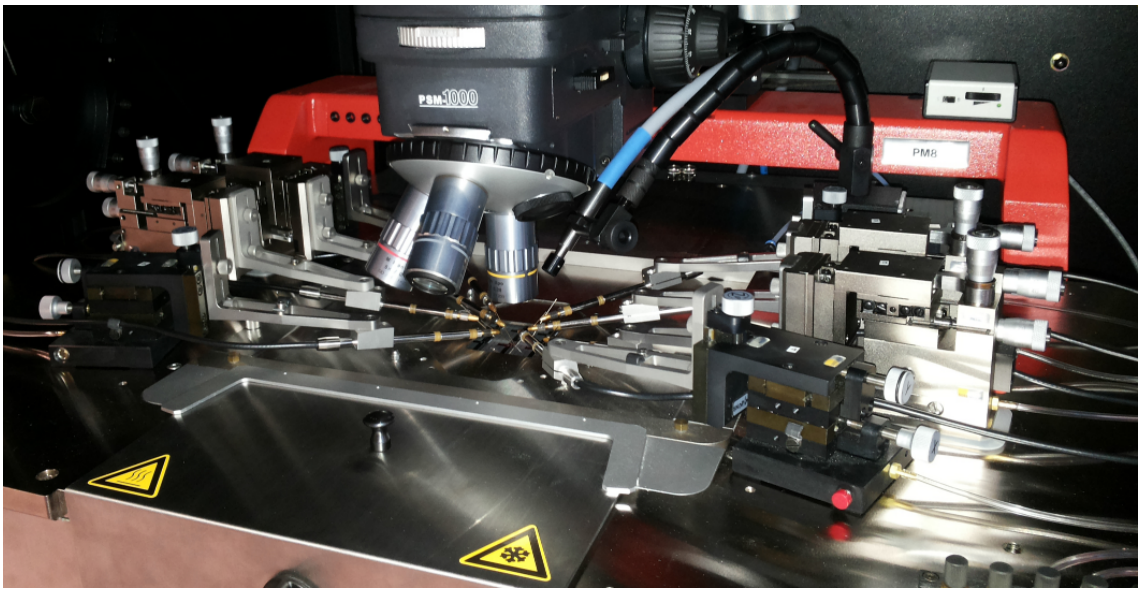

Figure 2.2. Close–up of the interior of the probe station. The electrical contact is made with eight DC probes, which can be moved along the three directions by the manipulators surrounding the window on the wafer under test, and using the optical microscope. The light guide (grey and blue cable) and its mounting is also visible in the background. See Section 2.4 for the description of the optical setup.

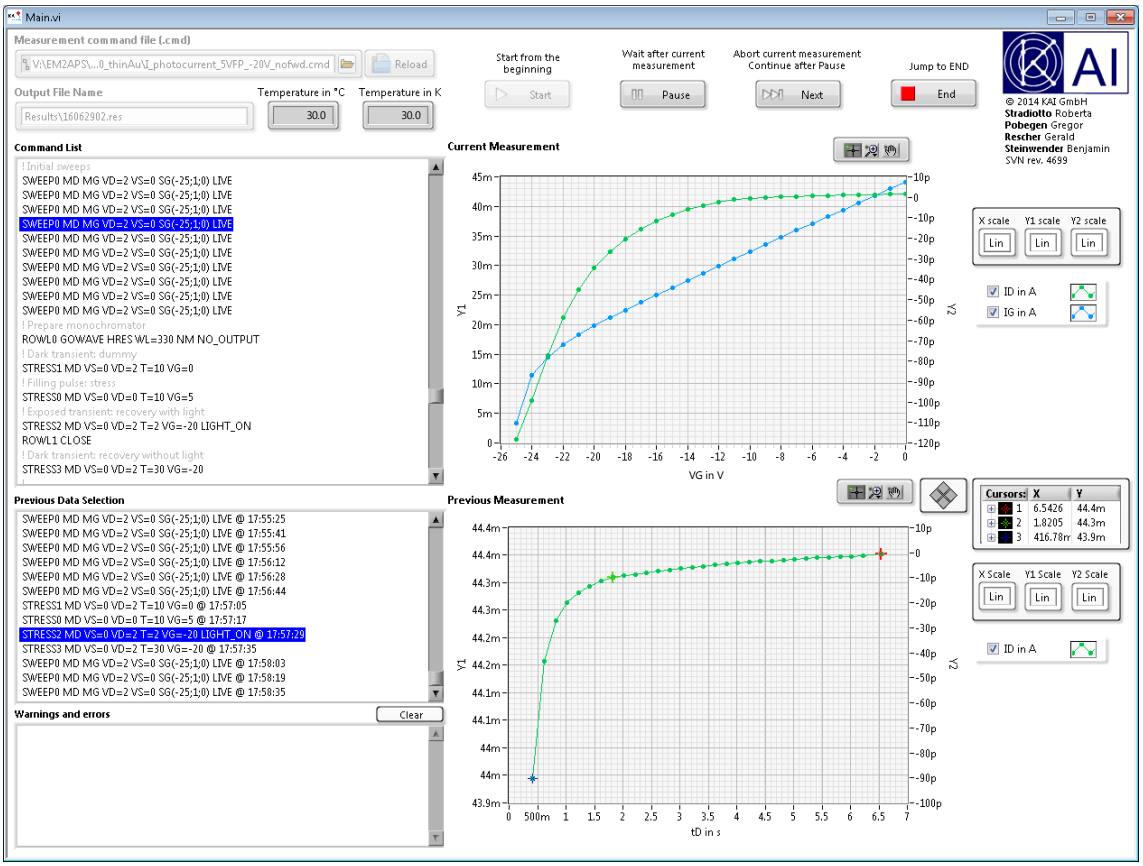

Figure 2.3. A screenshot of the control panel during a measurement with the LabView software developed in the course of this thesis. The input command file is loaded and shown in the upper part together with the current measurement plot. On the bottom part, the chronology of the past measurements is shown and the relative plot can be activated in the window below. A third window shows warning and error messages received from the instruments, or raised during the execution of the program.

During the course of the thesis the software for communicating with the instruments, driving the measurements and storing the data has been developed in LabView. It is based on a producer–consumer architecture, which handles the user interface through the front panel and the other operative tasks in parallel. A screenshot of the main window during the execution of a series of measurements is shown in Fig. 2.3. The communication with the hardware is based on a general purpose interface bus (GPIB), which can send command strings to the instruments and read out measurement data. The core of the program consists in a file parser which loads the measurement instructions contained in a special text file, and writes to another output file the result of the measurement in plain text format. In this way, the user has the possibility to plan a series of consecutive measurements and to control the temperature of the chuck, using a syntax developed *ad hoc*. The output file is ready to be analyzed in a second stage with software programs like Matlab or Python.

2.3 Fast measurement with a lock–in amplifier

A Zurich Instruments HF2LI lock–in amplifier has been integrated to the existing experimental facility. Similarly to the impedance analyzer, this instrument can perform impedance measurements, but it offers a much higher time resolution, thus allowing for very fast transients to be recorded.

Generally speaking, lock–in amplifiers are used to measure signals with a known carrier wave. They find their typical application in extracting a signal from a noisy background, provided that the signal is modulated over a known frequency. This instrument can be extremely reliable even when the signal to noise ratio is very poor. The actual ratio between the amplitude of the maximum tolerable noise and that of the signal is called *dynamic reserve*, and it is expressed in decibel (dB). For the Zurich Instruments HF2LI the dynamic reserve is 100 dB [57], which means that we can measure accurately a signal hundred thousand times smaller than the background noise.

In the following, we describe the working principle of lock–in amplifiers, the phase sensitive detection, and the functionality of our setup in particular. Then we report some details about the calculation of the impedance of the devices under test and, finally, we present our approach to fast sampling measurements .

2.3.1 Functional description

A lock–in amplifier needs a reference signal of a certain frequency, which can be generated by the internal oscillator or provided by an external function generator. In our case, we use the internal oscillator signal as the reference $\tilde{V}_{\mathrm{ref}}(t)$, a sinusoidal wave with amplitude $\sqrt{2}$ V and customizable frequency. The higher the frequency, the larger are the parasitic effects due to the cables and the probes which contact the device. Above a maximum frequency limit the measurements must be considered not reliable anymore. In our case, the limit is 1 MHz, since our setup features standard DC probes only.

The reference signal is used to generate the output signal to be applied to the device under test (DUT), as illustrated in Fig. 2.4a. Its amplitude V_{AC} can be adjusted, and we choose typically 50 mV in order to perform small–signal measurements. In addition, the DC baseline of the output signal can be set by using an auxiliary output, V_{DC}.

The response of the device is led to a current to voltage amplifier, which is described in Fig. 2.4b. The first part of the amplifier consists of a transimpedance stage, which converts the input current I1 to a voltage output. The load R1 can be set to one out of seven available values, which determine the gain in a range from 100 V/A to 100 MV/A. A second amplifying stage offers an output voltage gain G1 of one or ten. In addition, a switch allows to measure the DC signal directly, or to select AC coupling mode, thus removing the DC offset. Finally, an analog to digital converter digitizes the signal into the measured signal, $\tilde{V}_{\mathrm{sig}}(t)$.

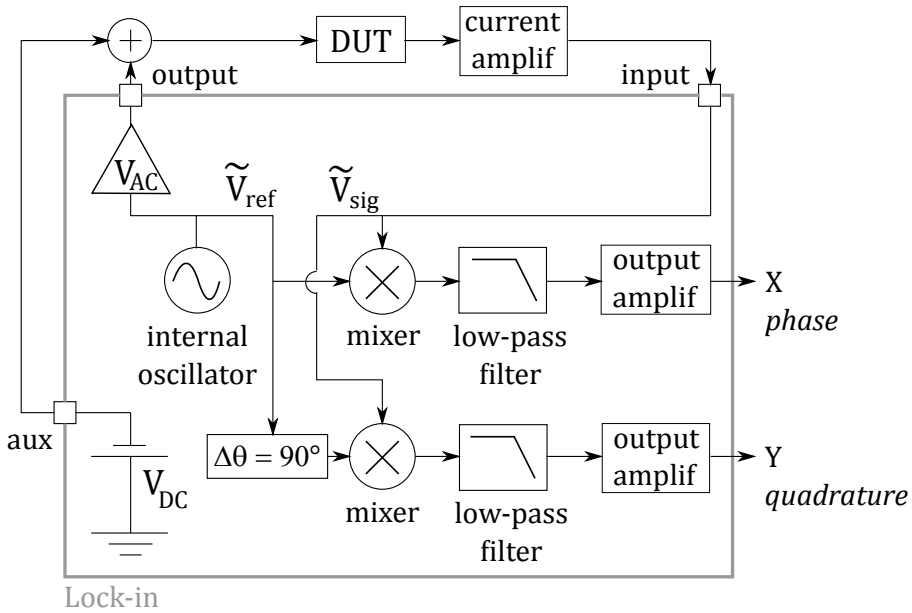

(a)

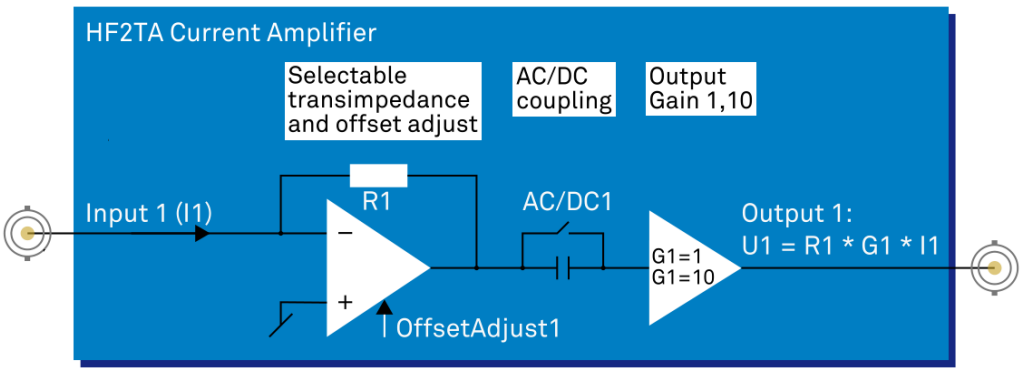

(b)

Figure 2.4. (a) Schematic illustration of the lock–in amplifier setup and (b) of the current amplifier (adapted from [57]).

In general, the measured signal has the same frequency of the reference, but a different phase θ_{sig}. The core of the lock–in amplifier, the *phase sensitive detector*, uses this information in order to extract the signal of interest. Two analog multipliers (or mixers) combine the measured signal $\tilde{V}_{sig}(t)$ with the reference $\tilde{V}_{ref}(t)$, applying a phase shift of $\theta_{ref} = 0$ and $\theta_{ref} = 90°$. Performing this operation, a coefficient $k = 1\,\mathrm{V}^{-1}$ is also introduced. We indicate the amplitudes of the measured and reference signals as $V_{ref} = \sqrt{2}\,\mathrm{V}$ and V_{sig} respectively, and their angular frequencies ($\omega = 2\pi f$) with ω_{ref} and ω_{sig}. In this way, the result obtained by mixing is

$$\begin{aligned} k \times \tilde{V}_{sig} \times \tilde{V}_{ref} &= k \times V_{sig} \sin\left(\omega_{sig} t + \theta_{sig}\right) \times V_{ref} \sin\left(\omega_{ref} t + \theta_{ref}\right) \\ &= k \frac{V_{sig} V_{ref}}{2} \cos\left((\omega_{sig} - \omega_{ref}) t + \theta_{sig} - \theta_{ref}\right) + \\ &\quad - k \frac{V_{sig} V_{ref}}{2} \cos\left((\omega_{sig} + \omega_{ref}) t + \theta_{sig} + \theta_{ref}\right). \end{aligned} \tag{2.1}$$

If the two frequencies are different, this procedure is called *heterodyne demodulation*, the working principle of radio transmissions. However, we expect that the response of the DUT has the same frequency of the excitation ($\omega_{\text{ref}} = \omega_{\text{sig}} = \omega$), therefore we are performing a *homodyne detection*. In this case the result is a DC component proportional to the product of the two signals' amplitudes, plus a component at high frequency 2ω. In fact, the aim of the lock–in amplifier is to shift the spectrum of the demodulated signal to base band, i.e., as close to DC as possible. At this point, the desired $\tilde{V}_{\text{sig}}(t)$ amplitude can be found by applying a digital low–pass filter, which can exclude the 2ω component from the output of the mixers. In other words, we perform a temporal average of the two demodulated signals, which brings us to the final outputs of the lock–in amplifier, X and Y:

$$\begin{aligned} k\,\langle \tilde{V}_{\text{sig}} \times \tilde{V}_{\text{ref}} \rangle &= k\,\frac{V_{\text{sig}}\,V_{\text{ref}}}{2}\cos\theta_{\text{sig}} = \frac{V_{\text{sig}}}{\sqrt{2}}\cos\theta_{\text{sig}} = X \\ k\,\langle \tilde{V}_{\text{sig}} \times \tilde{V}_{\text{ref}} \rangle &= k\,\frac{V_{\text{sig}}\,V_{\text{ref}}}{2}\sin\theta_{\text{sig}} = \frac{V_{\text{sig}}}{\sqrt{2}}\sin\theta_{\text{sig}} = Y. \end{aligned} \tag{2.2}$$

These two components, measured in $\mathrm{V_{rms}}$, describe a vector in the complex plane in cartesian coordinates: X on the real axis, Y on the imaginary axis. They are called *phase* and *quadrature* respectively, as they represent the part of the signal in phase and out of phase with respect to the reference. In polar coordinates, the same vector $X + i\,Y$ is indicated by $R\,e^{i\phi}$: the amplitude is $R = V_{\text{sig}}/\sqrt{2}$ and the phase is $\phi = \theta_{\text{sig}}$. The measured signal R corresponds to the RMS value of the signal amplitude, V_{sig}. Therefore, we can reconstruct the complex signal $\tilde{V}_{\text{sig}}$ as

$$\tilde{V}_{\text{sig}} = V_{\text{sig}}\,e^{i\omega t} = \sqrt{2}R\,e^{i(\omega t+\phi)}. \tag{2.3}$$

2.3.2 Impedance measurement

The complex vector $X + i\,Y = R\,e^{i\phi}$ can be related to the capacitance and conductance of the DUT. Indicating with $\tilde{I}$ the current flowing from the DUT to the amplifier, we can express it in relation to the measured signal $\tilde{V}_{\text{sig}}$ as

$$\tilde{I} = -\frac{1}{R_G}\tilde{V}_{\text{sig}} = -\frac{1}{R_G}\sqrt{2}R\,e^{i(\omega t+\phi)} \tag{2.4}$$

where $R_G = R1 \cdot G1$ is the total gain, and the negative sign comes from the fact that the current amplifier gives a phase shift of 180°. The current $\tilde{I}$ can be also related to the excitation signal applied to the DUT, $\tilde{V}_{\text{exc}} = \mathrm{V_{AC}}\,e^{i\omega t}$ and the measured complex impedance Z_{m} (or the measured complex admittance Y_{m}) as

$$\tilde{I} = \frac{\tilde{V}_{\text{exc}}}{\tilde{Z}_{\text{m}}} = \tilde{\mathrm{Y}}_{\text{m}}\,\tilde{V}_{\text{exc}} = \tilde{\mathrm{Y}}_{\text{m}}\,\mathrm{V_{AC}}\,e^{i\omega t}. \tag{2.5}$$

Thus, we can calculate the measured impedance in a straightforward way as

$$\begin{aligned} \tilde{\mathrm{Z}}_{\text{m}} &= \frac{\tilde{V}_{\text{exc}}}{\tilde{I}} = -R_G\frac{1}{\sqrt{2}R\,e^{i(\omega t+\phi)}}\mathrm{V_{AC}}\,e^{i\omega t} \\ &= -\frac{R_G\,\mathrm{V_{AC}}}{\sqrt{2}R\,e^{i\phi}} = -\frac{R_G\,\mathrm{V_{AC}}}{\sqrt{2}R}\,e^{-i\phi} \end{aligned} \tag{2.6}$$

and the measured admittance as

$$\begin{aligned}\tilde{\mathrm{Y}}_{\mathrm{m}} &= \frac{\tilde{I}}{\tilde{V}_{\mathrm{exc}}} = -\frac{1}{R_G}\sqrt{2}R\,e^{i(\omega t+\phi)}\frac{1}{\mathrm{V_{AC}}\,e^{i\omega t}} \\ &= -\frac{\sqrt{2}R\,e^{i\phi}}{R_G\mathrm{V_{AC}}} = -\frac{\sqrt{2}}{R_G\mathrm{V_{AC}}}(X+iY)\,.\end{aligned} \tag{2.7}$$

At this point, we need to assume an impedance model for the device under test. The complex impedance or admittance are described by a couple of real numbers, which define their real and imaginary parts. We can think of our MIS device (or MIS–HEMT) as a capacitor, in which displacement currents take place as well. The correct way to describe its behavior is the parallel model: a capacitance $\mathrm{C_m}$ and a conductance $\mathrm{G_m}$ in parallel. The complex admittance in this case is given simply by $\tilde{\mathrm{Y}}_{\mathrm{m}} = \mathrm{G_m} + i\,\omega\,\mathrm{C_m}$. Therefore, we find the solution in terms of the lock–in measured quantities X and Y as

$$\mathrm{G_m} = \Re\mathrm{e}\{\tilde{\mathrm{Y}}_{\mathrm{m}}\} = -\frac{\sqrt{2}X}{R_G\,V_{\mathrm{AC}}} \qquad \text{and} \qquad \mathrm{C_m} = \frac{\Im\mathrm{m}\{\tilde{\mathrm{Y}}_{\mathrm{m}}\}}{\omega} = -\frac{\sqrt{2}Y}{\omega\,R_G\,V_{\mathrm{AC}}}. \tag{2.8}$$

Finally, we can improve our result by correcting the test fixture residuals. In fact, the actual $\mathrm{C_m}$ and $\mathrm{G_m}$ measurement includes not only the DUT, but also the probes and the cables necessary for the connection. This introduces a parasitic effect, which can be simplified and modelled as an additional *residual impedance* $\tilde{\mathrm{Z}}_{\mathrm{s}} = \mathrm{R_s} + i\,\omega\,\mathrm{L_s}$ and a *stray admittance* $\tilde{\mathrm{Y}}_0 = \mathrm{G_0} + i\,\omega\,\mathrm{C_0}$, as shown in Fig. 2.5a. Performing a measurement with open terminals (Fig. 2.5b) and one by contacting the two probes directly together (Fig. 2.5c), we have an estimate of the parasitic components $\mathrm{R_s}$, $\mathrm{L_s}$, $\mathrm{G_0}$ and $\mathrm{C_0}$. In this way, we can correct our $\mathrm{C_m}$ and $\mathrm{G_m}$ to the real DUT capacitance and conductance $\mathrm{C_{DUT}}$ and $\mathrm{G_{DUT}}$ by solving the following equation for $\tilde{\mathrm{Y}}_{\mathrm{DUT}} = \mathrm{G_{DUT}} + i\,\omega\,\mathrm{C_{DUT}}$:

$$\tilde{\mathrm{Z}}_{\mathrm{m}} = \tilde{\mathrm{Z}}_{\mathrm{s}} + \frac{1}{\tilde{\mathrm{Y}}_{\mathrm{DUT}} + \tilde{\mathrm{Y}}_0}. \tag{2.9}$$

An example of the result achieved by such a correction is shown in Fig. 2.6 for a CV characteristic of a GaN/AlGaN MIS device. A measurement with the impedance analyzer is also included.

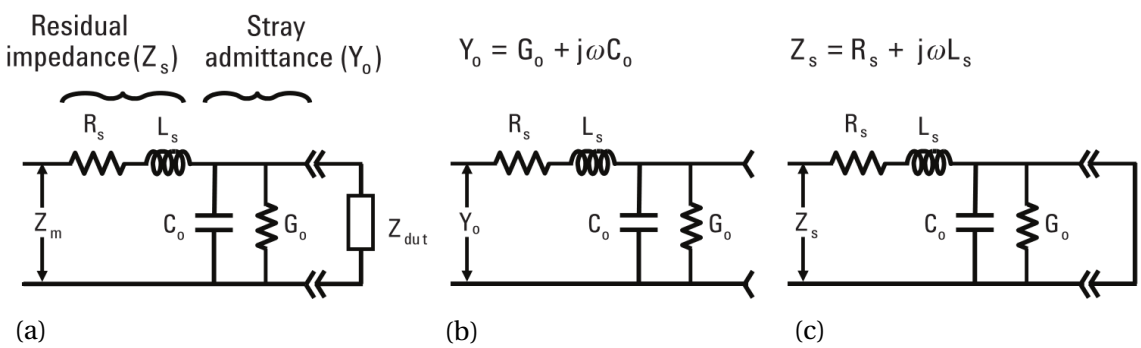

Figure 2.5. (a) Model of the test fixture residuals, showing the residual impedance in series and the stray admittance in parallel with the DUT impedance. (b) The measurement with open and (c) shorted contacts for the parasitic correction (adapted from [58]).

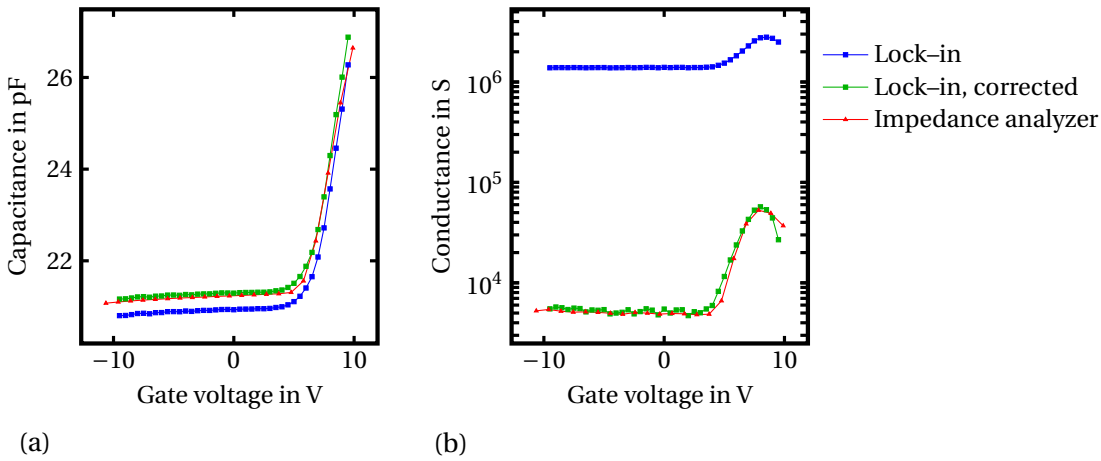

Figure 2.6. The capacitance (a) and conductance characteristics (b) are taken with the impedance analyzer and the lock–in amplifier. After the correction of the test fixture residuals, the two measurements show a good agreement.

We clearly see that the parasitics correction leads us to a more accurate measurements, since the result from the lock–in amplifier after correction agrees with that of the impedance analyzer. The difference in shape of the CV curve is due to the different timing of the measurement, and it will discussed in detail in Chapter 3.

2.3.3 Sampling measurement

The main reason to use the lock–in amplifier for impedance measurements is that it offers a very high time resolution. In fact, the sampling rate of this instrument can be as high as 210 MSa/s, and it can be adjusted during operation to fit the user's needs. The lower limit is given by the Nyquist principle, which states that the sampling frequency must be at least twice the maximum signal frequency to avoid aliasing. We usually choose a fixed signal frequency f and we tune the sampling rate making sure that it never falls below $2f$.

We set the sampling frequency to a value large enough to achieve the desired time resolution, but not exceeding it further in order to keep an acceptable number of samples. To maximize the resolution at the beginning of the transient, the measurement starts with maximum sampling rate, at the instant when the trigger to the auxiliary output is sent. Then the driving software, included in the main LabView interface, automatically selects the sampling rate to record a constant number of samples per decade. In this way, an approximately logarithmic spacing in time between samples is achieved.

The smallest time at which the lock–in provides an accurate measurement depends on the time constant (TC) of the digital filter. A small TC results in fast sampling, at the expenses of the signal to noise ratio. Therefore, a trade–off must be found in order to perform accurate and fast sampling at the same time. In fact, a certain amount of time is needed for the lock–in to reach

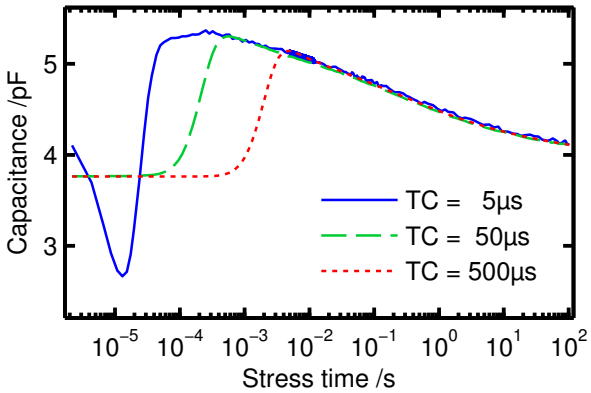

Figure 2.7. The measured transient is the convolution of the filter response with the actual signal from the DUT. A fourth order filter needs about ten times the TC in order to achieve the correct value with 99% accuracy.

the correct final value, which itself depends on the chosen TC. This is due to the roll–off of the digital filter, which is a characteristic depending on the filter order. Before the settling time of the filter, the lock–in response is a convolution of the signal with the filter time response. For example, the fourth order filter in use in our case has a roll–off of 24 dB/octave. In this case, an accuracy of 99% is achieved after ten times the chosen time constant [57]. Therefore, with a TC of 5 µs the time resolution is of approximately 50 µs, for a TC of 50 µs the first accurate point is at 500 µs and so on, as one can see in Fig. 2.7.

Taking into account the points discussed in this section, the lock–in amplifier enables us to measure accurate impedance transients with a time resolution of 50 µs, thus allowing five orders of magnitude more than with the standard impedance analyzer, as shown in Fig. 2.8. This enables us to develop a methodology for characterization of interface defects, which will be the object of Chapter 3.

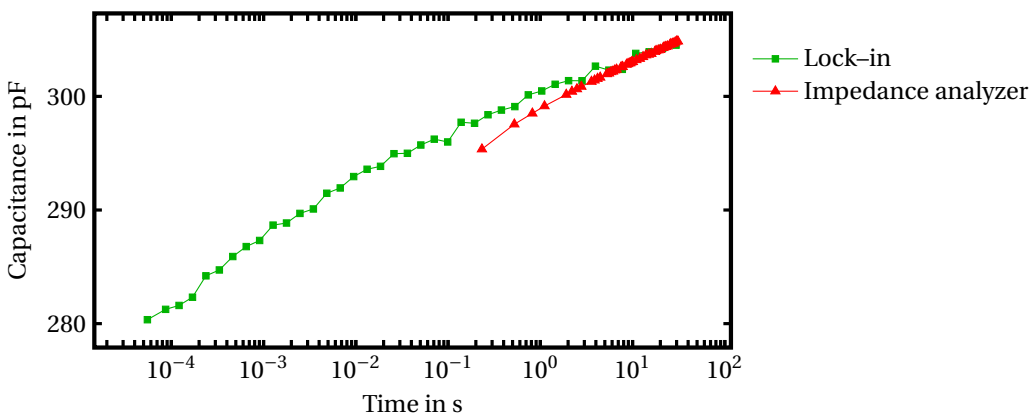

Figure 2.8. A capacitance transient measured with the impedance analyzer and with the lock–in amplifier, which has an advantage of five orders of magnitude while providing accurate data.

2.4 Setup for opto–electrical characterization

In order to extend the possibilities of the existing electrical characterization setup, a system for optical excitation has been developed. Most of the DLOS experimental setups consist of an open–beam optical bench, shielded by a black enclosure, where a single chip or device can be placed onto a dedicated holder to be characterized. In our case instead, we integrate the optical system to the on–wafer prober. The optical bench is placed outside the probe station and the light is brought to the device under test with a light guide. All the optical components are therefore enclosed individually, to protect the operators from the potentially hazardous radiation when working with wavelengths in the ultraviolet range.

In this section, we describe the components of the optical setup: the light source, the monochromating system and the light guide for the transmission of the optical energy. Furthermore, we evaluate its performance in terms of output light intensity.

2.4.1 Light source

The source of light is a high–pressure, short–arc discharge xenon lamp. It has a power of 300 W and emits light in a broad spectrum, almost featureless in the ultraviolet (UV, from 200 nm to 400 nm, or from 3.1 eV to about 6 eV) and visible (VIS, from 400 nm to 700 nm, or from 1.7 eV to 3.1 eV) range, with characteristic Xe lines between 750 nm and 1 µm, as shown in Fig. 2.9.

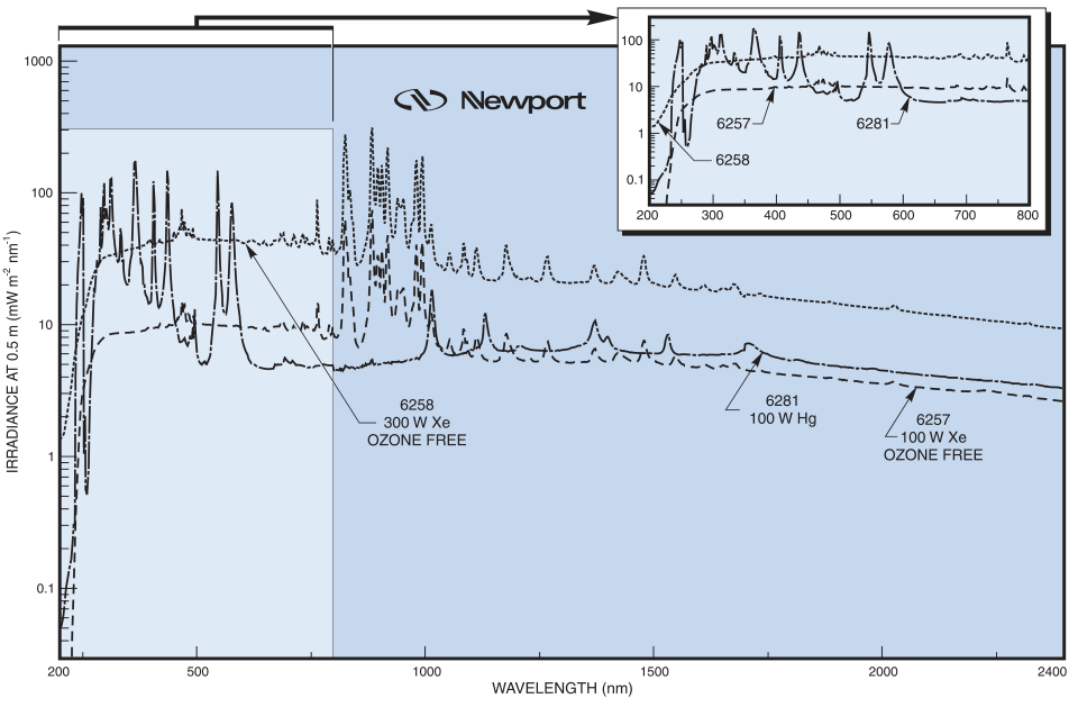

Figure 2.9. The spectra of some Xe and Hg discharge lamps. The one used in our setup is the 300 W Xe "ozone free", labeled with the number 6258 (from [59]).

A special coating prevents radiation below 200 nm, which can cause ionization of the oxygen present in the air, producing ozone. This is a safety measure, because breathing ozone can be harmful to health, as it damages the lungs.

The lamp housing (an Oriel Instruments research arc lamp source) consists of a metallic enclosure where the lamp can be mounted on a special socket. The ignitor for the lamp start up is built–in, and a fan with a temperature sensor ensures a proper cooling down of the lamp during operation. A collimating lens system gathers the emitted light and provides an output beam with a diameter of 33 mm. A rear reflector is placed behind the lamp and conveys the light emitted towards the back of the housing into the collimating optics. In this way, the output power is enhanced by 60%. Finally, standard flange mountings allow to match the lamp housing with the next component, leaving the light beam fully enclosed.

2.4.2 Monochromator

The beam next enters a Cornerstone 260 motorized monochromator, whose function is to transmit selectively the light around the desired wavelength λ, or energy

$$E = \frac{hc}{\lambda} \approx \frac{1240}{\lambda} \tag{2.10}$$

if the wavelength is measured in nm and the energy in eV. The basic principle of operation is shown in Fig. 2.10. The input slit lets the light in onto the grating, which diffracts the beam by reflecting the components at various wavelength with a different angle. The grating can rotate around its axis, thus selecting the central wavelength that is conveyed by the focusing mirror into the exit slit. A mechanical shutter can be used in order block the light path. The slits can be manually adjusted by micrometer–driven screws from a minimum width of 4 µm to a maximum of 3 mm, and from 3 mm to 12 mm in height. The width of the exit slit determines

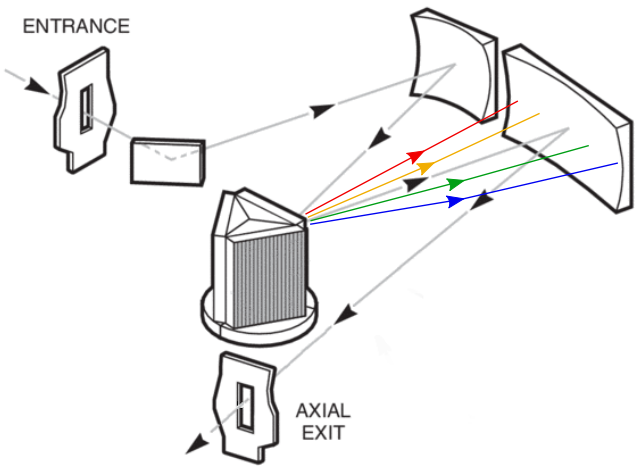

Figure 2.10. The working principle of the monochromator (from [60]).

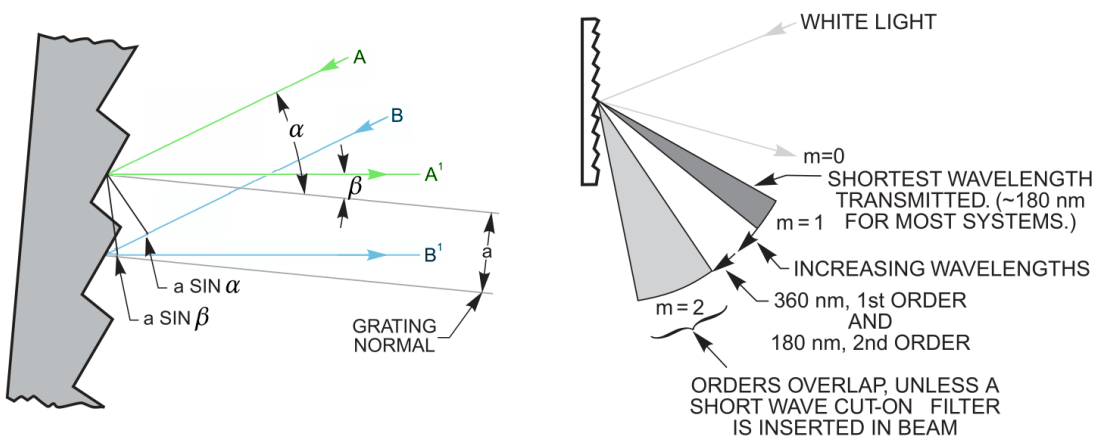

(a) (b)

Figure 2.11. (a) Illustration of the light diffraction by the grating's surface, from which the grating equation is derived. (b) Diffraction of polychromatic light from the grating: different orders of different wavelengths can overlap (adapted from [60]).

the *bandpass*, i.e., the range in wavelength of the output light: the thinner the slit width, the narrower the bandpass. The slit height instead has an impact on the output light intensity.

The gratings consist of an aluminum surface with regular, parallel grooves. The grating equation can be derived considering Fig. 2.11a: we have constructive interference between the reflected rays A^1 and B^1 if

$$a\left(\sin\alpha + \sin\beta\right) = m\lambda \tag{2.11}$$

where m is an integer and represents the *order of diffraction*. The most intense reflection corresponds to the first order m = 1. This basic equation holds true not only for two parallel grooves but for the whole grating. As a consequence, each wavelength is reflected with a certain angle θ for m = 1, and at multiples of θ at higher orders. If a white light beam is the input of the monochromator, it is clear that in certain situations we might obtain the main first order contribution from the wavelength λ, but also an additional contribution from the second order of the wavelength $\lambda/2$ at the same angle. This problem is illustrated in Fig. 2.11b, and it is solved by using a cut–on filter when the desired output is at a multiple of the minimum wavelength. In our case the minimum achievable wavelength is around 200 nm, therefore a cut–on filter with cut–off wavelength of 400 nm is used when the output is set above 400 nm in order to suppress second order reflections of light at 200 nm, and similarly a cut–on filter at 800 nm is used to eliminate the third order contributions.

The Cornerstone 260 monochromator allows to mount two gratings on a rotating stage, so that the user can select the desired one. The characteristics of the gratings are summarized in Table 2.1. The lines per millimeter indicate the density of grooves on the grating surface: the larger this value, the higher the output intensity and the narrower the wavelength range that can be achieved. The efficiency of the grating is not constant throughout its wavelength

		LR grating	HR grating
Lines per millimeter	in mm^{-1}	150	1200
Blaze wavelength	in nm	300	350
First order range	in nm	190 to 800	200 to 1400
Peak efficiency		70%	80%
Reciprocal dispersion	in nm/mm	25.5	6.7

Table 2.1. Characteristics of the two gratings in use with the Cornerstone 260 monochromator.

output range: the one that maximizes the efficiency is called the *blaze wavelength*. Finally, the reciprocal dispersion determines the final bandpass as a function of the exit slit width.

We use the first grating to maximize the bandpass (LR or low resolution grating), because in this way we maximize also the light intensity. In this case, for the maximum slit width of 3 mm the bandpass is 25.5 nm/mm × 3 mm = 160 nm. The second grating (HR or high resolution grating) is dedicated to spectroscopies, therefore the aim is to achieve the best resolution in wavelength. If we keep the slit width at its maximum to improve the light intensity, the bandpass is 6.7 nm/mm × 3 mm = 20 nm, and it can be decreased further by making the slit narrower. Although the theoretical maximum resolution is 0.02 nm, the real value is limited to 0.1 nm because of non–ideal behavior of the optics, for example due to aberrations.

Except for the micrometer driven slits, all other functionalities of the monochromator can be accessed remotely via GPIB. Dedicated drivers and a control software have been written in LabView. Available commands allow to choose the grating in use, set the central wavelength and manage the shutter opening and closing time. It is also possible to perform the same operations within the main measuring program described in Section 2.2, using a dedicated syntax in the input command file.

2.4.3 Light transmission

The light beam at the monochromator's output is ready to be brought to the device under test inside the on–wafer prober. We use a 2 m–long Newport liquid light guide for efficient transmission of light. It consists of a plastic tube, covered by a PVC jacket. The inner part is filled with a transparent, anaerobic, non–toxic fluid which transports optical energy by total reflection. The active core is 5 mm in diameter, sealed at both ends with fused silica glass windows. The whole volume is uniformly filled with light during operation, in contrast with fiber optics which are formed by many single, smaller tubes, thus creating a pattern of active and dead spots. The transmittance range of the light guide is dedicated to wavelengths in the UV and VIS range, as shown in Fig. 2.12. The efficiency is very good, exceeding 80% around 500 nm.

Since the working principle is total reflection, the light guide has a defined *acceptance angle*. This means that light rays with larger angle than the critical θ are not transmitted but absorbed,

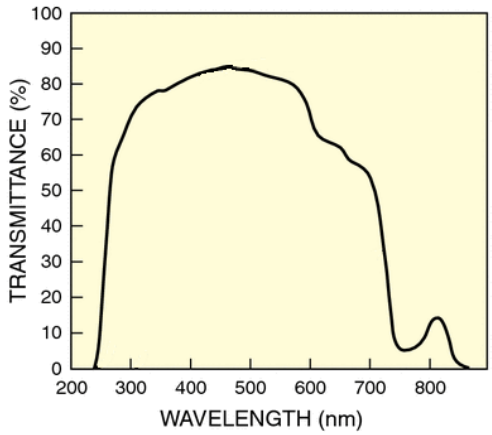

Figure 2.12. Transmission efficiency of the liquid light guide used in our setup.

thus heating up the light guide and eventually wearing out the light conductive material. The sine of such angle is called *numerical aperture* (NA) and it is a characteristic of the light guide, determined by its geometry and the refraction index of the building materials [61]. The NA can be calculated for any optical component, in the way illustrated in Fig. 2.13a. In the case of a lens, the important parameters are its diameter D and its focal length f. The NA is calculated with the approximation for small angles, resulting in $D/2f$. This number quantifies the light gathering ability of the lens, or fiber: the larger the NA, the larger the acceptance angle.

For example, in order to couple the light guide to the monochromator's exit slit, we must use a focusing assembly that matches the NAs of the two parts. The monochromator and the light guide have NAs of 0.13 and 0.43, i.e., the monochromator's output divergence angle is $2\theta = 15$ degrees, and the light guide has an acceptance angle of $2\theta = 98$ degrees. We can efficiently focus the light beam using a bi–convex lens of diameter $D = 25.4$ mm and focal length $f = 32$ mm, as shown in Fig. 2.13b. This works because the lens' NA is 0.385, thus resulting in

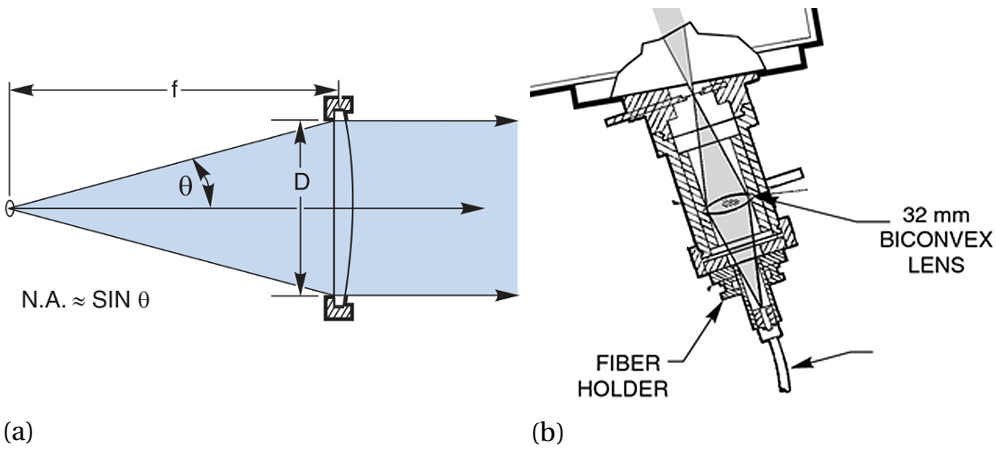

Figure 2.13. (a) Illustration of the numerical aperture (NA) definition. (b) Coupling the light guide to the monochromator requires a proper choice of focusing optics (adapted from [60]).

an angle of 90 degrees. In this way, the light from the monochromator can be fully gathered by the lens, and then focused into a volume which is contained by the acceptance cone of the light guide, so that the incidence angle always results in total internal reflection.

The light guide is flexible and it can be introduced inside the probe station. It can be attached to an adjustable mounting, anchored to the bench with a magnetic base, which can be positioned and fixed above the device under test in order to perform experiments including optical excitation.

2.4.4 Light intensity

The intensity of the light provided by the light guide is not constant at all wavelengths. It is important to evaluate the relative intensity of light over the accessible energy range in order to correctly interpret the response of the device under test when it is exposed to optical excitation at various wavelengths.

In the first place, the lamp radiates according to the emission spectrum, shown in Fig. 2.9. Furthermore, every optical component transmits different wavelengths with variable efficiency. The optical power at a certain wavelength is the product of the lamp emission spectrum with the transmission or reflection spectra of all components in the optical path: condenser lens, grating, cut–on filter, focusing lens and the light guide. Finally, the power of incident light onto the device is found by integrating the power at a single wavelength over the range of interest, which is determined by the bandpass of the monochromator.

While it is difficult to give an accurate estimate of the optical power based on calculations, it is possible to measure it with a calibrated photodiode. Photodiodes are sensors that produce a current directly proportional to the intensity and wavelength of the light incident on their active area. They are characterized by a specific spectral response, called *responsivity*, defined as the amount of current produced per unit power of incident light as a function of the wavelength. We use a Thorlabs SM1PD2A photodiode, whose responsivity is shown in Fig. 2.14.

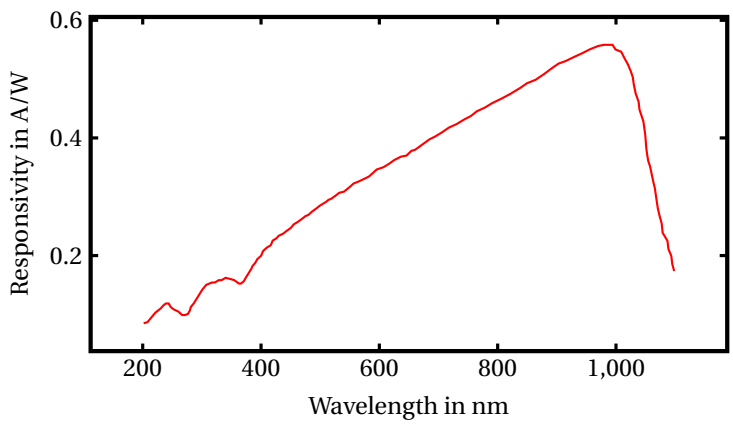

Figure 2.14. Spectral response of the calibrated photodiode (data from [62]).

In this way, we can evaluate the power of our optical setup as a function of the wavelength (or energy) performing a measurement with the photodiode. Recording the current generated by the light, the photocurrent I_{photo}, and knowing the photodiode's responsivity R, we can calculate the power P_{light} at a single wavelength as

$$P_{light} = \frac{I_{photo}}{R}. \tag{2.12}$$

If the sensor's active area is illuminated by the whole light beam without losses, we can calculate the number of photons arriving on the surface, or the *photon flux* Φ_{ph} as

$$\Phi_{ph} = \frac{P_{light}}{q\,\text{area}\,h\nu} \tag{2.13}$$

where q is the elementary charge, the area is that of the photodiode's active surface, and $h\nu = hc/\lambda$ is the photon energy. The result is shown in Fig. 2.15: our optical setup is capable of generating about 1.5 mW of optical power on average, providing up to 2×10^{15} photons per unit area and per unit time.

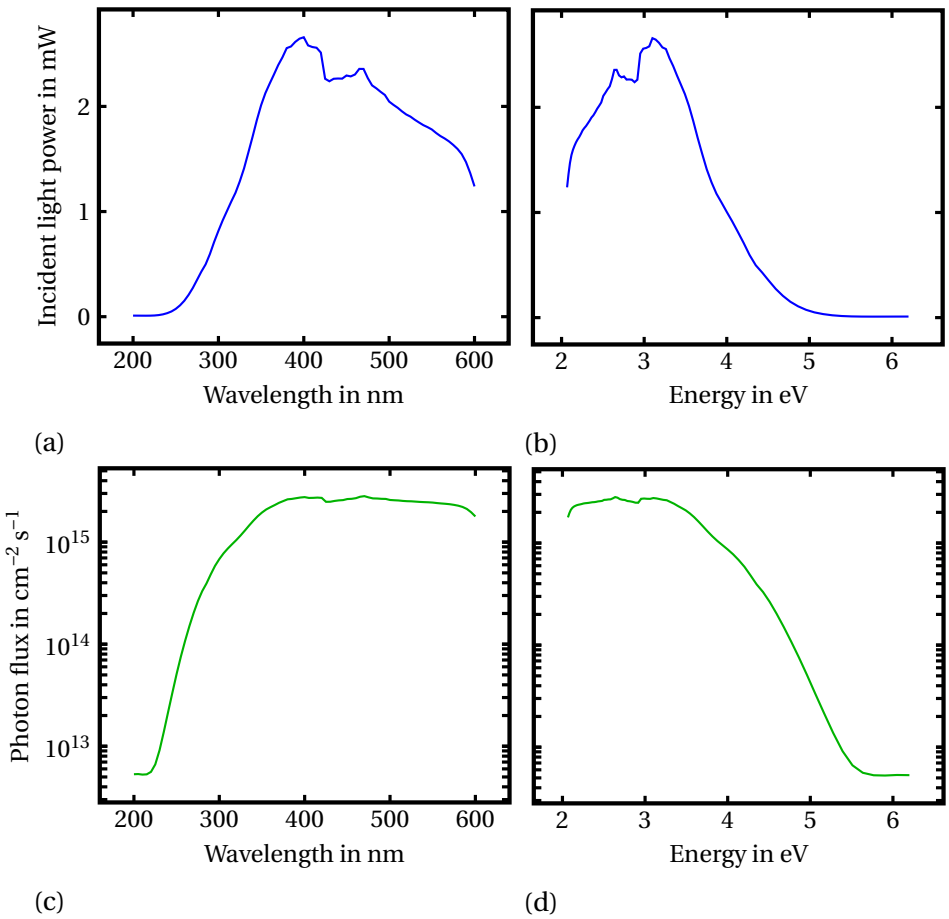

Figure 2.15. Incident optical power (a and b) and photon flux measurement (c and d) with the calibrated photodiode as a function of the photon wavelength and energy.

These results will be used to normalize the device's electrical response during exposure to different wavelengths. Nevertheless, since the area of the device is much smaller than that of the illuminated region by the light beam, the effective power (and number of photons) incident on the structure under test will be smaller than what has been calculated here, but still being proportional to that. For this reason, any quantity evaluated as a function of the light energy will include a proportionality factor, as we will see in Chapter 6.

3

Methodologies for electrical characterization of interface defects in GaN–based MIS–HEMTs

SMALL SIGNAL investigations allow us to study in detail the behavior of the devices under test, as well as their frequency response. A number of methods based on impedance measurements have been established in the past decades in order to evaluate the density of defects at the interface with the dielectric. We focus on the two most used ones, explain their principle of operation and the approximations used, and we underline their limitations when applied to GaN–based devices. The main factor that makes such methods inaccurate in our case is the presence of the AlGaN layer. We investigate the role of the barrier and show that composite GaN/AlGaN structures require a more complex equivalent circuit model than that of regular MIS devices. Furthermore, we highlight other issues that constitute a challenge for an accurate characterization of MIS structures and MIS–HEMTs, namely hysteresis and the CV curve dependence on the measurement parameters. Finally, we develop two methods to evaluate the defect density based on the threshold voltage shift, applying a combination of small and large signal excitation.

3.1 The main established methods and their limitations

In this section we focus on the most used methods based on impedance measurements for the extraction of the interface defect density. In the first place, we need to develop a model for the small–signal response of a MIS structure. We present an equivalent circuit model, highlighting the assumptions and approximations used in the derivation. Then we describe the Terman and the conductance methods in detail, showing how they are applied to the experimental data and their limitations.

3.1.1 The equivalent circuit model

The model for the interface defects should describe the phenomenological loss of energy due to the trapping of conduction electrons into trap states. In the first place, the defects are effectively centres of charge storage: for this reason, we can associate to them a certain capacitance C_{it}. Furthermore, charge trapping do not follow precisely the AC signal, but it lags behind. The small–signal is a perturbation and the system evolves in time in order to return to equilibrium. This can be modelled with a certain characteristic time constant τ_{it}. The equivalent circuit model therefore consists of the interface state capacitance in series with a certain resistance R_{it} (series RC circuit), which gives rise to the time constant τ_{it} given by the product $R_{\mathrm{it}}C_{\mathrm{it}}$, as shown in Fig. 3.1a.

The equivalent circuit can be derived in a more rigorous way [63]: we summarize here the most important concepts and we highlight the approximations used. The net current density flowing in the device can be written as

$$i(\mathrm{t}) = q\left[r_n^c(\mathrm{t}) - r_n^e(\mathrm{t})\right] \tag{3.1}$$

where r_n^c and r_n^e are the capture and emission rate constants for electrons, respectively. The first assumption is the Shockley–Read–Hall (SRH) model for the rate constants. Originally, this theory has been developed for deep trap states inside a semiconductor, but its validity is here assumed to extended to interface states as well. The rate constants depend on the density of electrons available at the semiconductor surface, n_{s}, the density of traps N_{it}, the Fermi function f and the probability for electron capture c_n and emission e_n as

$$r_n^c(\mathrm{t}) = n_{\mathrm{s}} N_{\mathrm{it}} c_n \left[1 - f(\mathrm{t})\right] \qquad \text{and} \qquad r_n^e(\mathrm{t}) = N_{\mathrm{it}} e_n f(\mathrm{t}). \tag{3.2}$$

In the SRH model it is assumed that the capture and emission probability depend on the energy difference between the trap state and, in the case of electrons, the conduction band edge (this topic is discussed further in Chapter 4). In this case, we consider the interface states to be located at the same energetic position inside the bandgap. We also assume the small–signal approximation to be valid, i.e., to a small variation δv of the gate voltage around the mean value v_0 corresponds a small variation of the Fermi function f and of the surface potential ϕ_{s}, according to

$$v = v_0 + \delta v, \qquad f = f_0 + \delta f \qquad \text{and} \qquad \phi_{\mathrm{s}} = \phi_{\mathrm{s},0} + \delta\phi_{\mathrm{s}}. \tag{3.3}$$

Finally, we assume that thermal equilibrium is reached, therefore the detailed balance equation is valid and we can write the electron emission probability as a function of the capture probability:

$$e_n = n_{\mathrm{s}} c_n \frac{1 - f_0}{f_0}. \tag{3.4}$$

Manipulating Eq. (3.1) with these conditions, we can write a direct relationship between the net current density and the variation of the surface potential, from which an equation for the

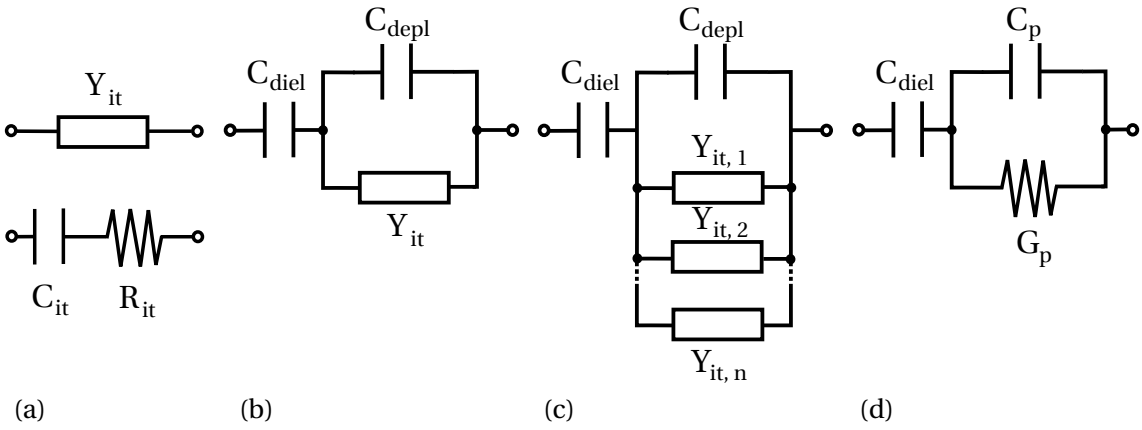

Figure 3.1. Equivalent circuit model for the admittance of the interface defects (a) and of the full MIS structure (b) in the single–level approximation; generalization to an ensemble of trap states with different energy levels (c) and the model of the measured device impedance (d).

admittance of the interface, Y_{it}, can be derived:

$$i(\mathrm{t}) = Y_{\mathrm{it}}\,\delta\phi_{\mathrm{s}} \qquad \text{with} \qquad Y_{\mathrm{it}} = \frac{1}{R_{\mathrm{it}}} + i\omega\, C_{\mathrm{it}}. \tag{3.5}$$

The admittance Y_{it} can be modelled with a resistance R_{it} and a capacitance C_{it} in series, as shown in Fig. 3.1a. The response of the interface states is therefore characterized by the time constant $\tau_{\mathrm{it}} = R_{\mathrm{it}} C_{\mathrm{it}}$.

In order to investigate the defects at the interface with the dielectric, we need an equivalent circuit model for the full MIS structure. In the first place, we consider the distribution of charge in the device: the charge present at the gate contact Q_{gate} must be counterbalanced by the charge of the depletion region of the semiconductor Q_{depl}, the charge trapped at the interface Q_{it} and any possible fixed charge Q_{fixed}, according to

$$-Q_{\mathrm{gate}} = Q = Q_{\mathrm{depl}} + Q_{\mathrm{it}} + Q_{\mathrm{fixed}}. \tag{3.6}$$

When the small signal is applied, only the quantities depending on the surface potential follow the bias oscillation. For this reason, the small–signal current density arises from the contribution of the depletion region, $i_{\mathrm{depl}}(\mathrm{t})$, and that of the interface, $i_{\mathrm{it}}(\mathrm{t})$. The former can be written as

$$i_{\mathrm{depl}}(\mathrm{t}) = \frac{\mathrm{d}Q_{\mathrm{depl}}(\mathrm{t})}{\mathrm{dt}} = \frac{\mathrm{d}Q_{\mathrm{depl}}(\mathrm{t})}{\mathrm{d}\phi_{\mathrm{s}}}\,\frac{\mathrm{d}\phi_{\mathrm{s}}(\mathrm{t})}{\mathrm{dt}} = C_{\mathrm{diel}}\,\frac{\mathrm{d}\phi_{\mathrm{s}}(\mathrm{t})}{\mathrm{dt}} = i\omega\, C_{\mathrm{diel}}\,\delta\phi_{\mathrm{s}} \tag{3.7}$$

and we have just derived an expression for the latter, $i_{\mathrm{it}}(\mathrm{t}) = Y_{\mathrm{it}}\,\delta\phi_{\mathrm{s}}$. Together, the small–signal current due to the variation of the surface potential is

$$i(\mathrm{t}) = i_{\mathrm{depl}}(\mathrm{t}) + i_{\mathrm{it}}(\mathrm{t}) = [Y_{\mathrm{it}} + i\omega\, C_{\mathrm{diel}}]\,\delta\phi_{\mathrm{s}}, \tag{3.8}$$

which corresponds to an equivalent circuit model of the depletion capacitance in parallel with the admittance of the interface states. As a second step, we consider the potential drop across

the MIS structure. The small–signal bias applied to the gate, $v(\mathrm{t})$, is distributed in the semiconductor and the dielectric according to

$$v(\mathrm{t}) = v_0 + \delta v = \frac{Q(\mathrm{t})}{C_{\mathrm{diel}}} + \phi_{\mathrm{s}}(\mathrm{t}). \tag{3.9}$$

We can evaluate the variation due to the small–signal by taking the time derivative of Eq. (3.9):

$$\frac{\mathrm{d}v(\mathrm{t})}{\mathrm{dt}} = i\omega\,\delta v = \frac{i(\mathrm{t})}{C_{\mathrm{diel}}} + i\omega\,\delta\phi_{\mathrm{s}} \tag{3.10}$$

from which we can write

$$\delta v(\mathrm{t}) = \left[\frac{1}{Y_{\mathrm{it}} + i\omega\,C_{\mathrm{depl}}} + \frac{1}{i\omega\,C_{\mathrm{diel}}}\right] i(\mathrm{t}). \tag{3.11}$$

The model of the full MIS device is therefore the parallel circuit of the depletion capacitance and the admittance of the interface states, in series with the dielectric capacitance. This is illustrated in Fig. 3.1b.

In the derivation of the admittance of the interface defects Y_{it}, we assumed all traps to be located at the same position in the energy bandgap (single–level approximation). It is possible to extend this model to an ensemble of interface states distributed over a range of energy below the semiconductor conduction band. In this case, each level j contributes with its characteristic admittance $\mathrm{Y_{it,j}} = 1/\mathrm{R_{it,j}} + i\omega\,\mathrm{C_{it,j}}$, and the total admittance is the integral over all active states. In terms of our equivalent circuit model, we can model the ensemble of trap states as a parallel circuit of many single contribution $\mathrm{Y_{it,j}}$, as shown in Fig. 3.1c.

Finally, we need to extract the quantity we are interested in, Y_{it}, from the measurement data. As mentioned in Chapter 2, the result of an impedance measurement is a couple of real numbers that describe the complex impedance of the sample. For MIS structures we use a parallel model, which means that we measure the quantities $\mathrm{G_m}$ and $\mathrm{C_m}$ that define the complex admittance $\mathrm{Y_m} = \mathrm{G_m} + i\omega\,\mathrm{C_m}$. From this data it is easy to correct for the dielectric capacitance, which must be measured accurately and used as a parameter. In this way, we obtain the parallel capacitance and conductance $\mathrm{G_p}$ and $\mathrm{C_p}$, and the equivalent model of the MIS structure is shown in Fig. 3.1d. At this point, we can extract the interface defects admittance from our measurement using the following equations:

$$\begin{aligned} \mathrm{C_p} &= C_{\mathrm{depl}} + \frac{C_{\mathrm{it}}}{1+\omega^2\tau_{\mathrm{it}}^2} \\ \frac{\mathrm{G_p}}{\omega} &= \frac{C_{\mathrm{it}}\omega\tau_{\mathrm{it}}}{1+\omega^2\tau_{\mathrm{it}}^2}. \end{aligned} \tag{3.12}$$

The first equation is the basis of the Terman method, which is discussed in Section 3.1.2. We already note that this approach requires to calculate the depletion capacitance, for which a theoretical model is needed. Also the doping profile must be known and used as a parameter. In the case of an inhomogeneous doping, the calculation becomes more difficult and numerical methods might be necessary [64]. On the other hand, the conductance depends only on

interface defects properties. G_p is divided through the angular frequency in order to obtain symmetric peaks as a function of frequency. The method based on the analysis of the conductance is described in Section 3.1.3.

3.1.2 The Terman or high frequency method

The goal of the Terman method is to extract the density of interface traps from the measurement of the CV of the device [65]. This technique relies on a major simplification of the model in Fig. 3.1b, known as the high frequency approximation, which consists of neglecting the admittance Y_{it}. In other words, we assume that the frequency is so high that no trap responds to the AC signal during the sweep. The equivalent model is therefore a series of the dielectric capacitance and that of the depletion region only, whose capacitance C_{HF} is given by

$$C_{\mathrm{HF}} = \left(\frac{1}{C_{\mathrm{diel}}} + \frac{1}{C_{\mathrm{depl}}} \right)^{-1}. \tag{3.13}$$

In this case, the information about the interface defects can be indirectly extracted from the behavior of the semiconductor depletion capacitance [38]. In fact, this method is based on the comparison of the measurement with a simulated, ideal curve. The capacitance of the depletion region and that of the interface states are functions of the band bending. It is possible to simulate the ideal curve in absence of trap states, $C_{\mathrm{depl}}(\phi_{\mathrm{s}})$, from the device and material properties [38]. Subsequently, from $C_{\mathrm{depl}}(\phi_{\mathrm{s}})$ we can derive the dependence of C_{HF} on ϕ_{s} with Eq. (3.13). An example is shown in Fig. 3.2a. The CV measurement provides the experimental curve $C_{\mathrm{HF}}(V_{\mathrm{gate}})$, as shown in Fig. 3.2b. With such information we can extract the real surface

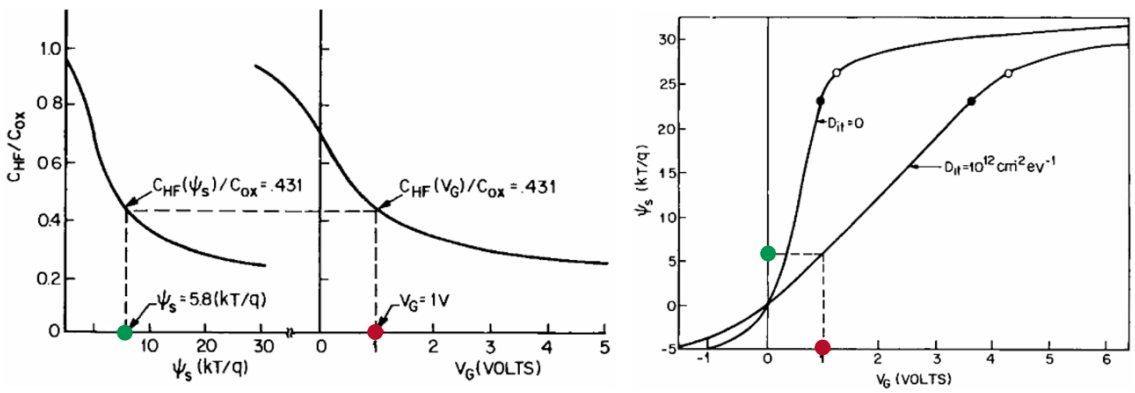

(a) (b) (c)

Figure 3.2. The simulated, ideal ($D_{\mathrm{it}} = 0$) capacitance as a function of the surface potential, in the high frequency approximation (a) and the measured CV curve, $C_{\mathrm{HF}}(V_{\mathrm{gate}})$ (b). These two curves allow us to calculate the real surface potential $\phi_{\mathrm{s}}(V_{\mathrm{gate}})$, to be compared with the ideal one (c), from which D_{it} can be extracted (from [38]).

potential as a function of the gate bias, as shown in the example of Fig. 3.2c. We note that the presence of interface states results in a stretch–out with respect to the ideal curve.

The density of interface states, D_{it}, can be calculated from the data in Fig. 3.2. We consider again the charge balance in the MIS structure of Eq. (3.6). The voltage drop at the gate contact is the difference between the applied bias and the band bending of the semiconductor, therefore the total charge can be written as

$$Q_{\mathrm{gate}} = C_{\mathrm{diel}}\left(V_{\mathrm{gate}} - \phi_{\mathrm{s}}\right). \tag{3.14}$$

The charges of the depletion region and that of the interface traps are functions of the surface potential through their respective capacitances:

$$Q_{\mathrm{depl}} = C_{\mathrm{depl}}\,\phi_{\mathrm{s}} \qquad \text{and} \qquad Q_{\mathrm{it}} = C_{\mathrm{it}}\,\phi_{\mathrm{s}}. \tag{3.15}$$

For a small change of the applied gate bias, we can write

$$C_{\mathrm{diel}}\,\mathrm{d}V_{\mathrm{gate}} = \left[C_{\mathrm{diel}} + C_{\mathrm{it}}\left(\phi_{\mathrm{s}}\right) + C_{\mathrm{depl}}\left(\phi_{\mathrm{s}}\right)\right]\mathrm{d}\phi_{\mathrm{s}} \tag{3.16}$$

from which we derive an expression for the interface trap capacitance:

$$C_{\mathrm{it}}\left(\phi_{\mathrm{s}}\right) = C_{\mathrm{diel}}\left(\frac{\mathrm{d}\phi_{\mathrm{s}}}{\mathrm{d}V_{\mathrm{gate}}}\right)^{-1} - C_{\mathrm{diel}} - C_{\mathrm{depl}}(\phi_{\mathrm{s}}), \tag{3.17}$$

where $C_{\mathrm{depl}}(\phi_{\mathrm{s}})$ is the simulated, ideal curve of Fig. 3.2a, and the derivative $\mathrm{d}\phi_{\mathrm{s}}/\mathrm{d}V_{\mathrm{gate}}$ can be calculated from Fig. 3.2c. This finally allows us to calculate the density of interface states as [38]

$$D_{\mathrm{it}}\left(\phi_{\mathrm{s}}\right) = \frac{C_{\mathrm{it}}\left(\phi_{\mathrm{s}}\right)}{q}. \tag{3.18}$$

In order to determine the energy of the trap states, an additional assumption is necessary. According to the Terman method, only the traps aligned with the semiconductor Fermi level are considered to contribute to the stretch–out of the capacitance curve. This would be possible only if the system under AC excitation reached a quasi–equilibrium situation, for which the position of the Fermi level remains constant and depends only on the value of the DC bias, V_{gate}. In other words, we assume that only the response of a trap located at $E_{\mathrm{CB}} - E_{\mathrm{t}}$ is in resonance with the small–signal applied to the gate. Such an approximation neglects the contribution of the DC bias to the trapping events at the interface. As we will discuss in the following sections, this can indeed result in an incorrect interpretation of the activation energy of the defects, and to an underestimation of the density of interface states. The energy diagram of this situation is shown in Fig. 3.3 for a n–type semiconductor in accumulation and depletion conditions. At each measurement point at a certain V_{gate} corresponds a value of the surface potential ϕ_{s}, at which we can calculate the density of interface traps D_{it} with Eq. (3.18) and their location in energy as

$$E_{\mathrm{CB}} - E_{\mathrm{t}} = \frac{E_{\mathrm{g}}}{2} - q\phi_{\mathrm{s}} - q\phi_{\mathrm{F}}, \tag{3.19}$$

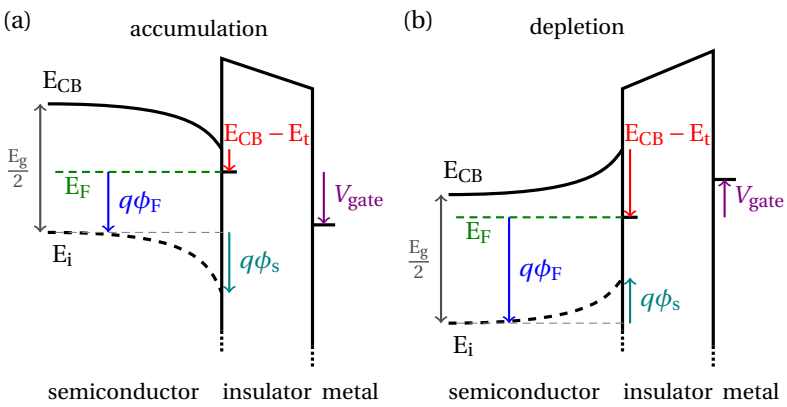

Figure 3.3. Band diagram of a MIS structure in accumulation (a) and depletion condition (b). The trap level at energy E_t below the conduction band edge is aligned with the Fermi level.

where E_g is the energy bandgap and ϕ_F is the Fermi potential, that can be estimated as

$$\phi_F = \frac{k_B T}{q} \ln \frac{N_d}{n_i} \tag{3.20}$$

where k_B is the Boltzmann constant, T the temperature, N_d is the doping profile of the semiconductor and n_i its intrinsic carrier density.

We apply the Terman method to the devices without the AlGaN barrier introduced in Section 2.1. The gate contact is realized on top of the dielectric layer, while the bulk is connected to the silicon doped layer buried into the GaN buffer, as shown in the cross section in Fig. 3.4a. We use two wafers, one of which has had an additional cleaning (a standard wet chemistry process) at the GaN surface before the deposition of the dielectric. Their high frequency capacitance characteristic are shown in Fig. 3.4b. The shape of the curve in depletion between –30 V and –20 V is due to the non uniform doping profile. In fact, at negative gate bias the depletion region grows in the semiconductor, and the depletion depth is proportional to the doping pro-

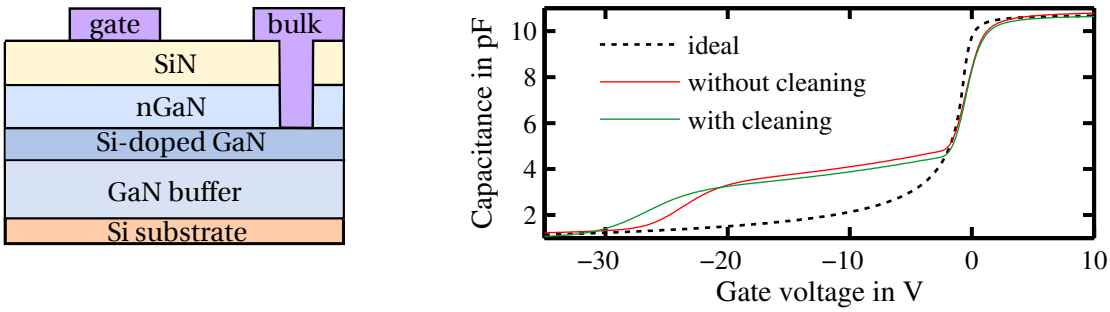

(a) (b)

Figure 3.4. (a) Cross–section of the GaN/SiN MIS structure with a silicon doped layer buried in the buffer. (b) High frequency (500 kHz) CV curves of the MIS devices on the two wafers, with and without the AlGaN surface cleaning. The ideal CV curve is also shown.

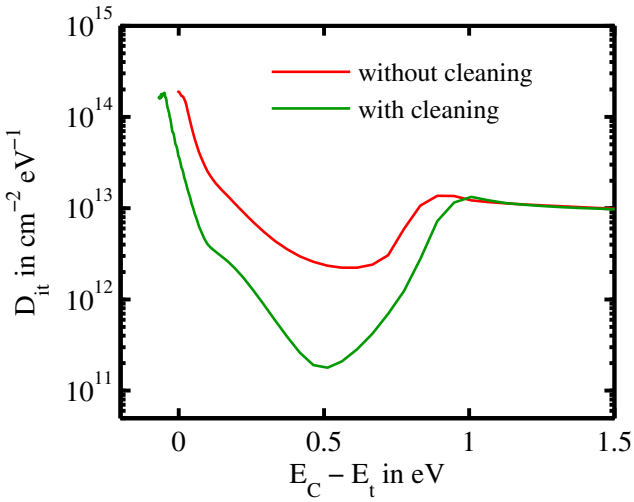

Figure 3.5. The density of interface traps as a function of the position in energy for the GaN/SiN structures, calculated with the Terman method.

file. The steeper part of the CV corresponds to the 10^{18} cm^{-3} Si doped layer, the rest to the UID GaN (dopant concentration 10^{16} cm^{-3}). This fact also explains the discrepancy between the measured curves and the ideal one, simulated using $N_d = 10^{16}$ cm^{-3}. We note that the CV of the structures with the additional cleaning is slightly steeper than the other one, which would imply a smaller amount of trapped charge. The results of the Terman analysis are shown in Fig. 3.5. We obtain a "U" shaped distribution close to the conduction band edge, with an average density of 10^{13} cm^{-2} eV^{-1}. The AlGaN surface cleaning appears to reduce the density of the traps around 0.5 eV of about one order of magnitude.

The first limitation of the Terman method is its dependence on parameters, namely the doping profile and the dielectric capacitance. The derivation of Eq. (3.18), which allows us to estimate D_{it}, assumes a uniform doping profile. It has been shown that an incorrect N_d value may cause an error of one order of magnitude in determining the density of interface states [66]. From Fig. 3.6a, we can see that also the shape of the D_{it} curve is affected. The same happens for the dielectric capacitance, for which the exact dielectric thickness has to be estimated or measured. In our case, the measured value of t_{diel} is 48 nm, while the nominal value is 50 nm. Discrepancies due to the SiN layer irregularities may result in the underestimation or overestimation of the D_{it}, as shown in Fig. 3.6b for a variation of 5 nm from the correct value.

A further, more serious limitation is the high frequency approximation. As we explained in the derivation of Eq. (3.18), we assume that the frequency used for the sweep is so high that no traps can follow the AC signal. This allows us to compare the measurement directly with the ideal curve. However, experimental evidence has shown that this interface presents traps with very small time constants, i.e., smaller than 100 ns [47]. It is clear that the high frequency approximation is not valid for these structures. Such a requirement might be met only at frequencies

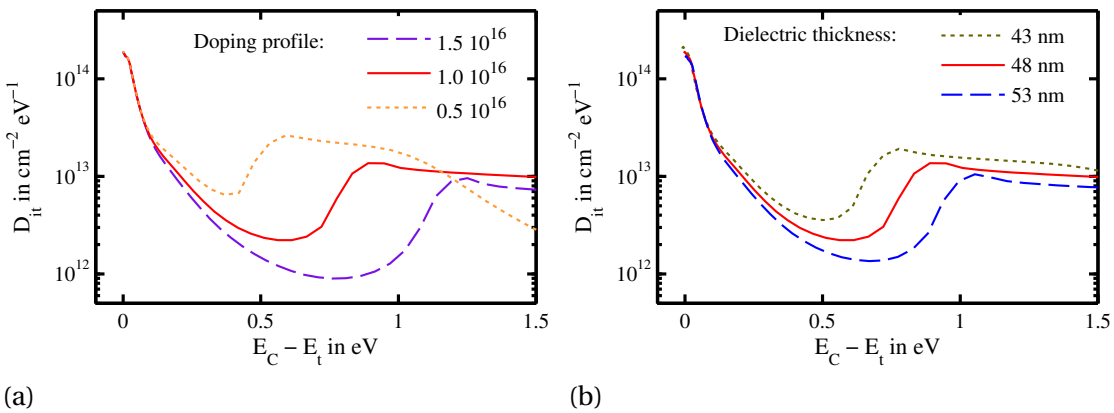

Figure 3.6. Impact of the parameters used for the D_{it} calculation with the Terman method, on the GaN/SiN sample without cleaning: doping profile (a) and dielectric thickness (b).

higher than 10 MHz, which would require a dedicated setup with RF probes. Nevertheless, the lower limit for the trapping time constant has not been measured, therefore even higher frequencies might be required.

In addition, this method is based on the assumption the Shockley–Read–Hall model through Eq. (3.4), which means that the traps accessible at a certain DC bias are capturing and emitting back all electrons following the AC signal. This would be true if the capture and emission time constants were identical for every defect state, namely $\tau_c = \tau_e$. In fact, if we describe this trapping behavior with a *capture–emission time* (CET) map, in which the amount of device degradation is plotted as a function of τ_c and τ_e, we would obtain a narrow stripe along the diagonal, and zero otherwise [27], as shown in Fig. 3.7a. On the contrary, the CET map for GaN–based devices shows that there are interface states with very different capture and emission time constants [47](see Fig. 3.7b). This means that some traps can capture an electron during the rising part of the AC signal ($\nu_0 + \delta\nu$), but they cannot emit it when the gate bias reaches again the baseline (ν_0). For this reason, the assumption of Eq. (3.4) is not adequate for our case.

The last and most important problem of the Terman method is that it cannot be applied to composite GaN/AlGaN structures. As we mentioned in Chapter 1, the presence of the AlGaN layer results in a small–signal behavior that cannot be modelled with the equivalent circuit described in Section 3.1. We will discuss in detail the role of the AlGaN barrier in Section 3.2.1, showing that the model of Fig. 3.1b should be fundamentally modified. It has been shown that the experimental CV curve can be simulated with a high degree of accuracy just by assuming the modified model, without additional interface traps [46]. Since one of the most important assumptions of the Terman method is not met, this method would lead to erroneous conclusions if applied to GaN/AlGaN MIS structures.

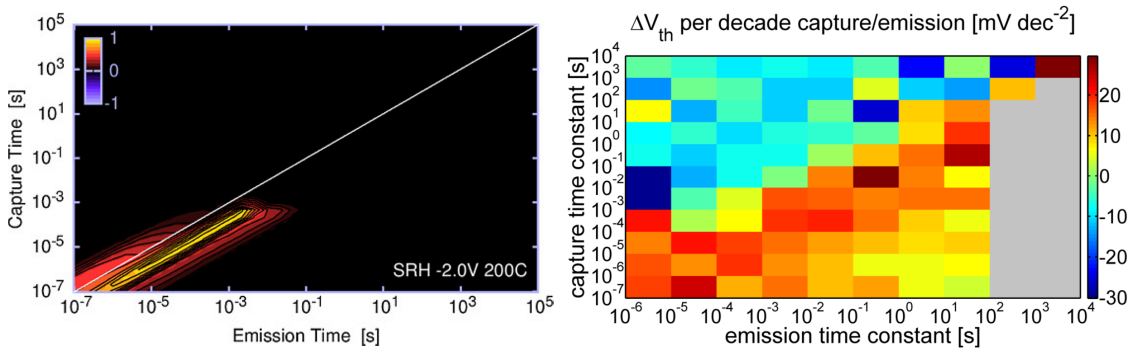

(a) (b)

Figure 3.7. (a) Simulated capture–emission time map for the Shockley–Read–Hall model (from [27]), and (b) measured CET map for GaN/AlGaN/SiN MIS–HEMTs (from [47]).

3.1.3 The conductance method

In Section 3.1.1 we derived the expression Eq. (3.12) for the parallel conductance, G_p, in the case of traps with a single energy E_t. It is possible to generalize it for an ensemble of traps distributed in energy, which is a better model of a real system. The integration is possible if we assume the density of traps and the capture probability, which can depend on the surface potential as $N_{it}(\phi_s)$ and $c_n(\phi_s)$, to vary smoothly in a range of few $k_B T/q$. This means that we consider N_{it} and c_n constant over a small variation of the surface potential. For this reason, the resolution in energy for D_{it} will be limited. With this assumption we can derive the equation [63]

$$\frac{G_p}{\omega} = \frac{C_{it}}{2\omega\tau_{it}} \ln\left(1+\omega^2\tau_{it}^2\right). \tag{3.21}$$

The quantities C_{it} and τ_{it} are extracted with a fit to the experimental curves, and the density of traps is then calculated with Eq. (3.18).

We calculate the parallel conductance from the measured data, G_m and C_m, with the equation

$$\frac{G_p}{\omega} = \frac{\omega C_{diel}^2 G_m}{G_m{}^2 + \omega^2 (C_{diel}+C_m)^2} \tag{3.22}$$

which gives symmetric G_p/ω peaks as a function of frequency, as shown in Fig. 3.8. At every gate bias we obtain a different peak, whose maximum value is proportional to the density of interface states and its resonant frequency is proportional to τ_{it}.

Similarly to the Terman method, we need to associate at each DC bias the energy of the trap which is in resonance with the AC signal, i.e., the one which is aligned with the Fermi level (see Fig. 3.3). The result of the conductance analysis on the GaN/SiN devices is shown in Fig. 3.9. We obtain the same order of magnitude of traps as with the Terman method, but a slightly different shape at energies around 1 eV. The device with the additional cleaning process shows a reduced trap density, although the difference is not as marked as in the previous results. In

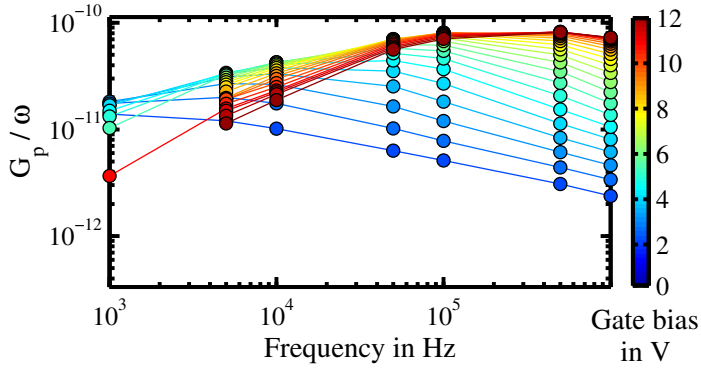

Figure 3.8. The parallel conductance as a function of frequency of the GaN/SiN structure without the surface cleaning. Each peak is measured at a constant DC bias value; here the data from 0 V to 12 V is shown.

addition, this technique reveals a drop of D_{it} at energies below –0.1 eV. Negative energies refer to trap states in the dielectric bandgap and above the semiconductor conduction band edge.

Differently from the Terman method, the conductance technique does not depend in the same way on the parameters used. The only parameter in Eq. (3.22) is the dielectric capacitance, which does not have a strong impact on the calculated G_p/ω peaks. In Fig. 3.10 we compare the results by using the measured dielectric thickness and variations of 5 nm, as we did in Fig. 3.6b. The difference in the result is less than the 6%, and this would not affect the D_{it} extraction.

However, in conductance measurements we should consider the impact of the series resistance. In fact, we can expect that our impedance measurement model is not fully described by a parallel circuit of C_m and G_m, but that also a certain resistance R_s in series is necessary,

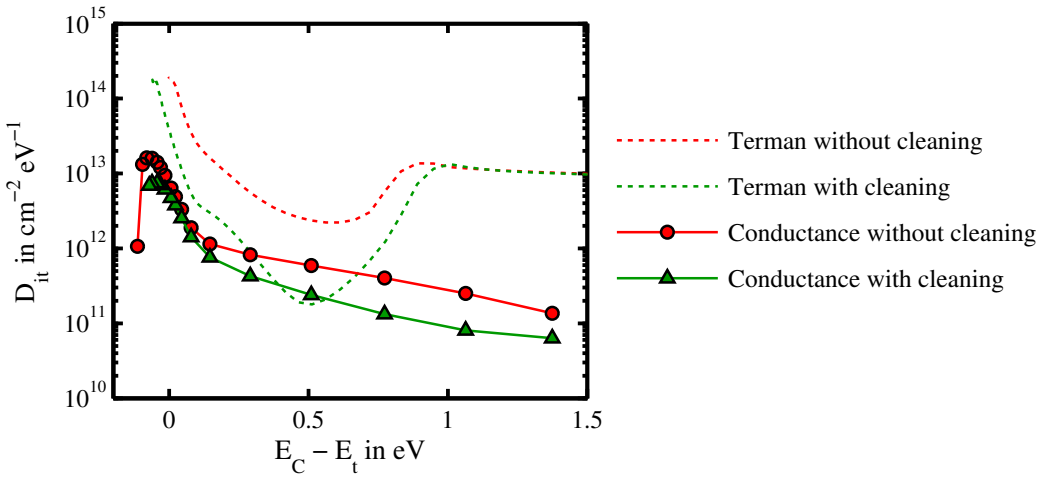

Figure 3.9. Density of interface states of GaN/SiN devices, calculated with the Terman and the conductance method.

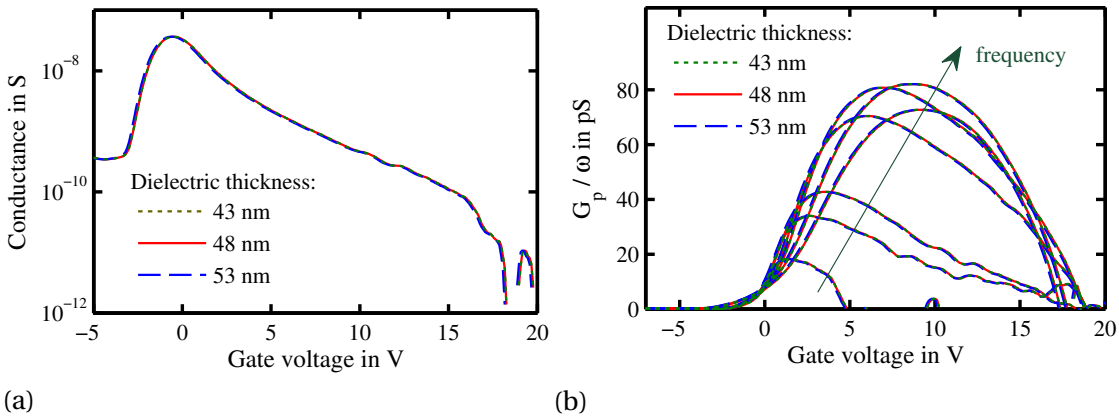

Figure 3.10. The value of the dielectric capacitance used in Eq. (3.22) does not have such a strong effect as for the Terman method. We obtain the same parallel conductance data at 10 kHz (a) and the G_p/ω peaks at all frequencies (b) using variations of the dielectric thickness of 5 nm from the measured value.

especially at high frequency. This accounts for leakage currents through the dielectric, and for the possible resistance arising from the bulk contact through the Si–doped layer. This can be seen in the measured G_m curves from their behavior at positive bias: the conductance peak over V_{gate} is not symmetric, but a larger value of conductance is reached, as shown in Fig. 3.11a. This is the typical effect of the series resistance [38], and can be corrected with the equations

$$\begin{aligned} C_{corr} &= \frac{C_m\left(G_m{}^2+\omega^2 C_m{}^2\right)}{a^2+\omega^2 C_m{}^2} \\ G_{corr} &= \frac{a\left(G_m{}^2+\omega^2 C_m{}^2\right)}{a^2+\omega^2 C_m{}^2}, \\ \text{with} \quad a &= G_m-\left(G_m{}^2+\omega^2 C_m{}^2\right)R_s \end{aligned} \tag{3.23}$$

where the series resistance R_s is evaluated with the high frequency approximation in accumulation conditions, where the response of the device is assumed to be described by the dielectric capacitance and the series resistance in series. On the contrary, the capacitance curves are not so severely affected. As a result of the correction with the appropriate R_s value, the G_p/ω peaks become symmetric. If the wrong series resistance is used, the shape of the curves can be very different. As one can see from Fig. 3.11b, this is true especially at high frequency, where the impact of the series resistance is larger. Such an artifact compromises the calculation of D_{it}, because the fit of the G_p/ω peaks with Eq. (3.21) would not converge in this case.

The conductance method suffers from the same limitation of the Terman method when applied to composite GaN/AlGaN structures. As we pointed out at the beginning of the present chapter, the foundations of this technique lie in the equivalent circuit model of Section 3.1.1. The presence of the AlGaN barrier causes the failure of such an assumption, as we will discuss in Section 3.2.1. For this reason, also this method is not adequate for GaN/AlGaN devices.

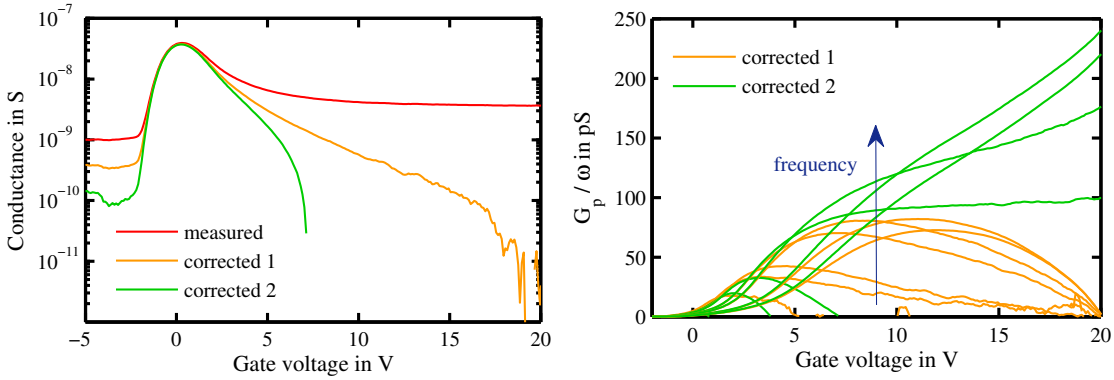

(a) (b)

Figure 3.11. The effect of the series resistance parameter in the correction of the parallel conductance data at 10 kHz (a) and of the G_p/ω peaks at all frequencies (b). The first correction (labeled "corrected 1") is made with the correct parameter, the second ("corrected 2") with a R_s value 15% off the real one.

Finally, a problem common to both methods consists in the dependence of the impedance characteristics on the measurement parameters, which will be discussed in detail in Section 3.2.2. In fact, we find that the CV and conductance curves at the same frequency can vary if the sweep rate is changed. An example is shown in Fig. 3.12. A slow sweep results in a stretch–out of the CV and a broader conductance peak. It is clear that the results from the Terman and the conductance method would be very different using the slow or the fast data. Moreover, such a behavior contradicts the assumption of thermal equilibrium. In other words, the trap states are not in resonance with the AC signal, capturing and emitting electrons following the small–signal oscillations, but the DC bias itself causes a time–dependent right shift of the threshold voltage. As a consequence, we cannot define the "baseline" of the surface potential $\phi_{s,0}$ and assume that the only change in time, $\delta\phi_s$, is due to the small–signal variation δv

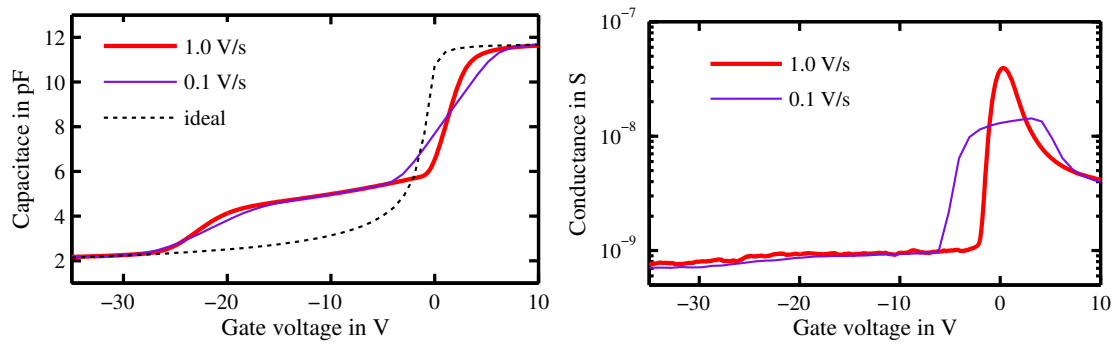

(a) (b)

Figure 3.12. CV curves (a) and conductance characteristic (b) at 10 kHz, taken with different measurement speed. The ideal CV curve for the Terman method is also shown.

of the gate voltage. Therefore, the measurements at various speed give very different results because the amount of trapped charge depends on the duration of the transients at each gate bias, which is longer the slower the sweep rate. The failure of this fundamental assumption causes the methods described in this section to give very questionable results even on GaN/SiN MIS structures. We must therefore conclude that the Terman and the conductance method are inappropriate for the characterization of interface traps in GaN–based devices, especially for composite GaN/AlGaN samples.

3.2 Impedance characteristics of GaN/AlGaN MIS structures

In this section, we focus on the two reasons why the main established methods are not adequate for our GaN/AlGaN MIS devices. In the first place, we investigate the role of the barrier, developing a new equivalent circuit model that can explain the observed frequency dispersion. Furthermore, we study in more detail the dependence of the impedance characteristics on the measurement parameters and the hysteresis of the devices with the standard interface.

3.2.1 The role of the AlGaN barrier

The study of the impedance characteristics of a composite GaN/AlGaN structure allows us to obtain an accurate insight into the different regions of operation of the device and its frequency response. As we can see in Fig. 3.13, from the capacitance– and conductance–voltage curves we can distinguish three main regions, indicated as depletion, 2DEG formation and spill–over.

When the gate bias is more negative than the threshold voltage, V_{th}, around –20 V in Fig. 3.13, the electrons of the 2DEG are pushed away from the GaN/AlGaN interface. This results in the creation of a depletion region, which extends in the semiconductor according to its doping profile. Since the generation time constant for holes is very large in wide bandgap materials, there are not enough minority carriers to form an inversion layer. As a consequence, at further negative gate voltages we never measure a constant inversion capacitance value, but we we are in *deep depletion* conditions.

Above the threshold voltage, the 2DEG is formed at the GaN/AlGaN interface. As we can see in the transfer characteristic in Fig. 3.13a, the device turns on and the electron flow between the source and drain contacts is possible. The capacitance almost abruptly reaches the plateau value $(\mathrm{C_{AlGaN}}^{-1} + C_{\mathrm{diel}}^{-1})^{-1}$, which is the result of the dielectric capacitance and that of the barrier in series. The conductance curve reflects the behavior of the displacement currents in the device. In Fig. 3.13b we can see a conductance peak in correspondence of the V_{th} value, which is the point at which the electron gas is formed.

At more positive gate voltages, starting from the spill–over voltage V_{so}, the capacitance increases towards C_{diel} and the conductance curve has another peak. This means that the electrons from the 2DEG found their way to through the AlGaN barrier to the interface with the

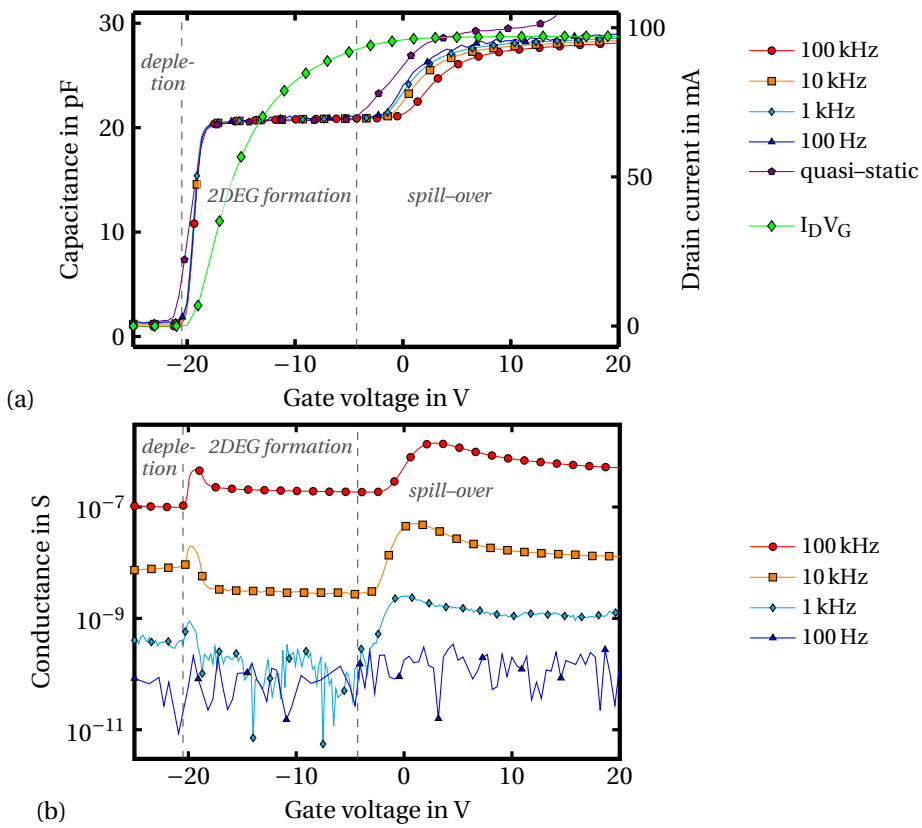

Figure 3.13. (a) Capacitance–voltage curve of a standard GaN/AlGaN/SiN MIS–HEMT at various frequencies. The quasi–static CV and the transfer characteristic at $V_{\text{drain}} = 2\,V$ are also shown. (b) The conductance–voltage curves at various frequencies for the same test structure.

dielectric. In fact, starting from the spill–over voltage, the edge of the conduction band at the AlGaN/dielectric interface is brought below the Fermi level, as shown in Fig. 3.14a. This results in the creation of a second electron channel. Interestingly, the AlGaN layer, which has a purely capacitive behavior below V_{so}, for more positive gate bias becomes conductive, thus allowing for electron transport from one side to the other. The GaN/AlGaN/dielectric structure can therefore be described by the circuit model in Fig. 3.14b, the dielectric capacitance in series with a parallel circuit of C_{AlGaN} and the bias–dependent barrier resistance, R_{AlGaN}. Such an RC circuit responds to a small–signal excitation in a frequency dependent way. As a consequence, this trap–free model can already explain the frequency dispersion observed in Fig. 3.13, and the frequency dependence of the spill–over voltage. It is possible to reproduce the experimental data by fitting the barrier resistance as a function of the gate bias [46].

The observed spill–over voltage in impedance measurements also depends on the frequency used. The lower the frequency, the smaller V_{so} appears. In fact, the low frequency limit ($\omega \to 0$) of the circuit in Fig. 3.14b is the dielectric capacitance. In this case the barrier is "short circuited" and the dominant term is C_{diel}. On the other hand, the high frequency limit ($\omega \to \infty$) is the serial connection of the dielectric and the barrier capacitances, which explains the lower

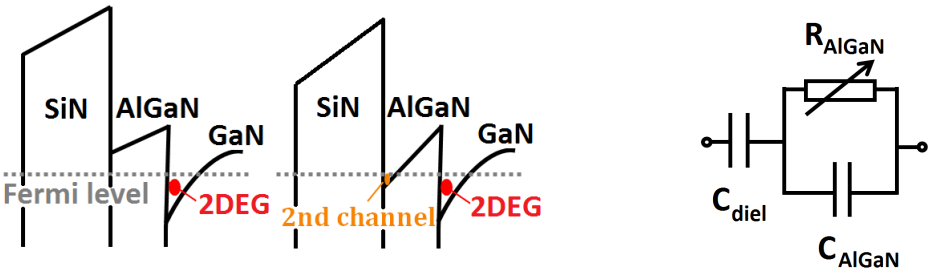

(a) (b)

Figure 3.14. (a) Circuit diagram model for a composite GaN/AlGaN MIS structure and (b) the conduction band edge diagrams before (left) and after (right) spill–over conditions (from [67]).

values of measured capacitance at high frequencies. For this reason, the most accurate way to determine the spill–over voltage is the quasi–static CV method: we directly measure the displacement current in the MIS structure by applying a small, linear increase of gate voltage. The incremental capacitance is proportional to the measured current. In order to calculate the capacitance of the device, we subtract the leakage current and integrate the result over time. The quasi–static CV curve obtained in this way is shown in Fig. 3.13a. As expected, this method provides the smallest value of the spill–over voltage. For the standard GaN/AlGaN/SiN structures, $V_{so} = -4\,\mathrm{V}$.

3.2.2 Dependence on measurement parameters

As we mentioned in Section 3.1.3, the impedance characteristics of the MIS–HEMT structures with a standard AlGaN/SiN interface show a strong dependence on the sweep rate. In this subsection we focus on the effect of the measurement parameters, varying the direction of the sweep, the oscillating amplitude, the sweep rate and the start and stop gate bias values.

By changing the direction of the sweep we investigate the hysteresis of the device characteristics. We perform a series of measurements on a number of fresh devices starting at 0 V, reaching a final gate bias value V_g^* (towards positive and negative voltages) and returning back to zero. The results are shown in Fig. 3.15a: the first part of the sweep is along the green curves, the return sweeps are in color, blue scale for $V_g^* > 0\,\mathrm{V}$ (5 V, 10 V, 15 V) and red scale for $V_g^* < 0\,\mathrm{V}$ (−10 V, −20 V, −30 V). We observe hysteresis along the whole gate bias axis, and the device status at the end of one cycle is different from fresh conditions. This can be seen clearly in the different capacitance value at 0 V before and after the hysteresis cycle with $V_g^* = -30\,\mathrm{V}$.

Furthermore, if we repeatedly sweep the gate bias between zero and V_g^* we observe a progressive shift of the CV curve, towards more positive voltages if $V_g^* > 0$ and towards more negative voltages if $V_g^* < 0$. In Fig. 3.15b we use $V_g^* = 10\,\mathrm{V}$ and we switch the bias twenty times. The curves labeled "fresh" are the first and the last sweep in the same direction, taken on a fresh device. We obtain a positive shift of about 5 V. Leaving the device floating results in a partial

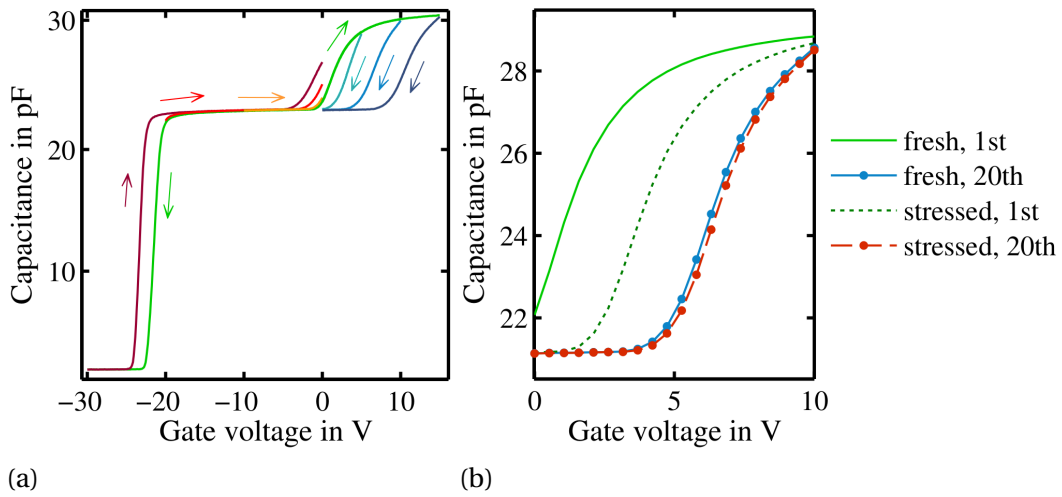

Figure 3.15. (a) Hysteresis of the CV curves of GaN/AlGaN/SiN devices. (b) Repetitive cycles between 0 V and 10 V, for a fresh device and after few minutes in floating conditions. Only the first and the last curves are reported (from [67]).

recovery of the voltage shift, as shown by the repetition of this experiment on the same device after some minutes (the two curves labeled "stressed"). We also note that the final sweeps (labeled "20th") are very similar. This means that a sort of saturation is reached, at least apparently, by repeating many times the same gate bias sweep. However, the final position of the CV curve depends on the V_g^* used, and it starts recovering as soon as the device returns to floating conditions.

In order to understand the impact of the sweep direction in more detail, we perform the following experiment with the lock–in amplifier. We apply an increasing or decreasing gate bias sweep in a staircase pattern. This means that we hold each bias value for a time t_{max}, and then we instantaneously switch to the next value. From the capacitance transients at each gate voltage we extract the value at time t_{extr}, and use it to build the whole CV curve. The results for different choices of t_{max}, t_{extr} and for positive ("up") and negative ("down") sweep directions are shown in Fig. 3.16. We use a fresh device for every measurement. Using a shorter or longer duration for each bias step t_{max} has the same effect on the sweeps in different direction, resulting in a certain positive shift for every point of the CV curve (see Fig. 3.16a). In fact, we apply only positive gate voltages, for which a positive shift of the capacitance characteristic is observed. This is due to electron capture, and in this case the capacitance transients at every gate bias step decrease as a function of time. For this reason, even if the extraction time t_{extr} is always the same, the longer the device has been at positive bias, the larger is the accumulated positive shift. This explains also the distortion of the curves when t_{max} gets longer. On the other hand, using the same t_{max} but different extraction times t_{extr} we obtain the opposite behavior in the "up" and "down" sweeps, as we can see in Fig. 3.16b. In the former case, we observe a decrease

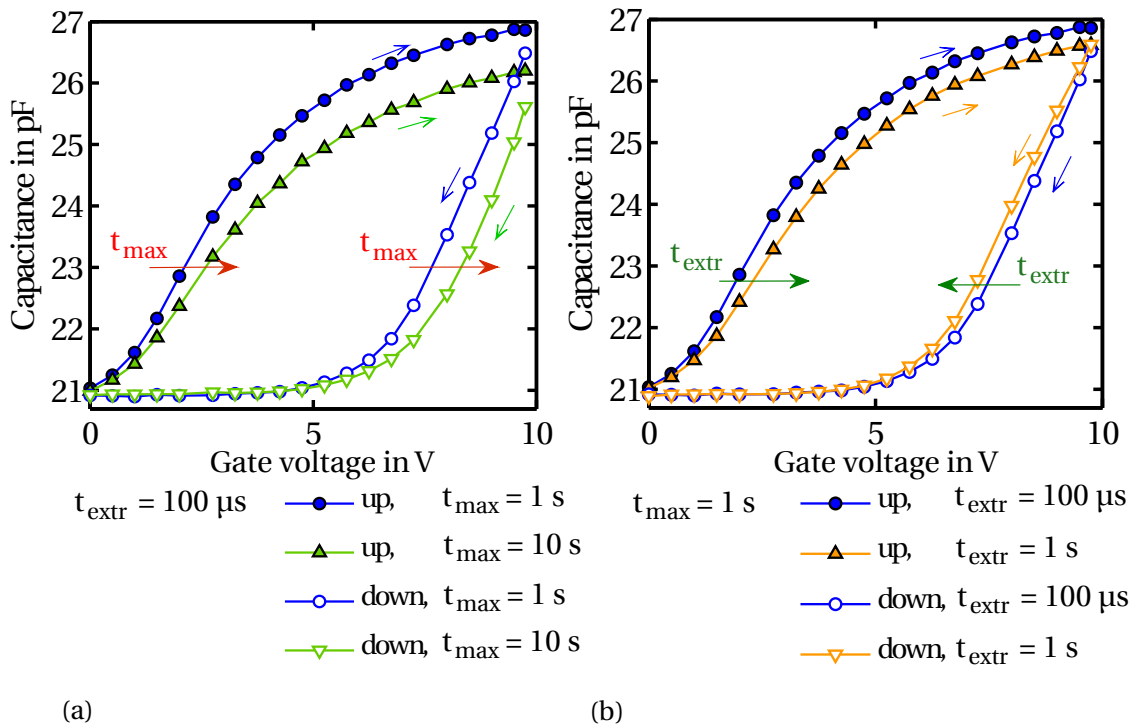

Figure 3.16. CV curves extracted from the staircase voltage pattern with the lock–in amplifier. (a) Each bias step is held for a time t_{max} *= 1 s or* t_{max} *= 10 s, and the capacitance is always extracted at* t_{extr} *= 100 µs. (b) Each step duration is* t_{max} *= 1 s and the extraction time is* t_{extr} *= 100 µs or* t_{extr} *= 1 s. In both cases the comparison of the positive (up) and negative (down) sweep direction is shown (from [67]).*

of capacitance as a function of time for every gate voltage step. A longer t_{extr} therefore results in a larger positive shift. If the sweep direction is negative instead, the capacitance transients increase in time, because some electron emission takes place at lower gate voltages. In this way, each bias step allows some recovery from the previous one. There are two competing effects: the electron capture due to the application of forward gate bias, and the electron emission because of the continuous reduction of the gate voltage. As a consequence, waiting for a certain time t_{extr} at each bias step lets these two effects balance each other out, thus minimizing the effect of trapping and detrapping during the measurement of the CV curve.

Among the measurement parameters that have an impact on the shape of the CV and conductance curves, we have discussed the frequency of the AC signal, the sweep direction and the sweep rate. Other important quantities are the oscillator level and the voltage extrema of the sweep. Fig. 3.17 compares the impedance characteristics measured with frequency 10 kHz, oscillator level 500 mV, sweep rate 1 V/s, starting from –30 V and stopping at 20 V with the curves obtained by changing one parameter at a time. We conclude that the impedance characteristics depend strongly on the measurement parameters. This is due to the fact that the structure does not reach the quasi–equilibrium conditions required to apply the small–signal

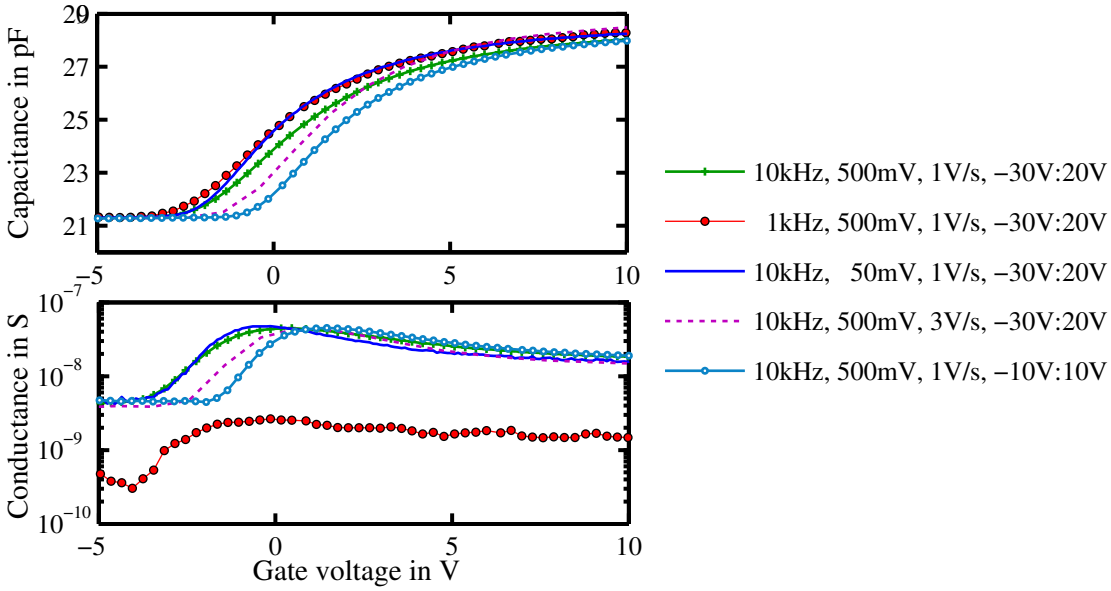

Figure 3.17. Capacitance and conductance characteristics measured with different values of frequency, oscillator level, sweep rate and start and stop voltage. Only the part from –5 V to 10 V is shown in order to focus on the differences in the spill–over region. The parameters used are indicated in the legend.

approximation. This means that the trap states are not in resonance with the AC signal, capturing and emitting electrons following the oscillations, but that the DC bias itself causes a time–dependent shift of the threshold voltage, which is very sensitive to the measurement parameters listed above.

Even if the impedance characteristic cannot be directly analyzed to extract information about the trap states, we can compare the characteristics of a device before and after the application of stress, provided that the measurement parameters used are constant. For example, in Fig. 3.18a and b the capacitance and conductance curve before and after a transient at 10 V for 100 s are shown. We note that there are two regions where the two curves differ the most, that we call C_1 and C_2 for capacitance and G_1 and G_2 for conductance. This is clarified in Fig. 3.18c, where the difference of the two curves is shown. We calculate the voltage shift in the following way: for every gate bias point of the stressed curve, V_{str}, we have a capacitance C^*. We find the same value C^* in the fresh curve and interpolate the relative gate bias V_{fresh}. The difference between V_{str} and V_{fresh} gives the total voltage shift ΔV, which is reported in Fig. 3.18d, labeled "from C_1" and "from C_2". We also calculate ΔV from the position of the conductance peak, by taking the difference of the gate biases where the peak has its maximum. The result is shown in Fig. 3.18d, labeled "from G_1" and "from G_2". The density of interface states ΔN_{it} is calculated with Eq. (1.1) and is estimated to be slightly less than 10^{12} cm^{-2}. We note that in the first region, around the threshold voltage, a parallel shift occurs. Furthermore, the comparison of capaci-

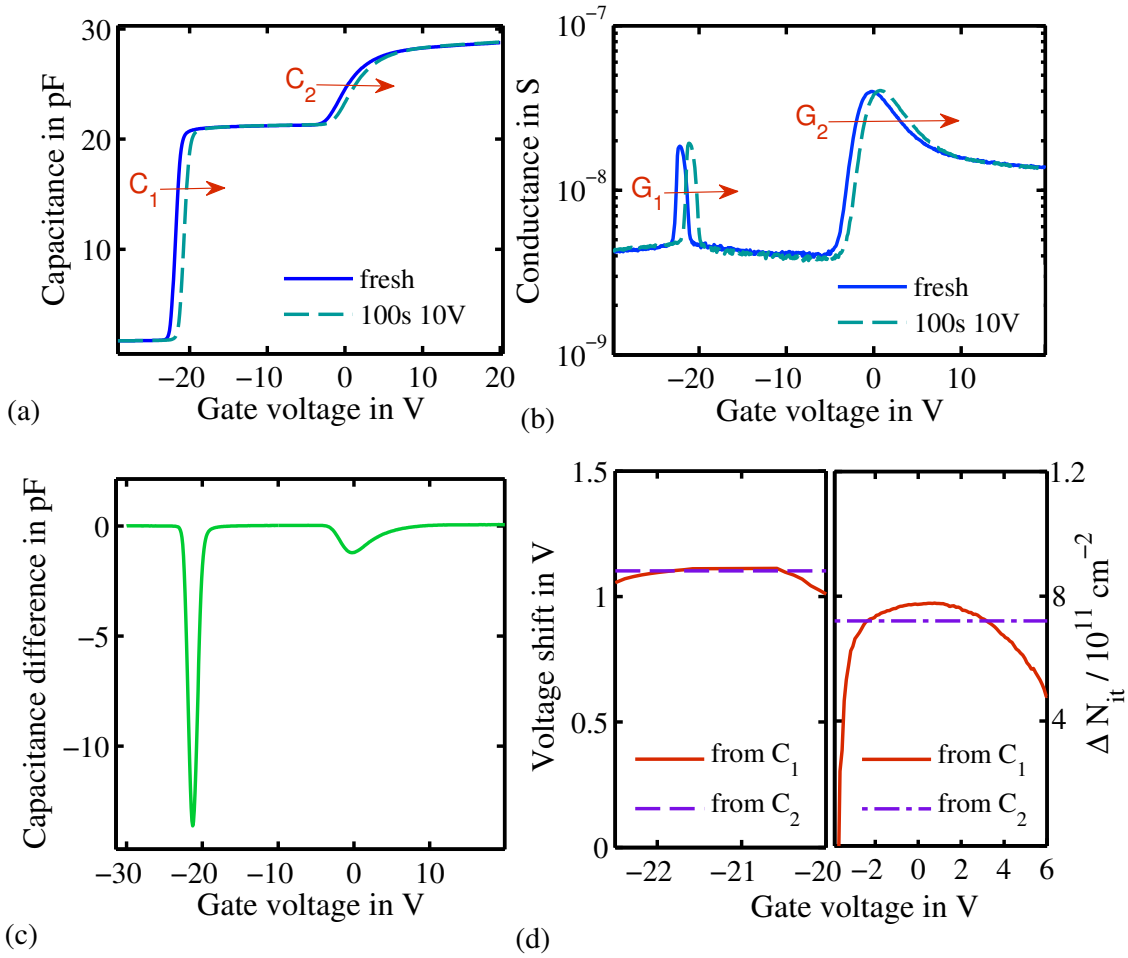

Figure 3.18. Capacitance (a) and conductance (b) characteristics before and after 100 s at 10 V. The difference between stressed and fresh curves determines the two regions where ΔV can be calculated (c). The voltage shift (d) is calculated from the capacitance curve (solid line) and from the position of the conductance peaks (dashed lines). The corresponding density of traps at the interface ΔN_{it} is shown on the right axis (from [67]).

tance and conductance curves gives the same information. On the other hand, the ΔV from the capacitance curve in the second region, around the spill–over, shows a rising and falling behavior. This is due to the slight distortion of the CV curve after stress. In fact, the rather high stress level of 10 V for 100 s can change the charge state of the interface and result in a different shape of the CV curve.

First, we test this approach by comparing a fresh and a stressed device after a fake "stress" where only the AC bias is applied for 100 s. We investigate the impact of the measurement parameters by repeating this experiment with the same variations used in the previous paragraph. The results are shown in Fig. 3.19a: the extracted voltage shift is always zero, as expected. This means that the small–signal alone does not wear out the device. Furthermore, this proves that the device to device variation is small enough to be neglected.

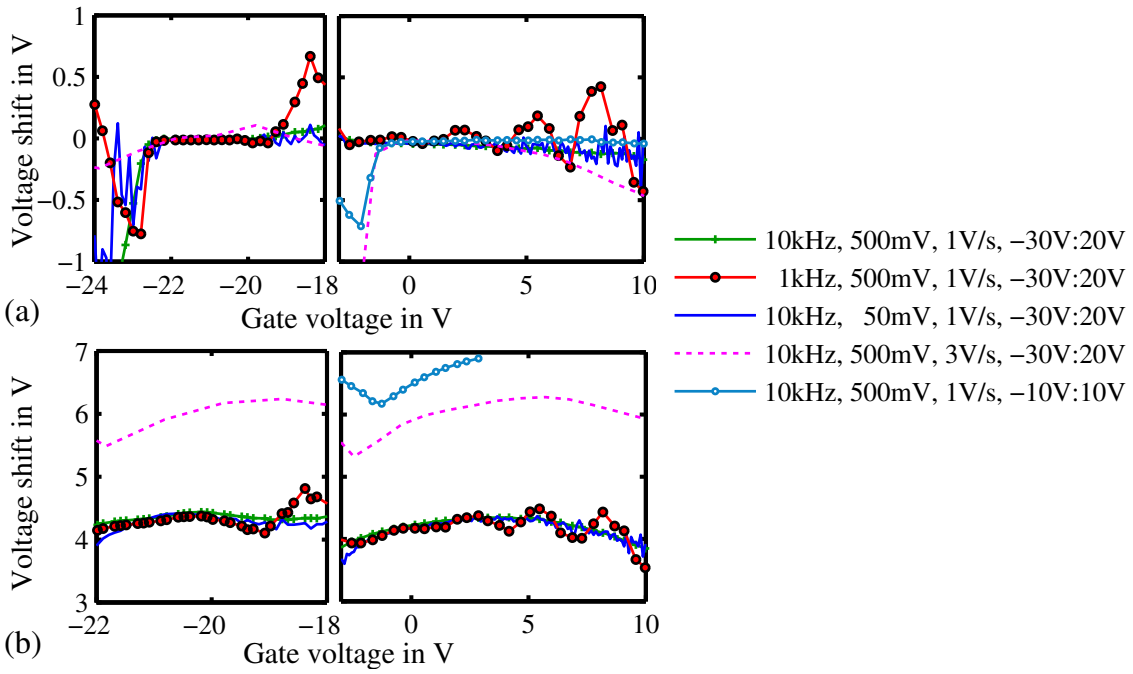

Figure 3.19. The voltage drift after 100 s at 0 V for various measurement conditions is zero in all cases (a). The voltage drift after 100 s at 10 V stress (b) instead varies for different DC bias sweeping conditions like the sweep rate and start and stop bias values (from [67]).

The second step consists in applying a real stress to the devices. Interestingly, in this case we find a strong dependence on some measurement parameters. Fig. 3.19b shows the ΔV after a stress of 100 s at 10 V. The result does not change when we vary the small–signal parameters, like the frequency and the oscillator level. Using a sweep rate three times larger, or starting the sweep from −10 V instead of −30 V results in a variation of the extracted voltage shift of about 40%. We must conclude that the measurement parameters impact not only the shape of the impedance characteristics of the device, but they can have a larger influence than a stress transient of 10 V applied for 100 s. This simple approach of ΔV evaluation therefore is not reliable since the measurement itself conceals the effect of the stress. For this reason, we must develop a characterization method that enables us to evaluate the device degradation as accurately as possible. We present two such methodologies in the next section.

3.3 Voltage shift methods

In this section we present two methods to evaluate the voltage shift during positive gate bias stress of a MIS–HEMT device. We rely on impedance measurements in order to be sensitive to the voltage drift in the spill–over region, where the second increase of capacitance and the second conductance peak are observed. However, our aim is to investigate the voltage shift due to the applied DC gate bias during a stress transient. Capacitance measurements have

been used in a similar way to investigate the bias temperature instability (BTI) of silicon devices [68]. First, we describe an approach based on the comparison of the CV characteristic before and after stress, the *measurement–stress–measurement* (MSM) method. Secondly, we propose an "on the fly" method that enables us to evaluate the voltage shift directly during the stress transient, the *capacitance–on the fly* (C–OTF) method.

3.3.1 The measurement–stress–measurement (MSM) method

In the previous section, we have shown that the impact of the sweep for characterizing the device can have a larger impact than the actual stress transient. For example, a longer time at negative bias reduces the extracted ΔV, since $V_{\text{gate}} < 0$ constitutes a recovery condition from a forward bias stress. For this reason, we apply a method that allows the comparison between fresh and stressed conditions without taking the impedance characteristic over the whole voltage range. Instead, we optimize the starting voltage, indicated as V'_{G}, to a value included in the C_1 region, where the capacitance has the steepest increase and therefore the sensitivity to the voltage shift is maximized. This approach is therefore a *measurement–stress–measurement* (MSM) method [69, 70], already extensively used in the study of voltage drifts in silicon, silicon carbide as well as in gallium nitride transistors [47, 71, 72]. A schematic illustration of the MSM method is shown in Fig. 3.20.

It is clear that a V'_{G} value close to the threshold voltage is still a recovery condition for the device, compared with the stress transient at positive gate bias. This is the main drawback of this method, which consists in the inevitable underestimation of the ΔV because of the intermediate recovery at the read–out voltage V'_{G}. However, by optimizing the starting voltage and reducing the measurement delay we can find a trade–off between the accuracy in extracting the voltage shift and the underestimation error.

We investigate the impact of the measurement delay using the lock–in amplifier. In this way we can achieve a delay as short as 1 ms, and we compare the result with a second measurement

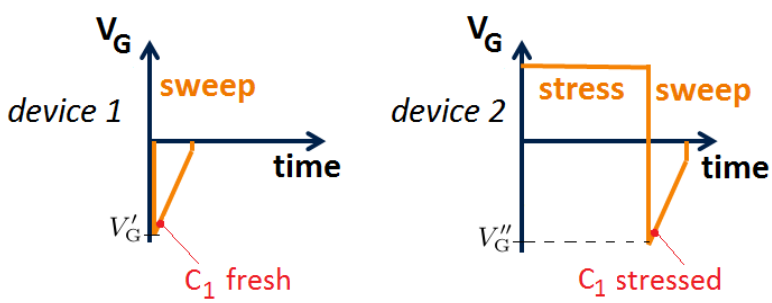

Figure 3.20. Schematic illustration of the experimental procedure of the MSM approach. The sweep before and after stress is aimed to measure a capacitance value C_1 in the steepest part of the CV, close to the threshold voltage of the device (from [67]).

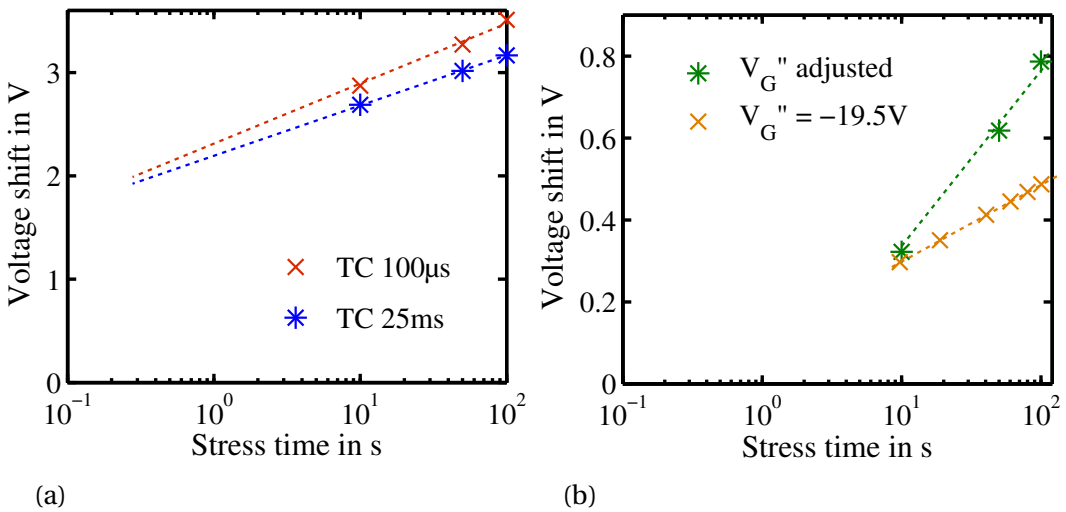

Figure 3.21. Application of the MSM method to MIS–HEMTs with a standard interface. We study the impact of the measurement delay (a), from the smallest value possible with the lock–in amplifier, 1 ms, to the typical delay of an impedance analyzer, 250 ms. Furthermore, we investigate the effect of using always the same $V'_G = -19.5$ V, instead of optimizing V''_G as described in the text (b). The dashed lines are just a guide to the eye.

with delay 250 ms, that is the typical value for a standard impedance analyzer setup. As we can see from Fig. 3.21a, a longer waiting time at negative bias results in a smaller value of ΔV. In the case considered here, this effect can influence the result up to 10% for the MIS–HEMTs with standard interface.

Furthermore, we must take into account that the threshold voltage shifts during stress. It is not uncommon to reach several volts of shift, therefore we might miss the C_1 region when we use the same V'_G before and after stress. As a consequence, it is necessary to optimize the starting voltage for the measurement after stress, especially after a long one, to a value V''_G which is ideally equal to $V'_G + \Delta V$. As the voltage shift is not known a priori, preliminary measurements might be required to determine the best starting voltage for a certain stress. Fig. 3.21b shows the impact of using always the same V'_G instead of choosing the proper value of V''_G. Since the sweep direction is positive, eventually we measure the desired C_1 region, but the time spent at negative bias before reaching it has the same effect as a long time delay. The consequence is an additional underestimation of the voltage shift, which is more severe the longer the stress duration. For this reason, the slope of the ΔV curve as a function of the stress time is affected.

In conclusion, the MSM method allows an accurate extraction of the voltage shift when all the relevant measurement parameters are optimized. Nevertheless, we must be aware of the fact that the extracted ΔV is always underestimated.

An additional, important observation regarding the application of this method at different temperatures can be made at this point. As we will see in the next chapters, the temperature de-

pendence of the device degradation is a key factor in understanding the physical mechanisms responsible for it. We are therefore interested in comparing the voltage drift data at various temperatures. However, both trapping and detrapping events generally depend strongly on temperature. Given the experimental restrictions, an MSM test would typically be carried out at a constant temperature. The stress transient and the recovery during the read–out phase will therefore have the same temperature, unless special devices for fast temperature switching were used. For example, this has been possible for silicon devices by means of the poly heater, a structure of two polycrystalline silicon wires in close contact with the device under test, that allows swift temperature changes [73]. If the temperature is the same during stress and recovery, the MSM method suffers from additional drawbacks. In the first place, the shape of the CV curve depends on temperature, therefore also the proper values of V'_G and of V''_G are temperature dependent. These values must be carefully evaluated in order to make the direct comparison of measurement at different temperatures possible. Moreover, the effect of the recovery during the time delay would also be temperature dependent. This means that the underestimation error in the extracted ΔV changes with temperature as well. As a consequence, it is very challenging to determine the real dependence of the device degradation on temperature. A solution can be found by separating the trapping and detrapping events, by focusing on the stress transients only. This is the basic concept of the method presented in the next paragraph.

3.3.2 The capacitance–on-the-fly (C–OTF) method

The idea of an "on the fly" method is to evaluate the device degradation directly during the application of a stress voltage. This kind of approach has been developed for current–voltage experiments to investigate the BTI on silicon MOSFETs [69, 70]. In our case, the drain current transient of a GaN/AlGaN MIS–HEMT at positive bias would not allow us to accurately extract the voltage shift, because the current is close to the saturation value in this region of operation. On the contrary, the CV curve shows the second increase of capacitance when spill–over is reached, providing a high sensitivity to voltage shifts. By choosing a stress voltage V_{stress} in

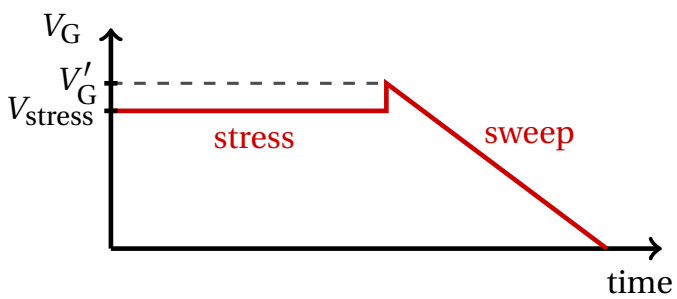

Figure 3.22. Schematic illustration of the experimental procedure of the C–OTF approach.

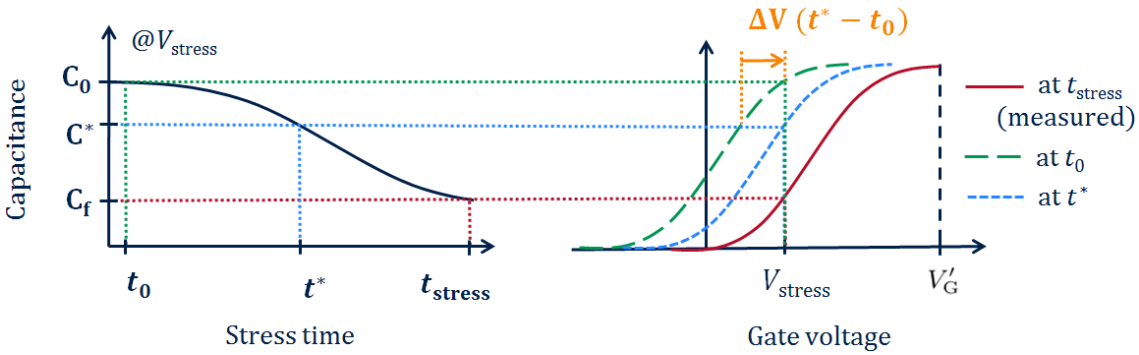

Figure 3.23. Illustration of the basic principle of the C–OTF method. After a stress transient (left) we measure the CV curve (right), which is used as a reference to calculate the voltage drift ΔV for each data point of the transient.

spill–over conditions, we can interpret the decreasing capacitance transient as a right shift of the whole capacitance characteristic. This can be done by comparing the capacitance value during stress with that of a reference CV curve, which is measured after the stress transient, as shown in Fig. 3.22. From the shift ΔV we can then calculate the density of active interface traps ΔN_{it} with Eq. (1.1).

Since the characteristic is taken after stress, the capacitance C_f corresponding to V_{stress} in the CV curve is the value at the last measurement point of the transient, at t_{stress}. Instead, the capacitance C_0 at the first measurement point, t_0, gives the position of the CV curve of the fresh device, as shown in Fig. 3.23 with the long dashed line. In a similar way, for every time t^* between t_0 and t_{stress} we can find the intermediate CV curve position, indicated by the short dashed line in the illustration. At this point, ΔV is calculated as the horizontal shift between the CV curve at t^* and that at t_0. Repeating this procedure for every data point of the transient we extract the time evolution of the device shift.

Obviously, the modalities of the CV reference measurement are of primary importance. We study in the first place the impact of the sweep direction. As we discussed previously in Section 3.2.2, at positive gate voltages a negative sweep direction allows the effect of electron capture and emission to partially balance each other out. This results in the CV curve having the least contribution of trapping during the sweep itself. For this reason, we choose to perform the reference CV curve measurement starting from a positive voltage, V'_G, going then down to zero. A clear argument in favor of this choice is the comparison of the temporal evolution of ΔV over two different values of stress duration, 5 s and 100 s. We expect our method to give consistent results in the portion of stress time in common with the two measurements. As we can see from Fig. 3.24, when we use a negative sweep direction ("down") our expectation is met. On the contrary, the positive ("up") sweep leads to a contradictory result. This is due to the fact that additional electron trapping takes place during the CV measurement, thus distorting the

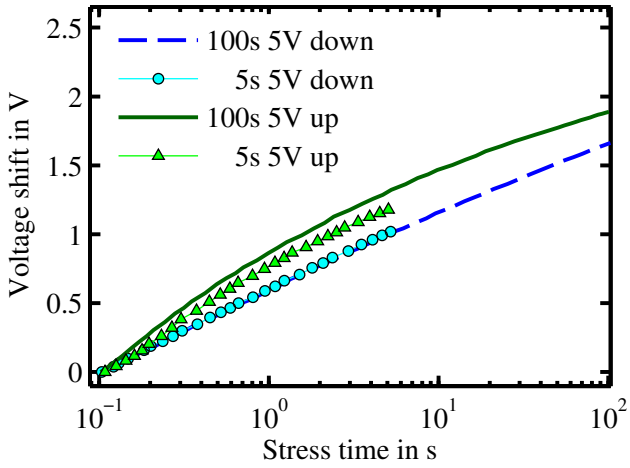

Figure 3.24. The time evolution of the ΔV calculated with the C–OTF method for different stress duration, and with CV references taken with positive and negative sweep directions (from [67]).

capacitance characteristic. As a consequence, the ΔV time evolution has a different shape for the two stress durations.

The starting voltage of the CV sweep is also very important. As we can see from Fig. 3.23, the value of V'_G must be larger than V_{stress} in order to allow for the calculation of the voltage shift. However, we have proven in Section 3.2.2 that a too large value might influence the shape of the CV curve to the point that the impact of sweeping dominates on that of the stress. The ideal starting voltage is in fact $V_{stress} + \Delta V$. For this reason, we must optimize it for every stress duration. We investigate the impact of varying V'_G for a stress of 5 V for 100 s. We use values slightly or much larger than V_{stress}, namely 5.5 V up to 14 V. The results are shown in Fig. 3.25. When the starting bias is much higher than stress, the additional trapping events during the sweep cause the distortion of the CV curve, that in turn results in an overestimated ΔV for long stress times. The larger V'_G, the larger the error on the slope of ΔV as a function of time. The error in this example is up to 20% at $t_{stress} = 100$ s. On the contrary, a too small difference between V_{stress} and V'_G does not allow to extract the voltage shift for the first part of the transient, as can be seen when we use $V'_G = 5.5$ V. As a consequence, a trade–off must be found. We must determine the voltage value that allows to extract the voltage shift for short stress time, while avoiding an excessive additional stress. This problem must be properly addressed in particular when the stress duration is very long, or for very small measurement delays. In fact, even if the first measurement point of an experiment with the lock–in amplifier is at $t_0 = 50\,\mu$s, the extraction of ΔV is not possible until about 10 ms. The data in Fig. 3.25 is measured with the impedance analyzer, which has a time delay of 250 ms. This is the reason why the first point does not decrease at larger V'_G. In this way the difference in slope is clearer in the figure.

We can distinguish three approximations made in the C–OTF method that limit its accuracy. In the first place, we assume a parallel shift of the CV curve as a whole during stress at positive

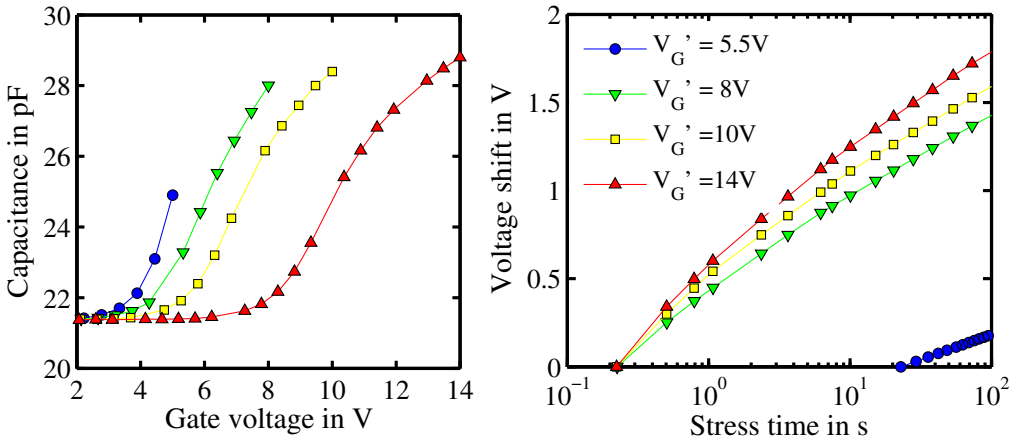

(a) (b)

Figure 3.25. Capacitance–voltage curves (a) and the extracted voltage drift (b) with the C–OTF technique for different values of V'_G. This data is measured with the impedance analyzer, with a time delay of 250 ms (from [67]).

bias. This might be imprecise for very long stress duration at large stress bias, or when a too large V'_G is chosen. The second approximation is to neglect the additional stress induced by a V'_G larger than the stress voltage. This effect contributes to the overestimation of the ΔV. Finally, the third limitation is the impossibility to determine the amount of voltage shift at the first measurement point, ΔV_0. In fact, we must assume that the CV curve of the device in fresh conditions is the one extracted from the first measurement point. However, the real value of capacitance right after stress is impossible to measure, because of the inevitable time delay of the instrument. In all time–resolved measurements we always observed a decreasing behavior, which means that the trapping phenomena causing the drift start playing their role before our time resolution of 50 µs. As a consequence, we arbitrarily set the unknown ΔV_0 of all C–OTF measurements to zero.

In conclusion, the C–OTF method allows us to evaluate the device degradation over time, extracting the voltage shift directly from the data measured during stress. The error due to the approximations used can be limited by choosing the proper parameters for the measurement of the CV characteristic, except for the inevitable effect of the experimental time delay, as for the MSM approach. In Chapter 5 we show a direct comparison of the two methodologies described in this Section (MSM and C–OTF) on different GaN–based samples. Furthermore, the C–OTF method enables the direct comparison of the results taken at different temperatures. In the next Chapter 4 we introduce some fundamentals about the modeling of the degradation mechanisms, that are then applied in Chapter 5 on C–OTF measurements on our test structures.

4

Modeling of charge trapping phenomena

CHARGE TRAPPING PHENOMENA are responsible for the threshold voltage instability of MIS–HEMTs structures under positive gate bias. In the previous chapters, we have focused on the experimental methodologies used to investigate these phenomena. At this point it is necessary to introduce a physical model for the mechanisms of trapping and detrapping. In this chapter we review briefly the Shockley–Read–Hall model and its shortcomings in explaining the experimental data. Subsequently, we give an overview of the non–radiative multiphonon theory that is used as the foundation for our data analysis. We describe the relevant parameters of the model and how to extract them from the data. We perform some simulations in order to highlight advantages and disadvantages of our approach, that will be finally applied to the measurement data on GaN–based devices in Chapter 5.

4.1 The Shockley–Read–Hall (SRH) model

The SRH model was first developed for defects in bulk semiconductors [74,75], then adapted for interface and oxide traps in MIS (and MISFET) structures by E. H. Nicollian and A. Goetzberger in 1966 [63]. The basic assumption is that the probability that a carrier at a trap energy E_t is captured (or emitted) is proportional to its thermal velocity v_{th} and a certain cross section σ.

Depending on the sign of the carriers in the channel, during operation we have a reservoir of electrons in the semiconductor conduction band (or holes in the valence band) which can charge the traps present in the *active energy region* (AER). The AER is that portion of trap states which can change their occupancy state during and after stress. This means that, if the traps in a nMOSFET are donor–like, they are above the Fermi level before stress (unoccupied) and below Fermi level with the application of the gate bias V_{stress} (thus trapping an electron). The contrary happens in the case of acceptor–like states in pMOSFETs. Let's assume that the defects are located inside the semiconductor bandgap, i.e., $E_t < E_{CB}$ and $E_t > E_{VB}$, where E_{CB} is the energy of the electrons at the conduction band and E_{VB} at the valence band edge. In this way,

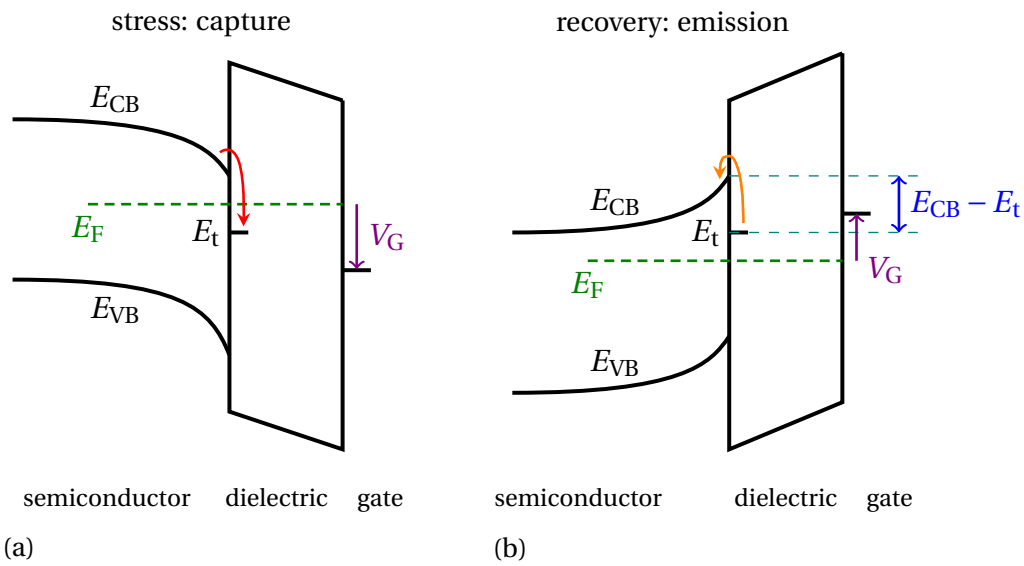

Figure 4.1. Band diagram of a n–type MIS structure during stress (a) and recovery (b). According to the SRH model, there is no energy barrier for electron capture (indicated by the red arrow on the left). On the contrary, for electron emission (orange arrow on the right) the additional energy $E_{CB} - E_t$ must be provided to the system.

there is no energy barrier for electron capture into donor–like traps (see Fig. 4.1a), and neither for hole capture into acceptor–like states. In this case, the capture rate is expressed simply by

$$\begin{aligned} k_{c,el} &= n\, v_{th}\, \sigma \qquad \text{or} \\ k_{c,h} &= p\, v_{th}\, \sigma. \end{aligned} \tag{4.1}$$

If no further assumptions on σ are made, the trapping process will be temperature independent. In this way, the temporal evolution during stress has a single time constant $\tau_c = 1/k_c$ at all temperatures, irrespective of the distribution of trap levels throughout the bandgap.

On the other hand, under recovery conditions the electron trapped in a donor–like trap can be emitted again, if the Fermi level falls below E_t. Similarly, holes captured in an acceptor–like trap are emitted if the Fermi level rises above E_t. The rate of emission differs from that of capture by a Boltzmann factor, depending on the difference of energy between the conduction band edge and the trap level $E_{CB} - E_t$ for electrons (see Fig. 4.1b), and $E_t - E_{VB}$ for holes, following the equations

$$\begin{aligned} k_{em,el} &= N_C\, v_{th}\, \sigma\, e^{-(E_{CB}-E_t)/k_B T} \\ k_{em,h} &= N_V\, v_{th}\, \sigma\, e^{-(E_t-E_{VB})/k_B T}. \end{aligned} \tag{4.2}$$

The experimental data generally depends on the temperature during both stress and recovery. From Eq. (4.1), we already note that the temperature dependence during electron or hole capture can be explained only by assuming a temperature–dependent cross section σ.

Furthermore, as we already discussed in Section 3.1.2, the SRH model does not explain the complex CET map observed in the case of GaN–based MIS–HEMTs. In fact, in Fig. 3.7b we see states with very small time constants for capture but very long ones for emission, while the SRH model allows only traps with correlated τ_c and τ_e, as shown by the result of a simulation in Fig. 3.7.

We must conclude that this model is inadequate to fully describe charge trapping at the semiconductor/dielectric interface, and therefore we must adopt a different physical model for charge exchange.

4.2 The non–radiative multiphonon (NMP) model

A model capable of describing the physical mechanisms of charge exchange cannot ignore the structural deformation at the defect site. In fact, after an electron (or hole) is captured (or emitted) the microscopic configuration of the defect and the surrounding area changes into a different arrangement. Bond lengths and angles are adjusted in order to accommodate the captured (or missing) charge. In other words, the whole system relaxes towards its new equilibrium position, which is defined by the total potential energy of the system in the respective charge state. The total potential energy is often approximated by a harmonic potential. The equilibrium configuration is therefore defined by a certain equilibrium position q^0 (representing the mass–weighted coordinates of the defect site) and a certain equilibrium energy E^0, corresponding to the minimum of the harmonic potential. This is illustrated in Fig. 4.2.

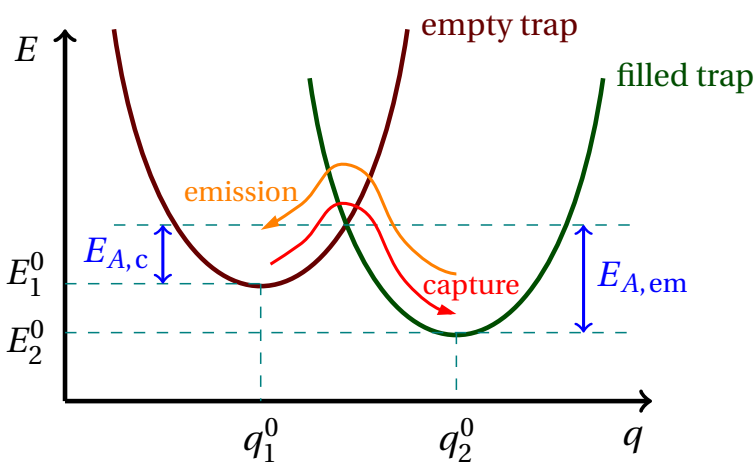

Figure 4.2. The potential energy of a defect site is approximated by a harmonic potential, which takes different equilibrium positions q^0 depending on its charge state. A charge exchange event is therefore a transition between the two potential energy surfaces. In the classical limit, a non–radiative, multiphonon transition must occur through their crossing point, as shown by the arrows.

When a trapping (or detrapping) event takes place, the equilibrium position and the energy of the system change. In this way, the transition from the initial state in q_1^0 to the final state in q_2^0 requires a transition between two potential energy surfaces. Without any external electromagnetic excitation, in a classical, high temperature approximation this can happen only through the crossing point of the two potential energy functions. In this way, an energy barrier is associated with each charge trapping event. The excess energy, called activation energy E_A, is provided to the system as thermal energy through phonon scattering. A *non–radiative multiphonon* (NMP) transition [76–78] is therefore a thermally activated process, which can be described in the classical high–temperature limit by the Arrhenius equation

$$\tau = \tau_0 \, \mathrm{e}^{E_A/k_\mathrm{B}\mathrm{T}}. \tag{4.3}$$

We note the similarity of Eq. (4.3) with Eq. (4.2), if we assume $\tau_0^{-1} = N_\mathrm{C}\, v_\mathrm{th}\, \sigma$ (or $\tau_0^{-1} = N_\mathrm{V}\, v_\mathrm{th}\, \sigma$). The difference is the physical meaning of the energetic barrier: in the SRH picture, it is defined by the energetic position of the trap with respect to the reservoir; for the NMP model it must be determined from the shape and position of the potential energy functions of the initial and final defect configurations.

The temperature dependence of a charge trapping event is given by the Boltzmann factor in the Arrhenius equation, while the applied bias has an influence on the activation energy. In fact, a modification to the gate voltage results in an offset for one of the two potential energy surfaces, thereby changing their relative positions and thus causing a different E_A.

With such a picture of the trapping mechanism we are able to explain very complex charge trapping dynamics, which would not be possible with the model presented in the previous section. For example, the physical model based on NMP transition can explain complex CET maps, allowing a defect to have a short time constant for capture but a long one for emission, because it is possible to find a state with a low barrier energy for capture and a large one for emission processes [79]. In fact, some defects have similar capture and emission time constants and therefore can be charged and discharged continuously within stress and recovery cycles, resulting in a fully recoverable degradation. Other trap sites have emission times much longer than for capture, giving rise to an almost permanent voltage drift, which can eventually recover only after very long time, or with high temperature annealing processes. Furthermore, it was shown that the behavior of threshold voltage drifts of silicon MOSFETs under NBTI can be fully explained only introducing intermediate, metastable defect configurations between the empty trap equilibrium state q_e^0 and the filled trap equilibrium state q_f^0 [80]. These states can be represented in our picture as local minima of the potential energy surfaces, with very similar energy values. The metastable states are also responsible for the anomalous *random telegraph noise* (RTN) observed in such structures [27, 81].

The temperature dependence of Eq. (4.3) can be used for temperature acceleration [82, 83]. Each experimental dataset is conducted at constant temperature (isothermal measurements),

and we expect the trap sites to contribute to the device drift in a different way at different temperatures. However, the time constants τ_1 and τ_2 of the same defect at temperature T_1 and T_2 are related to each other by

$$\tau_2 = \tau_0 \left(\frac{\tau_1}{\tau_0}\right)^{T_1/T_2} \tag{4.4}$$

where τ_0 is the coefficient of the Arrhenius' equation. Eq. (4.4) enables us to bring all measurements at different temperature on the same axis, by introducing the *temperature–time* variable

$$\vartheta(T) = \tau_0 \left(\frac{t}{\tau_0}\right)^{T_{ref}/T}. \tag{4.5}$$

This means that a measurement at cold temperature in the time window between t_0 and t_f is equivalent to a measurement at higher temperature between $t_0' < t_0$ and $t_f' < t_f$. In other words, temperature has the effect of accelerating both stress and recovery mechanisms. This allows us to fix our experimental time window, and investigate shorter time scales by using low temperatures, and longer time scales by increasing it. The shortest accessible time is therefore determined by two factors: the time resolution of the instrument and the coldest temperature achievable in our setup.

In the following, we examine three different scenarios of increasing complexity. The simplest case is to consider τ_0 a constant parameter and E_A to be single–valued (Section 4.2.1). However, this approximation can be too rough to properly explain the experimental data. Therefore, we consider the possibility of a continuous distribution of activation energies in Section 4.2.2, and of a non constant τ_0 in Section 4.2.3.

4.2.1 Constant τ_0, single activation energy

In general, under certain bias conditions, every defect has different parameters τ_0 and E_A. However, in a first approximation we can consider the pre–factor τ_0 to be constant. This has been proven to be accurate enough for NBTI investigations on silicon MOSFETs [83]. Furthermore, we can recognize "families" of states, or defects of the same type, that have approximately the same activation energy. For example, we can group in a "family" all defects that have the same microscopic configuration (due to a certain impurity), or the same origin (due to the vacancy of a certain element). In this way, the charge trapping mechanisms are described by Eq. (4.3) with a constant factor τ_0 and one, or more in case there are more defect "families", single–valued activation energies.

According to the Arrhenius equation, the time response of every single interface state follows an exponential function with characteristic time τ. Each defect type n, with activation energy $E_{A,n}$, gives rise to the time constant τ_n, and contributes to the total voltage shift of the device with the fraction ΔV_n. Summing up over all contributions, and assuming that electrons are being trapped into defects during stress, the threshold voltage shift increases as

$$\Delta V_{th}^{stress}(t) = \sum_n \Delta V_n \, e^{-t/\tau_{c,n}} \tag{4.6}$$

and then, after it reaches a maximum threshold voltage shift of ΔV_{max}, recovers according to

$$\Delta V_{th}^{recovery}(t) = \Delta V_{max} - \sum_n \Delta V_n \, e^{-t/\tau_{e,n}}. \tag{4.7}$$

If the activation energies of the defect types are quite different, it is possible to distinguish each contribution directly by looking at the time evolution of the ΔV_{th} [18]. The various τ_n and the respective $E_{A,n}$ can be easily extracted from a fit to the data. In Section 4.3.1 we present a straightforward method to extract the activation energy from $\Delta V(t)$ data measured at different temperatures.

4.2.2 Constant τ_0, distributed activation energy

Experimental evidence has shown that the single exponential model is normally not sufficient to explain the actual time evolution of ΔV. In fact, we should consider that the interface between two materials, especially in the case of an amorphous dielectric, is characterized by a certain amount of variability in the arrangement of the atoms. For this reason, also the defects exhibit a certain diversity in bond length and angles, thus resulting in a continuous interval of allowed activation energies rather than a precise, single value $E_{A,n}$. For example, we can describe a defect "family" with a gaussian distribution of activation energies around a mean value μ, with a certain standard deviation σ. As a consequence, capture and emission time constant will follow a log-normal distribution and an analytical expression for the device drift can be written as [79]

$$\Delta V_{str}(t) = \frac{\Delta V_{max}}{2} \operatorname{erfc}\left(-\frac{k_B T \ln\left(\frac{\vartheta_{str}(t)}{\tau_0}\right) - \mu}{\sqrt{2}\sigma} \right) \tag{4.8}$$

for stress, and

$$\Delta V_{rec}(t) = \frac{\Delta V_{max}}{2} \operatorname{erfc}\left(\frac{k_B T \ln\left(\frac{\vartheta_{rec}(t)}{\tau_0}\right) - \mu}{\sqrt{2}\sigma} \right) \tag{4.9}$$

for recovery, where ΔV_{max} is the voltage drift at saturation, achieved when all traps have been filled. This approach contributed to great advances in the understanding of the defects present at Si/SiO_2 interfaces and responsible for NBTI: here two main "families" of trap states with gaussian–distributed activation energies have been discovered [27].

However, the problem of determining the relevant defect groups from the experimental data may be complex if we observe a large number of contributions with very close E_A values. This is exactly the case for standard GaN/AlGaN MIS–HEMTs, for which a logarithmic temporal evolution is observed [47, 67]. In fact, a function $y \propto \log(x)$ can be fitted only by a large number of exponential components of the kind $\exp(-x/\tau_n)$. The fit of a dataset constituted by a finite number of points, M, with a multi–exponential model with an unknown number N of exponential components is in fact an *ill–posed* problem [84]. The system in this case is underdetermined: this means that a set of solutions exists, rather than a unique one. A *regularization*

method is therefore necessary in order to find the solution. If no additional information about the system is known, different approaches can be used. For example, the Tikhonov regularization method [84] solves the problem by adding a constraint given by a certain smoothing functional of the solution. The method of maximum entropy (MEM) [85, 86] instead chooses the most noncommital solution, i.e., the one which makes the least assumption on the data, thus fulfilling the parsimony principle by maximizing the Shannon entropy [87]. In our case, we can apply a method that has been developed for the investigation of chemical reactions involving distributed activation energies, which is described in Section 4.3.2.

4.2.3 Non–constant τ_0

In the cases discussed until now, the pre–factor τ_0 is assumed to be constant, to be determined as a parameter of the fit to the whole dataset of measurements taken at different temperatures. However, in certain cases this approximation can be too crude and might lead to an error in the determination of the activation energy values.

The physical meaning of τ_0 for a single charge transfer reaction following Eq. (4.3) can be related to the phonon frequency, i.e., how many phonons per unit time are available to provide energy to overcome the energetic barrier. In fact, the fitted value of τ_0 from investigations on silicon MOSFETs agrees with the inverse of the phonon frequency in silicon, which has been measured and can be estimated with DFT calculations to be on the order of 10^{13} Hz [83].

The first reason for the failure of the constant τ_0 approximation can be a large variety of defect types. In fact, each type would have a characteristic $\tau_{0,n}$ for its charge exchange reaction, related to the attempt frequency in that particular case. Such $\tau_{0,n}$ is already an approximated value, averaged over the entire "family" of similar defects, each of which has its own characteristic τ_0. The overall effect on a macroscopic device, however, has a characteristic time constant given by the average over the $\tau_{0,n}$ of all the active defects in those conditions. As a consequence, if measurements at different temperatures access different defect types, it is clear that a single τ_0 cannot be found. For example, this can happen if some traps have a quite large time constant, becoming active only at high temperatures, but are not accessible at low temperatures. The whole dataset from low to high temperatures in this case cannot be fitted accurately with the same τ_0. An experimental approach that allows to avoid this problem is the *time–dependent defect spectroscopy* (TDDS), developed and used for NBTI studies on Si/SiO_2 MOSFETs. It relies on the measurement of small–area devices, thus allowing to deal with only a handful of defects at a time [80, 88, 89] and therefore to determine the properties of each trap state individually.

A second reason for a non–constant τ_0 can be found in the inaccuracies arising from the classical approximation. In fact, Eq. (4.3) is based on the assumption that a transition between two potential energy functions occurs at the intersection point (IP), as illustrated in Fig. 4.3a. The IP determines the height of the barrier, that is the activation energy E_A. However, the quantum–mechanical approach to the same problem possibly leads to a lower value for the

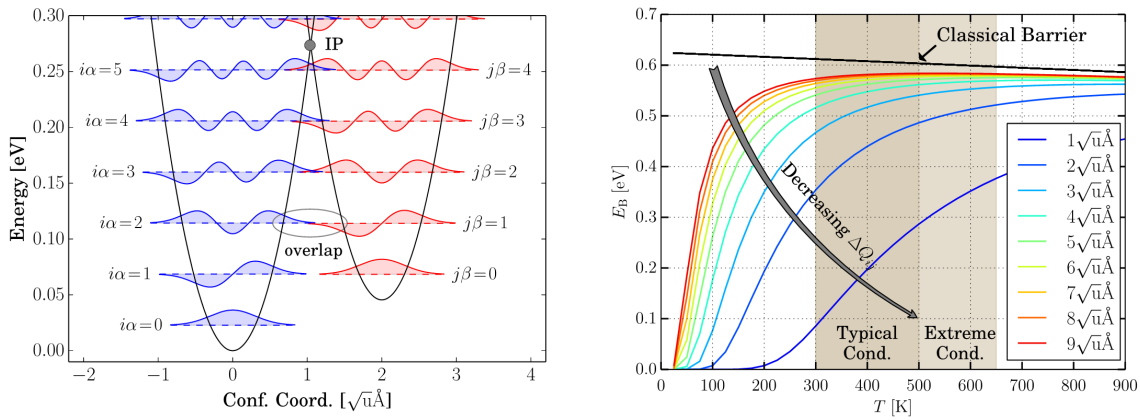

(a) (b)

Figure 4.3. The transition between two potential energy surfaces occurs at the intersection point (IP) in the classical approximation, but in the quantum–mechanical approach tunnelling between two wavefunctions can take place as well (a). The resulting activation energy can be much lower than the classical value (b), depending on temperature and the displacement ΔQ between the two equilibrium coordinates (from [90]).

energy barrier and a different τ_0. The solutions of a harmonic potential are wavefunctions characterized by a discrete energy spectrum, as shown in Fig. 4.3a. Depending on the distance of the two equilibrium positions q_1^0 and q_2^0, it can happen that some excited states of the two harmonic potentials overlap at an energy below that of the IP. This gives a certain probability for the transition at a lower energy barrier than the classical one through carrier tunnelling. In Fig. 4.3b the activation energy in the classical limit and with the quantum–mechanical approach have been calculated as a function of temperature and for different values of displacement $\Delta Q = q_2^0 - q_1^0$ [90], performing density functional theory (DFT) calculations based on the data obtained by TDDS studies on silicon MOSFETs. The error on E_A due to tunnelling is larger at cold temperatures, and it can be still relevant under typical conditions of device operation (down to 300 K). Unfortunately, at the present time it is not yet possible to perform the same calculations for GaN/AlGaN MIS–HEMTs, since the properties of the defects needed for DFT simulations are still unknown. Further investigations and the improvement of the characterization methods are therefore necessary to clarify this aspect.

In conclusion, if the wavefunction overlap is not negligible, the extraction of E_A and τ_0 with Eq. (4.3) results in non–constant, temperature–dependent values: at higher temperature the energy would increase while τ_0 would decrease. We discuss further the possible effects of a non–constant τ_0 in Section 4.3.3.

4.3 Extraction of the activation energy and τ_0 from experimental data

In this section we introduce two data analysis methods that assume a constant τ_0, dedicated to the extraction of single–valued and distributed activation energies. We test the methods on three datasets, simulated using Eq. (4.3) and Eq. (4.6). We reproduce the ΔV transients during stress in the case of a single–valued E_A of 0.3 eV (labeled "single–state"), the case of two trap states with energies 0.2 eV and 0.4 eV ("multi–state"), and a normal distribution of activation energies with mean μ =0.3 eV and standard deviation σ = 0.1 eV ("distributed"), from 10 µs to 100 s. We choose a pre–factor τ_0 = 50 ns and various temperatures between –100 °C and 100 °C. The transients obtained in this way are shown in Fig. 4.4.

Furthermore, we discuss the effect of a non–constant τ_0 on the data. The methods described here are applied in Chapter 5 to our experimental data.

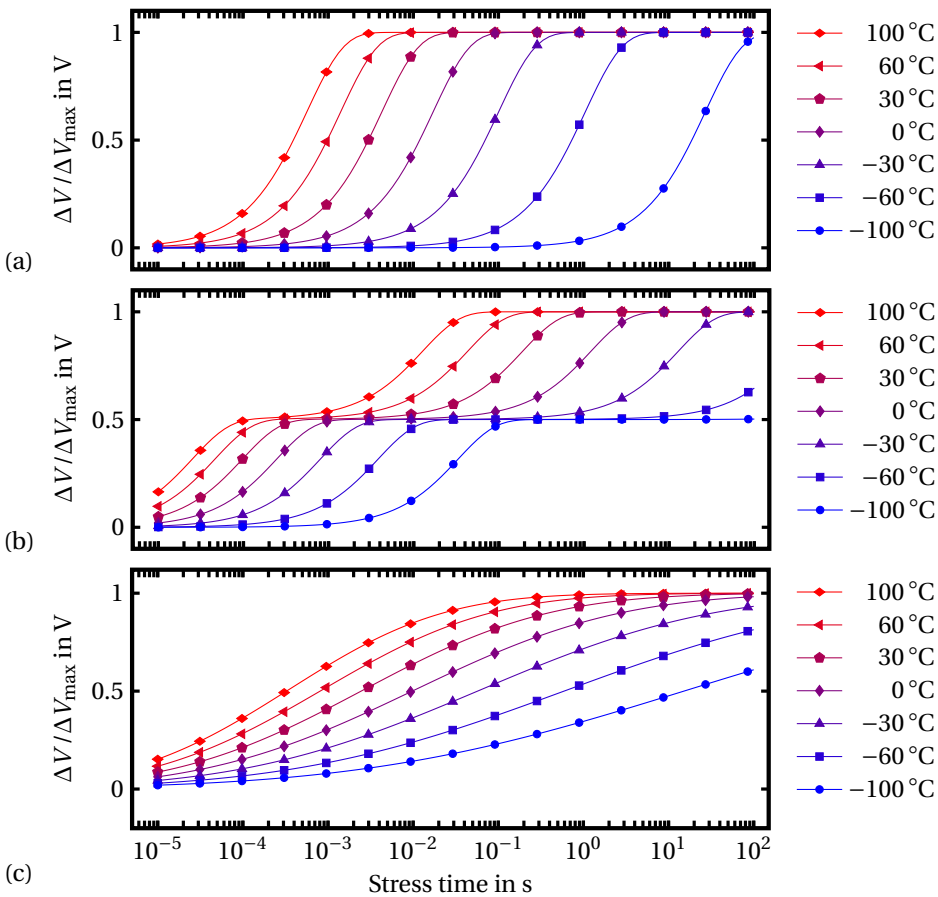

Figure 4.4. Simulated ΔV transients with τ_0 = 50 ns at temperatures from –100 °C to 100 °C over seven decades. We assume a single–valued E_A of 0.3 eV (a), two defect states with single–valued E_A of 0.2 eV and 0.4 eV (b), and a normal distribution of activation energies with mean μ = 0.3 eV and standard deviation σ = 0.1 eV (c).

4.3.1 Extracting single–valued activation energies

We present here a direct, simple way to evaluate the activation energy from a set of recovery transients at different temperatures, based on the Arrhenius equation. We choose few values of voltage shift, V_{extr}, included in the range of our dataset. In our example, we take nine values between 0 V and 1 V. For each recovery transient we extract the time t^* at the extraction voltage V_{extr}. In this way we obtain a set of t^* as a function of temperature and V_{extr}. For each extraction voltage we perform a linear fit of $\log(t^*)$ as a function of $1/k_B T$, the Arrhenius plot, which is shown in Fig. 4.5. According to Eq. (4.3), the slope of the fitting line is the activation energy E_A and the offset gives the pre–factor τ_0. Finally, an average over the results at various V_{extr} gives an estimate for E_A and τ_0 [54].

Next, we test the Arrhenius analysis of the simulated data. The results are shown in Fig. 4.6 for various values of V_{extr}. We note that this method provides an accurate energy value for all V_{extr} values when the distribution is single–valued. Also for two single–valued states (or multi–state), it is possible to distinguish two regions where the two distinct activation energies are correctly estimated. On the contrary, if E_A is broadly distributed the results at various V_{extr} can be very different. In this case, the smallest and largest V_{extr} give an error in the activation energy of about 30%. Nevertheless, we note that the extracted activation energy E_A as a function of V_{extr} is symmetric around its mean value, in our example 0.3 eV. Therefore the average over all extraction voltages gives the correct mean activation energy μ. Visually, we can determine the mean E_A value as the symmetry axis in Fig. 4.6a. Unfortunately, this is rarely possible with real data. In the first place, noise might conceal this feature. Another reason is that the measurement window should be large enough to reveal the whole shape like in Fig. 4.6a, which is impossible to know a priori. Therefore, this method might give just a rough estimate of the real E_A value. Regarding the pre–factor τ_0, the error in this case is larger than for the activation

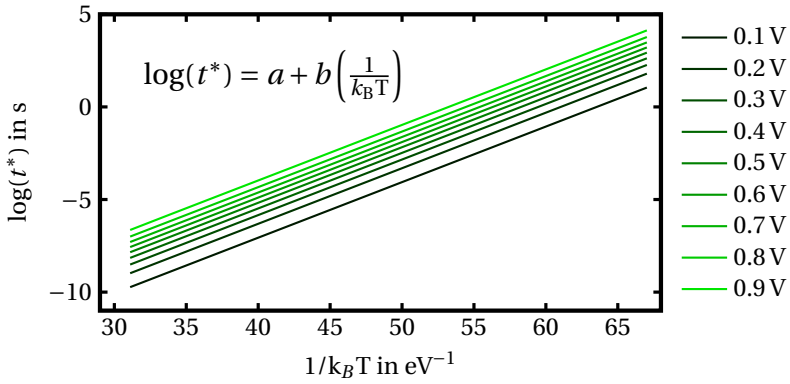

Figure 4.5. Arrhenius plot for the single–valued dataset, for nine values of V_{extr} between 0.1 V and 0.9 V. A linear fit to these plots provides an estimate of the activation energy as the slope, b, and of τ_0 as the exponential function of the offset, a.

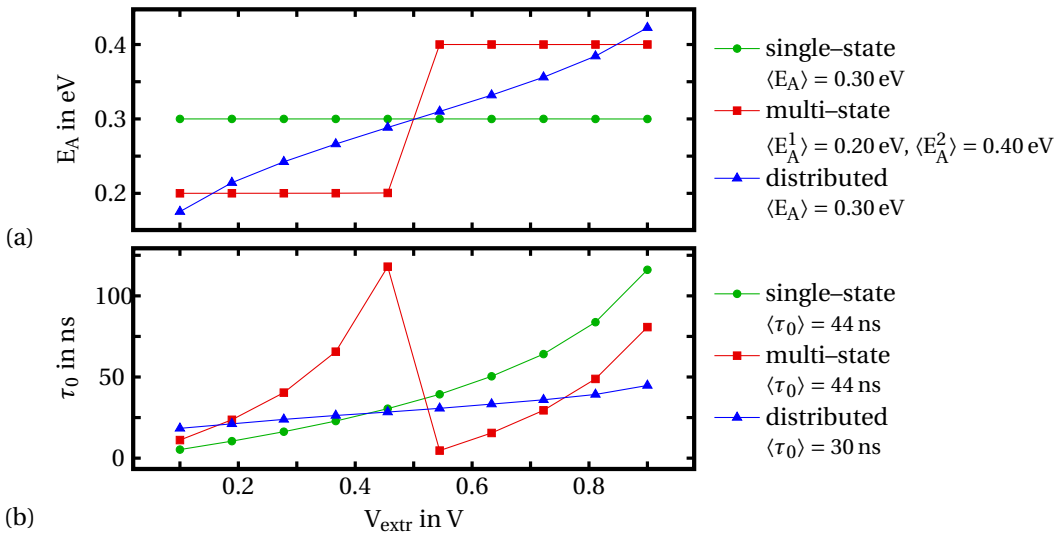

Figure 4.6. Activation energy (a) and pre–factor τ_0 (b) extracted from the simulated data. The original values are a single–valued $E_A = 0.3$ eV, a multi–state defect with $E_A^1 = 0.2$ eV and $E_A^2 = 0.4$ eV, and a normal distribution of energies with mean 0.3 eV and standard deviation 0.1 eV. We use a constant τ_0 of 50 ns. The average over V_{extr} for E_A and τ_0 are shown in the legend.

energy. In fact, the fitted values have the correct order of magnitude but they can be 35% off the original τ_0.

In conclusion, this method provides an estimate of the mean value of the activation energy, but it does not give any insight into the actual range of its distribution. Therefore, this analysis is sufficient if the activation energy has a precise, single value, but it offers only partial information if E_A is distributed across a broader range, which is the most common situation for interface defects.

4.3.2 Extracting distributed activation energies

We present here a method to extract the distribution of activation energies associated with trapping events, which is based on the study of chemical reaction kinetics, proposed by Primak in 1955 [91]. In fact, the charge exchange event responsible for the device drift causes the modification of certain chemical bonds at the AlGaN/SiN interface. We can therefore think of the capture process as a chemical reaction which transforms a reactant, the empty trap, into a product, the filled trap state. This approach can be described mathematically with a differential equation. Indicating the reactant concentration as a quantity depending on the activation energy, $g(t, E_A)$, its time evolution is given by the differential equation

$$-\frac{\mathrm{d}g}{\mathrm{d}t} = k\,g \tag{4.10}$$

where we assume for simplicity first–order kinetics, with $k = 1/\tau$ as its temperature–activated rate constant, obeying Eq. (4.3). The solution of the differential equation is

$$g(t, E_A) = g(t = 0) \exp\left[-\frac{t}{\tau_0}\exp\left(-\frac{E_A}{k_\mathrm{B}\mathrm{T}}\right)\right] \tag{4.11}$$

which can be written as

$$g(t, E_A) = g(t = 0, E_A)\,\Theta(t, E_A) \tag{4.12}$$

where the function $\Theta(t, E_A)$ is called the characteristic isothermal annealing function. It is a monotonically increasing function of the activation energy, with a rising transient around the characteristic activation energy

$$E_A^0 = k_\mathrm{B}\mathrm{T}\ln\left(\frac{t}{\tau_0}\right). \tag{4.13}$$

The width of the rising transient is directly proportional to τ_0 [91]. Since τ_0 is usually small, the characteristic isothermal annealing function can be approximated with a step function in E_A^0 with a small error [92].

Furthermore, if we integrate the reactant concentration $g(t, E_A)$ over energy, we obtain the density of active defects, $\Delta\mathrm{N}_\mathrm{it}$:

$$\Delta\mathrm{N}_\mathrm{it} = \int_0^\infty g(t, E_A)\mathrm{d}E. \tag{4.14}$$

In addition, $g(t = 0, E_A)$ is actually the spectral density of defects that play a role in this reaction. We call the spectral density $D_\mathrm{it}(E_A)$, which is the distribution in energy of E_A. As a consequence, we can calculate $D_\mathrm{it}(E_A)$ from the experimentally observed ΔV using Eq. (1.1) and

$$D_\mathrm{it}\left(k_\mathrm{B}\mathrm{T}\ln\left(k_0 t\right)\right) = -\frac{t}{k_\mathrm{B}\mathrm{T}}\frac{\mathrm{d}\Delta N_\mathrm{it}}{\mathrm{d}t} \tag{4.15}$$

where k_0 is the inverse of the coefficient τ_0.

This method therefore extracts the activation energy spectrum of the defect concentration. However, because of the approximation of $\Theta(t, E_A)$ by a step function, the result will be a smooth function of the activation energy. For this reason this technique is not sensitive to sharp features in the spectrum.

The pre–factor τ_0 can be extracted by a fit to the data taken at different temperatures. Since we have the same temporal window for all measurements, we can calculate the defect density within an energy range determined by temperature through Eq. (4.13). The higher the temperature, the larger the E_A values which are experimentally accessible. The optimal τ_0 is the value which gives a smooth spectrum when connecting the parts at different temperature. We use a numerical algorithm in order to optimize τ_0 according to this approach.

We begin the evaluation of the Primak method using the simulated dataset. The results are shown in Fig. 4.7 for the three cases introduced in Fig. 4.4. The mean value of the activation energy is always extracted accurately: 0.3 eV for the single–state and distributed cases, and for the multi–state we can see two distinct peaks at 0.2 eV and 0.4 eV. The optimized value for τ_0 is compatible with the original 50 ns within an error of 30%.

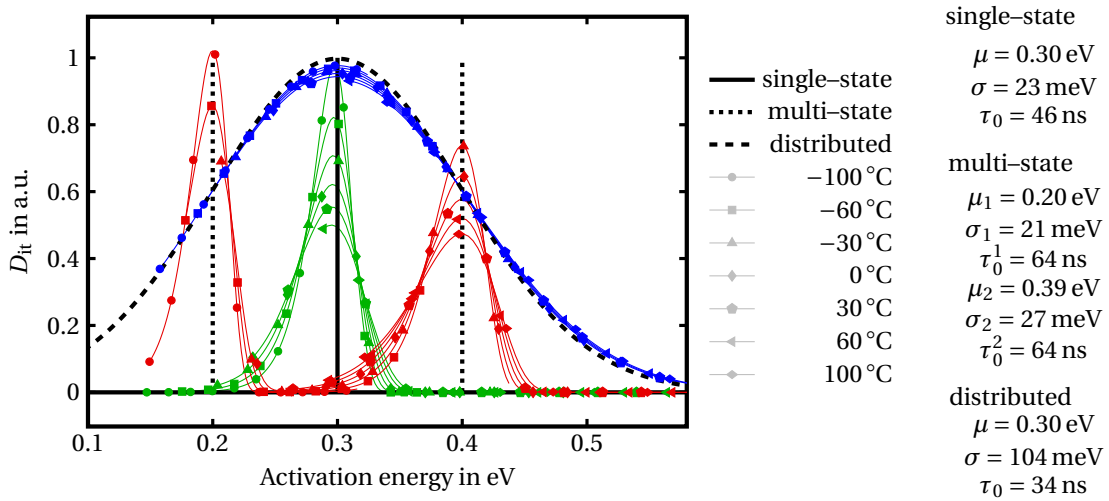

Figure 4.7. Activation energy distribution extracted from the simulated transients at various temperatures. The D_{it} values are scaled for better reading. The lines show the original activation energy functions: the single–valued 0.3 eV (solid), the two single–valued 0.2 eV and 0.4 eV (dotted) and the normal distribution with mean 0.3 eV and standard deviation 0.1 eV (dashed).

A limitation of this method is the apparent standard deviation, which is different from zero even for the dataset simulated with a single–valued E_A trap states. In this case σ_{apparent} is around 25 meV. This is an artifact of the analysis caused by the assumption on the characteristic isothermal annealing function. We can consider σ_{apparent} to be the energy resolution of the Primak method.

4.3.3 Effects of a non–constant τ_0

As we discussed in Section 4.2.3, a broad distribution of trap types and the failure of the classical limit are two factors that can determine a non–constant τ_0 over a set of data taken at different temperatures. Having a more detailed look at the reaction kinetics, we find that in both cases the differential equation Eq. (4.10) is no longer sufficient anymore to describe our system. Such equation means that the empty traps, with concentration g, are trapping electrons with a rate k. Thus, they become filled traps, which have a concentration g'.

However, if at a certain temperature an additional defect "family", p, becomes active, we do not have only the reaction from g to g', but also that of p to p' with a different rate constant k'. The two phenomena may even be competitive, because the electrons can be trapped in either one or the other trap type. If the reaction is not limited by electron supply or other external factors, the observed time constant for electron capture is the average value between $1/k$ and $1/k'$. For example, if the defect type p becomes active at high temperature, its time constant would be probably longer than that for g. In this way, we would obtain an increase of the effective τ_0 as a function of temperature.

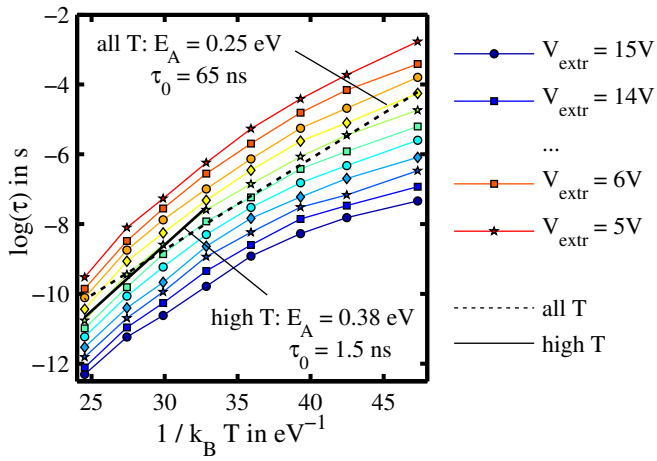

Figure 4.8. Example of non linear Arrhenius plot from the measurements on the MIS–HEMT devices with the fluorinated interface. The linear fits with all or just the highest temperatures are shown as dotted and solid black lines, respectively.

On the other hand, if the reaction does not only happen through the classical intersection point (giving rise to the rate constant k), but also with tunnelling, we have an alternative way for the same reaction, with a different rate constant k''. In this case, the energetic barrier height is lower than the classical one, and this effect is stronger the lower the temperature (see Fig. 4.3). As a consequence, the analysis of the data using Eq. (4.3) as explained in Section 4.3.1 would result in a temperature dependent activation energy, which means a temperature dependent slope in the Arrhenius plot. This might be a possible explanation for Fig. 4.8, which has been calculated for the MIS–HEMTs with fluorinated interface. The convex curvature of the lines at low temperature indicates that there is a deviation from the classical Arrhenius interpretation [93]. We extract E_A as the slope of a linear fit, by using the whole curve or just the four highest values of temperature. As we would expect from Fig. 4.3b, the activation energy at high temperature is larger. Although many other explanations are possible, charge exchange through tunnelling could be the reason of the non–linearity of the Arrhenius plot of these structures.

We can add a third phenomenon that would result in a non–constant τ_0. At a certain temperature it might become possible that the population g transforms into a third state, g'', having another, different rate constant k''' and a higher activation energy than that of the main reaction. Let's assume that the reaction from g'' to g' is not possible, or that it has an extremely large barrier. If we can measure only the change from g to g' but we are insensitive to g'', then we would observe less reactions than we would expect, as some reactant are "blocked" in the third state. As a consequence, since the amount of g to g'' events depends on temperature, also the observed reaction becomes temperature dependent, which will result in the observed curvature of the Arrhenius plot. This is often observed in biology studies, when a certain biological

system (e.g., a protein) reacts with the system and transforms into something else; however, at high temperature it can undergo a denaturation process which blocks the reaction. In this case, the Arrhenius plot $\log(t)$ as a function of $1/k_{\mathrm{B}}\mathrm{T}$ usually has a convex shape [94].

In conclusion, a non–constant τ_0 could be due to different reasons [95]. More detailed experiments are necessary in order to identify the true origin. The effect on the experimental data is clearly visible as the non–linearity of the Arrhenius plot. It should also be observed when we try to connect the data at different temperature with the Primak method: if τ_0 is temperature dependent, then we would not find a single value which gives a smooth spectrum. However, this effect can be small because of the noise caused by the derivation of the data.

5

Electrical characterization of interface defects in GaN–based MIS–HEMTs

IN THIS CHAPTER we apply the experimental methods discussed in Chapter 3 and the physical model presented in Chapter 4 to our test structures. In the first place, we compare the MSM and the C–OTF experimental approaches and we discuss their outcomes on different samples. Then, we evaluate the impact of forward gate bias stress on device degradation due to the defects at the AlGaN/dielectric interface, and we extract the trap density. We use different GaN–based test structures: MIS and MIS–HEMTS with and without the barrier layer, with different bulk compositions and with different AlGaN surface chemical treatment. We characterize and compare them in order to understand the behavior of the interface traps and the impact of certain processes during production.

5.1 Results on devices with standard interface

In this first section we focus on structures with a standard AlGaN/dielectric interface. Such devices have been extensively investigated [47, 51] and they always display a linear dependence of the threshold voltage shift on the logarithm of time under positive gate bias stress, from 100 ns to 10 ks. This implies a broad distribution of characteristic time constants of the interface traps, irrespective of variations of the Al content from 20% to 25%, of the thickness of the barrier (10 nm to 25 nm), that of the dielectric (25 nm to 75 nm) and the dielectric material (SiN, SiO_2, AlO, HfO_2, $HfSiO_2$). As a preliminary step, we apply and compare the two experimental methods introduced in Chapter 3.3. Then, we evaluate their response to positive gate bias stress and we calculate the density of traps present at the interface with the Primak approach, as described in Chapter 4.3.2.

5.1.1 Comparison of experimental methods

We apply the MSM and the C–OTF methods on two different GaN/AlGaN MIS structures. The first has a 25 nm thick barrier and a UID GaN buffer; the second has a 50 nm thick AlGaN layer, its area is roughly four times larger and an additional silicon doped (10^{18} cm^{-3}) layer is inserted into the GaN, 100 nm from the interface with AlGaN.

Fig. 5.1 shows the impedance characteristics of the two test structures. In both cases we clearly observe a frequency dispersion, arising from the dynamic response of the AlGaN barrier to the applied small–signal excitation, as discussed in detail in Section 3.2.1. The best estimate for the spill–over voltage is given by the quasi–static CV: the Si–doped sample has a V_{so} of –4 V, the UID structure of –1 V.

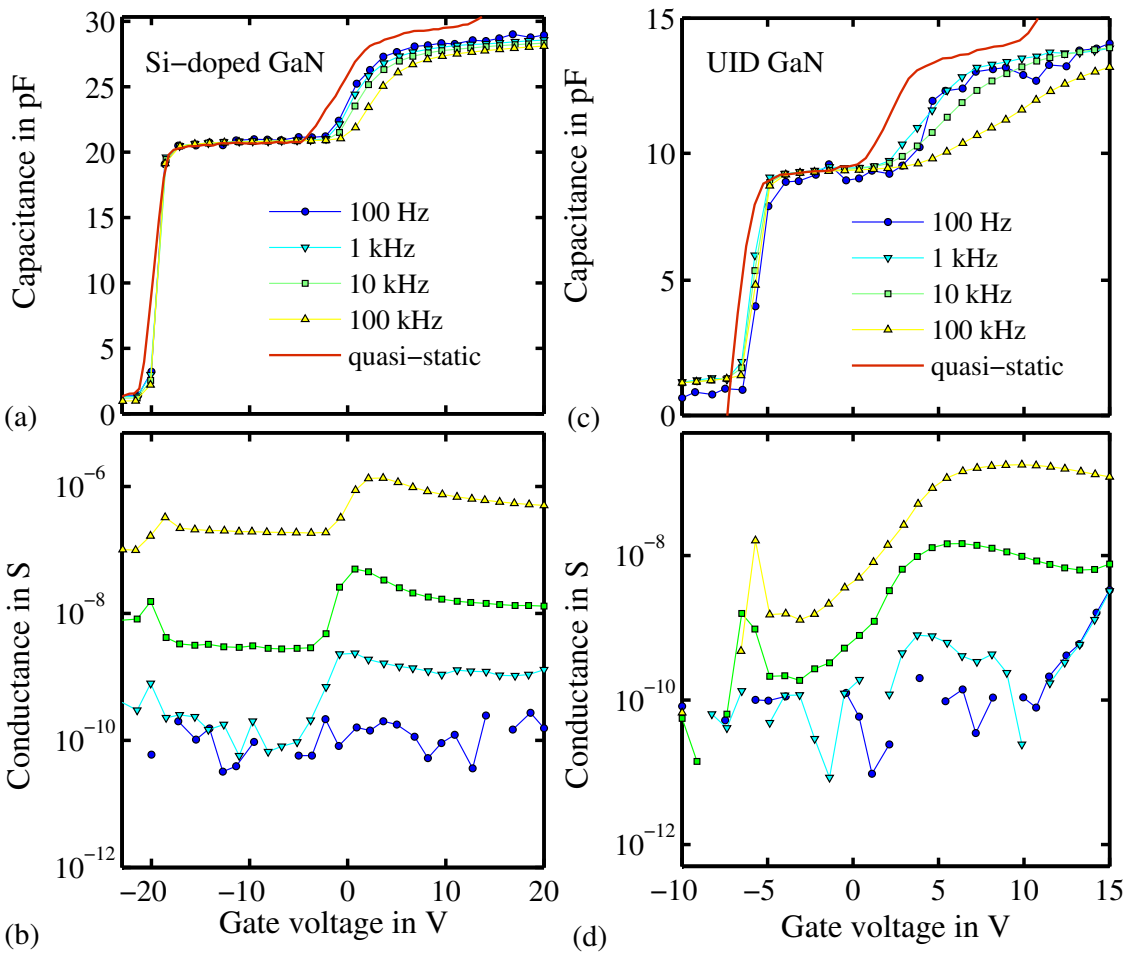

Figure 5.1. Impedance characteristics of the devices with the Si–doped layer: capacitance (a) and conductance (b) at various frequencies, and the same measurements on the structures with the UID GaN buffer (c and d). The quasi–static CV is also shown. All data has been measured with the impedance analyzer using the same parameters (from [67]).

We apply a positive bias at the gate contact in order to bring the devices in spill–over conditions, and then we monitor the voltage drift. We use similar operating conditions for the two structures by choosing a voltage 9 V larger than V_{so} [51]: the resulting stress voltage used in this experiment is $V_{stress} = 5$ V for the Si–doped and $V_{stress} = 8$ V for the UID devices.

The MSM method is based on the comparison of the capacitance before and after stress. In particular, we measure in the proximity of the first steep capacitance step, where the sensitivity to ΔV is very high. Unfortunately, the read–out voltage must be negative, thus bringing the device into recovery conditions. The interval of time between the voltage switch and the measurement of the first experimental point causes a partial recovery from the applied stress. As a consequence, we systematically underestimate the real degradation by an amount ΔV_0^{MSM}. In addition, at such gate bias buffer defects may have an impact as well.

On the other hand, with the C–OTF method we make two approximations which result in a systematic overestimation of the voltage shift. First, we neglect the additional stress caused by the sweep when measuring the capacitance characteristic, and secondly, we assume a parallel shift of the CV curve during stress. In addition, we miss a certain ΔV_0^{OTF} because of the unavoidable measurement delay.

The method which gives the most severe error depends on the relative time dependence of capture and emission processes. In fact, using the same time delay, ΔV_0^{MSM} depends on the amount of electrons that can be emitted during this interval, while ΔV_0^{OTF} depends on the capture process at the beginning of the stress transient. Recent studies on standard devices with UID GaN buffer have shown a similar temporal evolution of stress and recovery [52]. In this case, we would expect that the errors with the two methods are on the same order of magnitude. In fact, the results in Fig. 5.2a confirm our hypothesis.

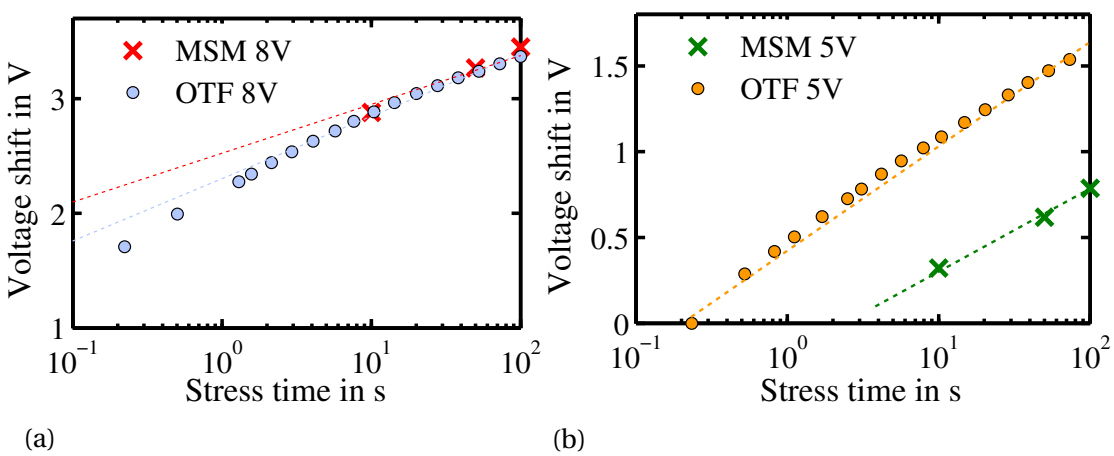

Figure 5.2. The temporal evolution of the voltage shift during stress, measured with MSM and C–OTF methods for the devices with UID GaN buffer (a) and with the additional Si–doping (b). The dashed lines show a logarithmic fit to the data (from [67]).

Interestingly, this is not the case for the Si–doped devices. As we can see from Fig. 5.2b, the MSM method severely underestimated the ΔV in comparison to the C–OTF. The difference is about 40%. We explain this effect with the presence of additional defects in the bulk, located in the Si–doped region, which become active when the negative read–out bias for the MSM technique is applied. In this way, the negative shift due to the buffer defects results in a strong underestimation of the positive ΔV accumulated during stress.

In conclusion, the two methods give similar results for the structures with an UID GaN bulk. The C–OTF technique focuses on the stress transient, giving directly the temporal evolution of ΔV with a single measurement, while the MSM approach can be used for more complex experiments of repetitive stress and recovery cycles. The presence of a highly doped layer inside the GaN buffer can result in a severe error when the MSM method is used, because buffer defects cause additional trapping phenomena at negative bias. On the contrary, the data extracted with the C–OTF method is unaffected by those traps, and in this case is the most accurate characterization method.

5.1.2 Effect of forward gate bias stress

We further investigate the devices with the silicon–doped buffer using the C–OTF method. We focus on the dependence of the voltage shift on time, bias and temperature.

The results for different stress voltages at room temperature (30 °C) are summarized in Fig. 5.3. As expected, we observe a logarithmic behavior over time. We estimate the density of electrically active interface states at the interface to be on the order of 10^{13} cm^{-2}.

Fig. 5.4a shows the bias dependence of the voltage shift between 220 ms and 100 s of stress. We see that an increase of gate bias stress leads to a larger final device drift. This can be ex-

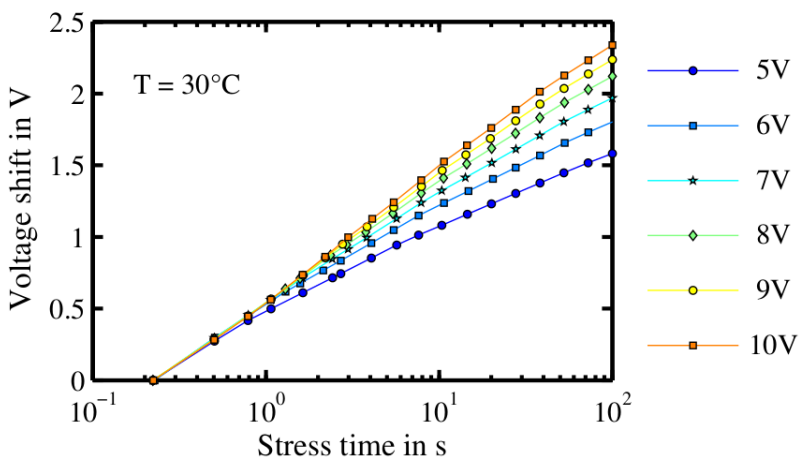

Figure 5.3. Results on the standard GaN/AlGaN/SiN test structures with the C–OTF method at room temperature (30 °C), for various values of forward gate bias $V_{\text{stress}} > V_{\text{spill-over}}$. The first measured point is at 220 ms (from [67]).

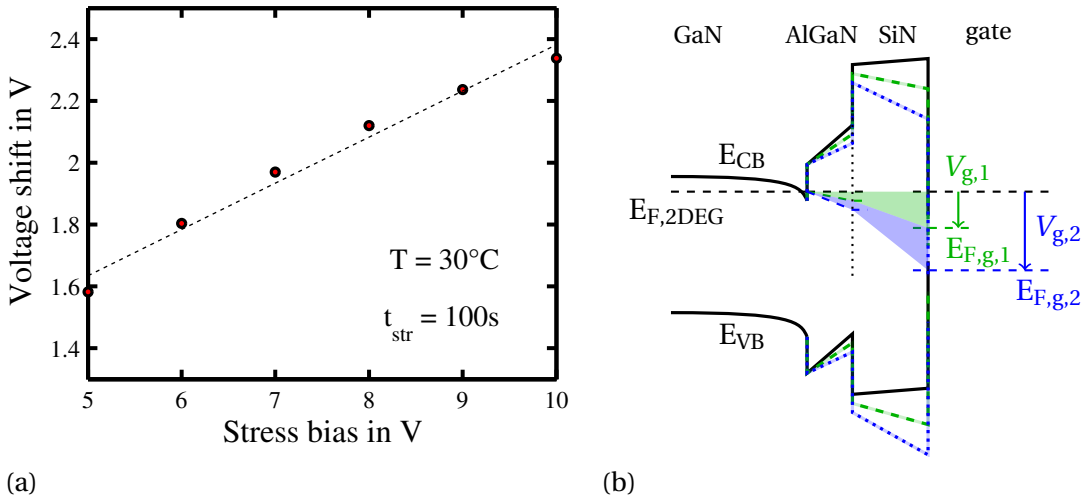

Figure 5.4. Dependence of the ΔV value on the gate bias (a) between 220 ms and 100 s at room temperature (30 °C), from Fig. 5.3. The line is a guide to the eye. Schematic illustration of the AER concept (b). The band diagram is shown in three situations: before stress (solid line), after stress at $V_{str} = V_{g,1}$ (dashed) and after stress at $V_{str} = V_{g,2} > V_{g,1}$ (dotted).

plained by considering the amount of trap states which are in a favorable position in energy to change their charge state as a function of V_{stress}. When the external positive bias is applied the band structure changes, lowering the conduction band edge. In this way, an additional number of defects are brought from above to below the Fermi level, thus acting as electron traps. This is sketched in Fig. 5.4b. The portion of accessible states is called the *active energy region* (AER) [27], and it increases with gate bias stress.

We investigate the influence of temperature by performing C–OTF experiments using a cryogenic probe station. In this way, we span a range of nearly 400 °C, from liquid nitrogen temperature (–190 °C) to the highest chuck temperature (200 °C). We apply a stress bias of 5 V for 100 s. From the coldest to the hottest conditions we always observed a logarithmic behavior over time, as shown in Fig. 5.5a. The only difference with increasing temperature is an increase of the slope of ΔV.

We can compare the effect of positive stress on composite GaN/AlGaN MIS devices and similar structures that do not have an AlGaN layer. Obviously, the GaN/SiN samples do not have any 2DEG, but in this case the carriers are supplied by the Si–doped layer buried in the GaN. For this reason they exhibit poor conductive properties, which explains the larger noise in the data with respect to the composite GaN/AlGaN measurements, as we can see in Fig. 5.5b. Nevertheless, we observe a qualitatively similar behavior to the previous case: ΔV increases linearly with the logarithm of time and higher temperatures lead to a faster degradation. This result allows us to exclude that the transport through the barrier is the rate limiting effect. This is consistent with previous experiments which have investigated the role of the barrier in MIS–

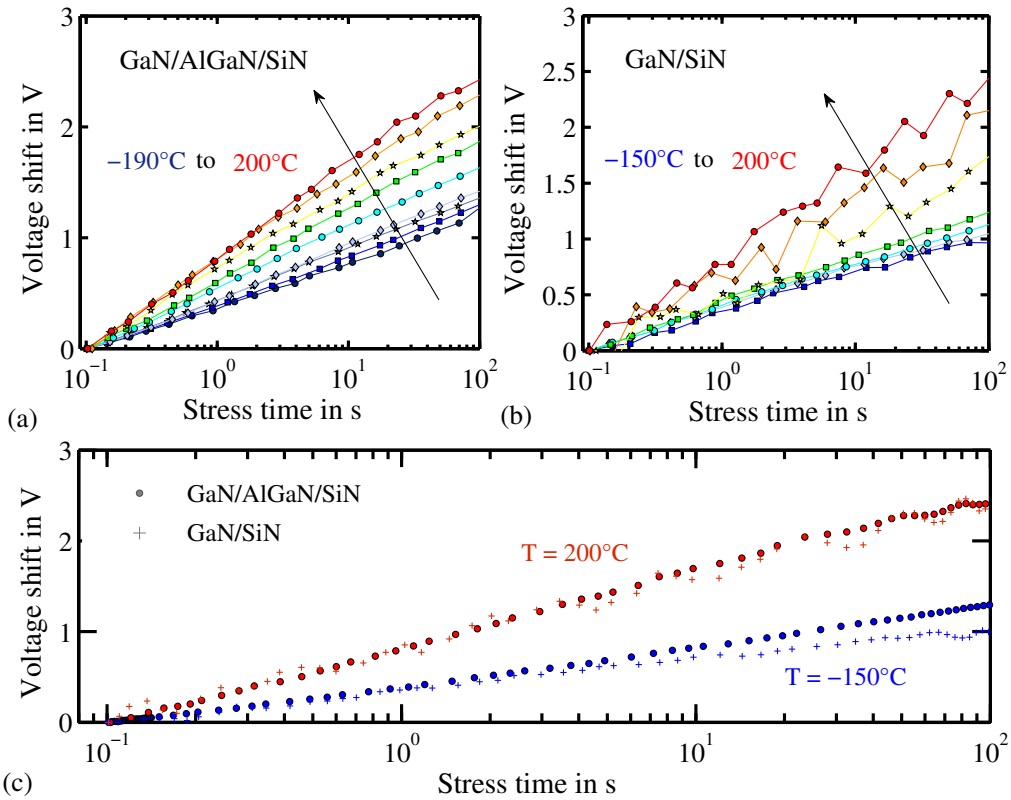

Figure 5.5. Isothermal forward gate bias stress experiments from cryogenic (–190°C) to high (200°C) temperature, for the GaN/AlGaN/SiN (a) and the GaN/SiN devices (b). Interestingly, the temporal behavior of the degradation does not change much over a range of almost 400°C. Comparison of the coldest and hottest stress experiment for the devices with and without an AlGaN layer (c): the similarity of the temporal evolution of ΔV implies the same qualitative degradation mechanism.

HEMT degradation. It has been shown that the barrier becomes important for short stress times at low biases, while for long times and gate bias well above spill-over (like in our experiment) this is not the case [47]. Fig. 5.5c summarizes and makes a direct comparison of the two wafers with the standard interface at the coldest and highest temperature. Except for the noise, the difference in absolute value of ΔV between the two cases is of about 10%.

5.1.3 Evaluation of the interface trap density

We apply the Primak method for the extraction of the density of interface traps, D_{it}, from the experimental data on the GaN/AlGaN/SiN devices. The result is shown in Fig. 5.6.

The energy range accessible with our measurements is from 0.1 eV to 0.8 eV. The trap density spectra are distributed over the whole interval, never falling below 5×10^{12} cm^{-2} eV^{-1}. The small increase of D_{it} to 2×10^{13} cm^{-2} eV^{-1} at low energies could be a hint to a normal distribu-

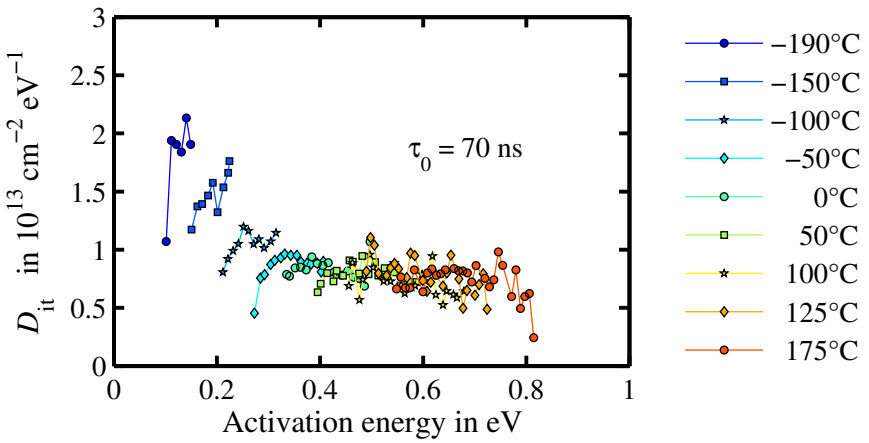

Figure 5.6. The density of interface traps per unit energy D_{it} over activation energy for the standard AlGaN/SiN samples is distributed over the whole accessible energy range, from 0.1 eV to 0.8 eV (from [96]).

tion around a value below 0.1 eV. However, with our experimental setup we are sensitive only to this portion of the spectrum. Measurements at colder temperatures or the evaluation of the device drift on shorter time scales would allow to extend the energy range to smaller values. The almost uniform distribution of activation energies from 0.2 eV to 0.8 eV gives rise to the observed uniformly distributed time constants, which in turn cause the logarithmic behavior of the ΔV over time.

We can interpret this result as a clear indication of the disordered nature of the AlGaN/SiN interface. Physical–chemical investigations in fact suggest the presence of a non–stoichiometric interlayer, about 1 nm thick, where the density of point defects is very high. Although the origin of such defects is still under investigation, recent studies indicate the accumulation of oxygen impurities at the bottom of the SiN layer, which is in contact with the AlGaN [97].

The question whether these states are actually the surface donor states necessary for the 2DEG formation remains open. However, the comparison with the devices with the fluorinated AlGaN/SiN interface presented in the next Section leads to some interesting conclusions.

5.2 Results on devices with fluorinated interfaces

The fluorination of the AlGaN surface before the deposition of the dielectric results in particular device properties, which are observed only when this cleaning process is used. The differences to the standard devices indicate that fluorine plays an active role in passivating the native surface donor states, while it gives rise to an additional type of defect. In this section we describe the characteristics of the fluorinated GaN/AlGaN MIS–HEMTs, investigating their behavior under forward and reverse gate bias conditions. Finally, we evaluate the density of interface traps and compare it with that of standard devices.

5.2.1 Effect of fluorination on device behavior

The fluorination process at the AlGaN/SiN interface results in a slightly reduced 2DEG density of the MIS–HEMT devices, namely 5.5×10^{12} cm^{-2} instead of 7.3×10^{12} cm^{-2} [54], but, on the other hand, threshold voltage drifts appear to be consistently reduced and the hysteresis is almost absent, as we can see in Fig. 5.7. Furthermore, there is no increase of capacitance at positive gate bias. The capacitance takes the value of the plateau, $(C_{AlGaN}{}^{-1} + C_{diel}^{-1})^{-1}$, until breakdown of the device around 20 V.

We can explain the absence of the spill–over capacitance by studying the trapping behavior. Electron capture can be measured with our setup only around the threshold voltage, i.e., when the gate bias is switched from a value in depletion to one above V_{th}. When a more positive bias is applied, transients are stable down to microseconds [54]. This means that our experimental setup is too slow to appreciate electron trapping, which takes place entirely before we can measure the first point. For this reason, the devices appear to be always in equilibrium conditions. If we could measure the CV curve at the time scale of electron capture, we would indeed observe the second rise of capacitance in spill–over conditions. However, the electrons are promptly trapped at interface states and therefore the capacitance returns again to the plateau value. Since the trapping phenomena cannot be investigated with our time resolution, we focus on the electron emission process instead.

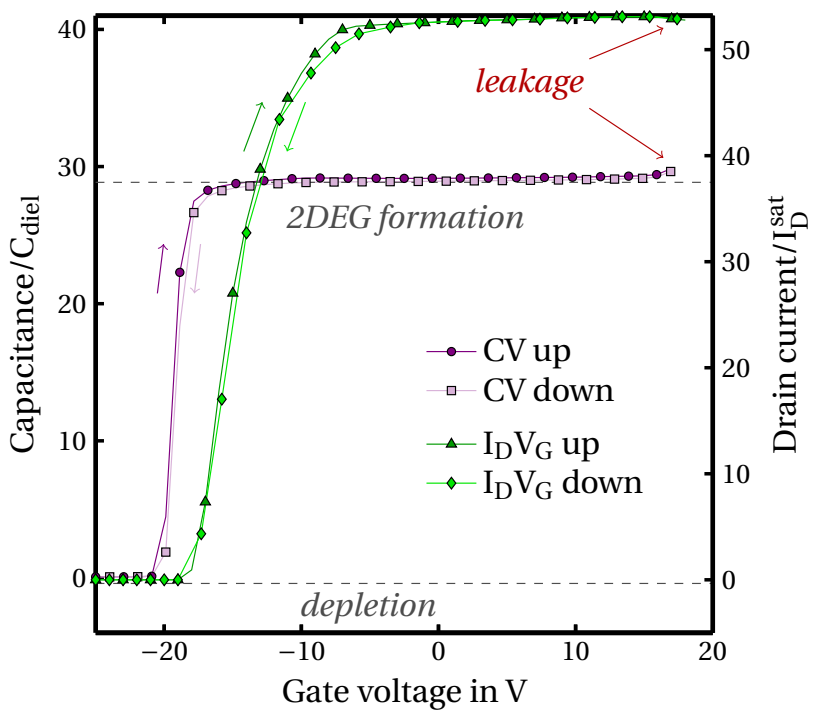

Figure 5.7. Capacitance–voltage and transfer characteristics of the fluorinated devices. The capacitance does not exhibit the second rise to the spill–over value before breakdown, and hysteresis is absent as well (from [96]).

Electron detrapping can be studied by holding the device at a certain positive bias, at which equilibrium conditions are reached before 1 µs, and then switch the voltage to a more negative value. Interestingly, drain current transients are observed at any gate voltage down to depletion. The increase of the current implies a negative shift of the transfer characteristic, as shown in Fig. 5.8a for a hold bias of 10 V and recovery voltages from 10 V to –20 V. For all recovery voltages, the current reaches a saturation value within 1 s. This means that after this time the negative shift has reached its final value, and the device does not drift anymore. As a consequence, the position of the transfer characteristics at subsequent times remains the same, as shown in Fig. 5.8b. This is the reason why we do not observe hysteresis with a standard double–sweep measurement, because it takes usually a few seconds to be performed. In this way, the device appears to be very stable.

This behavior can be explained with the presence of a very high density of interface states with an energy very close to the Fermi level. The band diagram during stress and recovery is illustrated in Fig. 5.9a: in equilibrium conditions, the traps are filled with electrons, and the drain current has the value 1, indicated in the transfer characteristic in Fig. 5.9b and as a function of time in Fig. 5.9c. When the gate bias is switched to more negative values, the Fermi level is brought down, the 2DEG is depleted and, consequently, the drain current decreases to the value 2. However, at this point the trapped electrons are emitted back to the 2DEG, resulting in an increase of the drain current to the value 3 and, eventually, to the value 4, which is almost the same as it was in equilibrium conditions. The increase of the drain current at constant recovery voltage corresponds to a negative shift ΔV, as shown in Fig. 5.9b with the sequence of consecutive transfer characteristics.

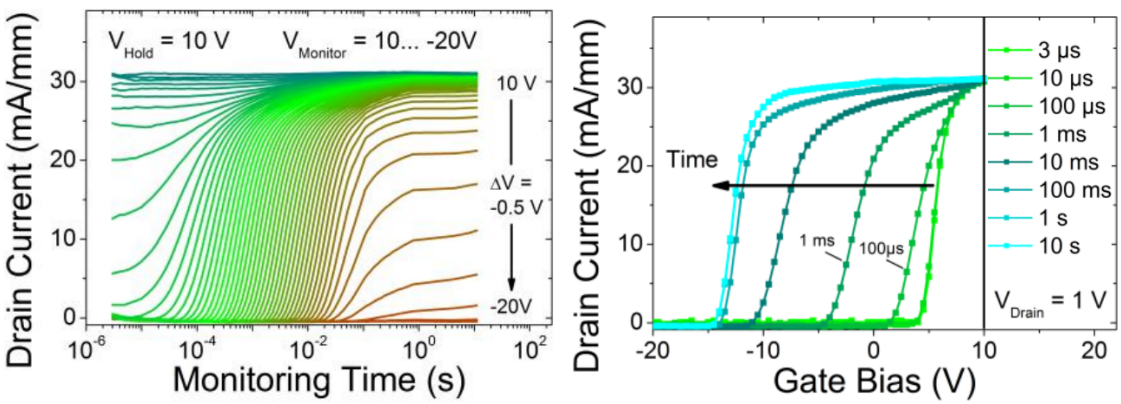

(a) (b)

Figure 5.8. Drain current transients (a) when the gate bias is switched from 10 V to a recovery voltage value from 10 V to –20 V. The transfer characteristics (b) are extracted by interpolating the drain current values at various times over all gate voltages. The negative shift saturates after about 10 ms (adapted from [54]).

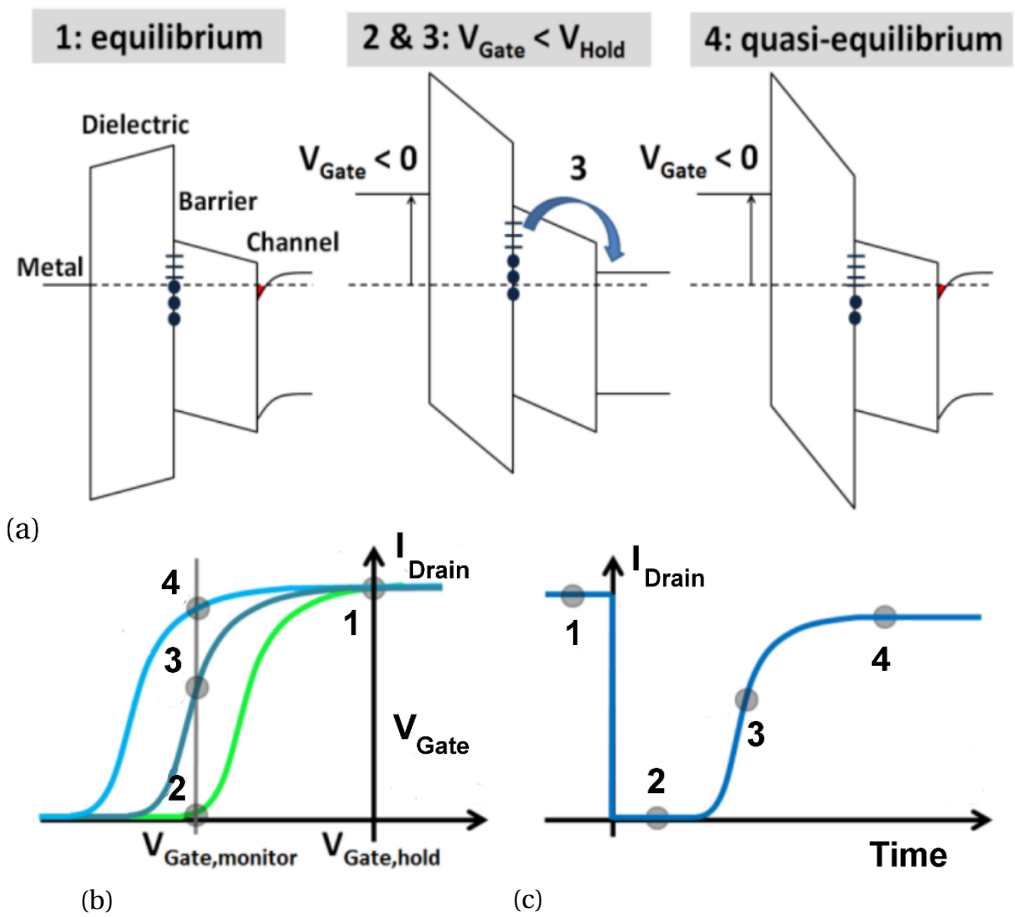

Figure 5.9. Band structure diagram (a), transfer characteristic (b) and time evolution of the drain current (c) in equilibrium conditions and during electron emission (adapted from [54]).

We study the temperature dependence of electron emission with a series of isothermal measurements at our probe station. We hold a stress bias of 10 V for a few seconds and then switch to the recovery voltage of –10 V, monitoring the drain current increase for 1 s. As expected, variations of the stress time from 1 s to 100 s did not affect the result, as the device remains in equilibrium conditions. We span a temperature range from –30 °C to 200 °C by using the thermostatic chuck. The results in terms of voltage shift as a function of time are shown in Fig. 5.10. We note that at higher temperatures the transients accelerates; however, the drain current always comes to the saturation value within 1 s. An exponential curve with a single time constant of 100 µs is also shown in order to compare the shape of the transient. It is clear that the measured curves, although quite fast in reaching saturation, cannot be properly fitted with a single exponential. For this reason, the activation energy would not have a single value but rather a narrow distribution around a mean value. We extract the activation energy spectrum with the Primak method in the next section.

5.2.2 Evaluation of the interface trap density

We analyze the dataset of Fig. 5.10 with the Primak method. The result is shown in Fig. 5.11: the value of τ_0 obtained with the optimization algorithm is 70 ns, and the D_{it} as a function of activation energy is narrowly distributed. We can fit the whole dataset with a gaussian function, using a mean value of 0.22 eV and standard deviation of 70 meV. We note that the width of the distribution is larger than the energy resolution of the Primak method, which has been estimated to be around 25 meV in Section 4.3.2. The density of defects per unit area and energy is 8×10^{13} cm^{-2}, few times larger than that of devices with the standard interface.

However, we can observe that not every part measured at different temperature connects with the others to build a smooth spectrum. This is true for any value of τ_0: longer characteristic time constants allow a good alignment of the measurements at low but not at high temperature, and vice versa for shorter time constants. This is an indication that the approximation of a constant τ_0 does not hold true in this case. In fact, as we have seen in Section 4.3.3, the Arrhenius plot extracted from this data (shown in Fig. 4.8) is not linear.

We have discussed few reasons that might explain such a behavior in Chapter 4. One of them is the presence of tunnelling as an additional charge transport mechanism next to NMP transitions, and the consequent failure of the classic approximation. We investigate the temperature dependence of E_A and τ_0 by repeating the Primak analysis in three separate groups of temperatures, combining together the three lowest values (-30, 0, 30 °C), the three highest (100, 150, 200 °C) and the remaining three ones in the middle range (30, 50, 100 °C). As shown in Fig. 5.12, the lower the temperature the smaller is the extracted activation energy. This would in principle fit to the model described in Fig. 4.3b. In fact, the impact of tunnelling over that of NMP transitions is larger at low temperatures. Therefore, the error made with the Primak approach, which assumes only NMP transitions for charge exchange, is larger at low tempera-

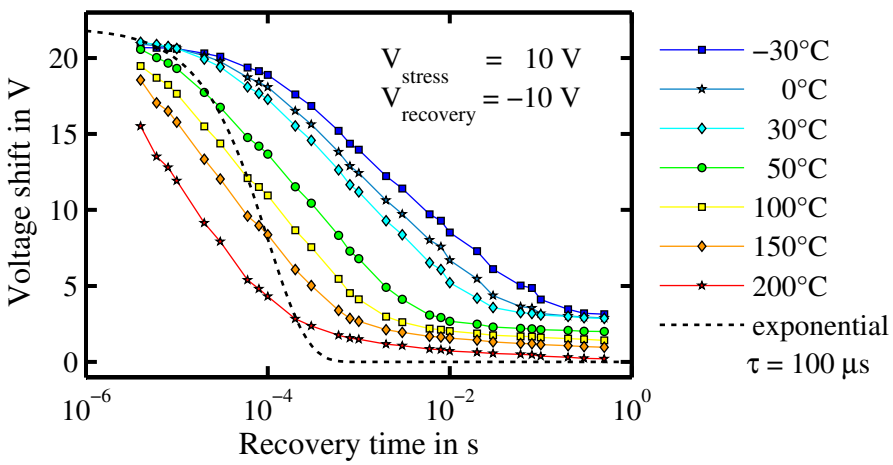

Figure 5.10. Time evolution of the threshold voltage shift of the devices with fluorinated interface during recovery at −10 V (from [96]).

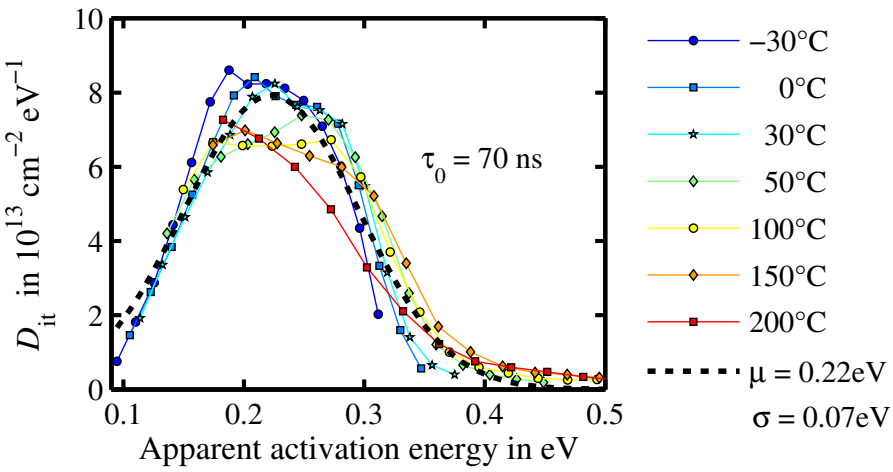

Figure 5.11. The spectrum of the density of interface defects is narrowly distributed in energy. We fit the data with a normal distribution with a mean value of μ = 0.22 eV and a standard deviation of σ = 0.07 eV (from [96]).

tures. In conclusion, according to this hypothesis the best estimate for the activation energy for electron emission is the one extracted at high temperature. In our case, we set the lower limit for E_A to be the one extracted with the fit at high temperature (labeled "fit 3" in Fig. 5.12). The result is a gaussian distribution with a mean of 0.32 eV and a standard deviation of 90 meV.

From all the experimental data and the Primak analysis we can conclude that the fluorination process results in a drastic modification of the defects at the AlGaN/dielectric interface, which makes the device behavior more stable. Since the 2DEG density is affected [54], fluorine plays a role in the modification of the surface donor states responsible for the creation of the

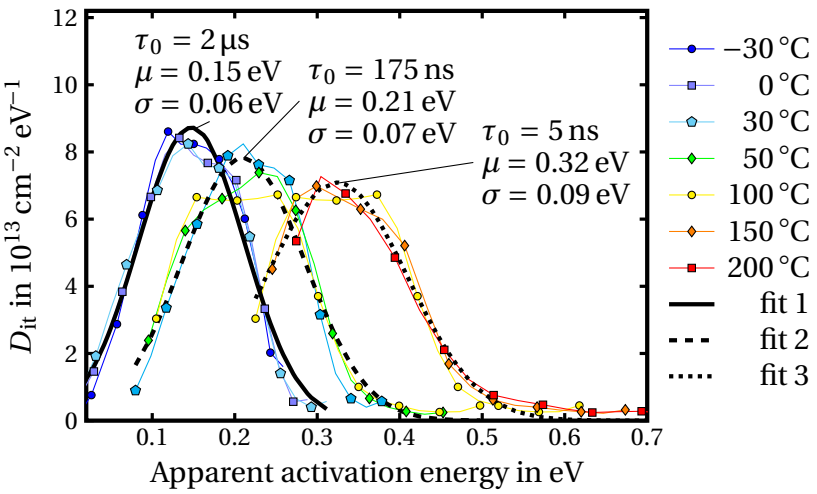

Figure 5.12. The D_{it} spectra extracted in three separate groups of temperatures. Group 1: -30, 0, 30°C, group 2: 30, 50, 100°C, group 3: 100, 150, 200°C. The optimized τ_0 values and the parameters of the gaussian fit μ and σ are reported in the figure (from [96]).

electron gas, at least partially. The new interface state has a narrowly distributed activation energy around a rather low mean value (0.32 eV) and a large density per unit area and energy (8×10^{13} cm^{-2}). The small E_A leads to the rather fast detrapping mechanism observed experimentally, while the D_{it} is large enough to cause the large voltage shift described in Fig. 5.9.

Physical–chemical investigations have shown that the fluorine radical F^- competes with the hydrolytic group OH^- for the AlGaN surface bonds, giving rise to a highly polarized bond [98]. This increases the electronegativity of the surface termination, which therefore results in a considerably different AlGaN/SiN interface than in standard devices. The modification impacts both the density and the dynamic response of the interface states. In conclusion, the fluorination process can be considered a “defect engineering” tool, capable of improving the device performance in terms of reliability.

6

Opto–electrical characterization of defects

OPTICAL CHARACTERIZATION METHODS allow us to access defects with very large activation energies, which would not be possible to characterize with electrical techniques only. During the course of this thesis the setup for combined optical and electrical characterization, described in Section 2.4, has been established. In this chapter, we present the theoretical foundations for the deep level optical spectroscopy (DLOS) experiment. We apply this method first to GaN/AlGaN samples for the characterization of impurities in the GaN buffer. Then, we investigate the effect of monochromatic light on MIS structures and on MIS–HEMTs, focusing on a method to distinguish defects at the AlGaN/dielectric interface from bulk states. We highlight the challenges of our standard test structures, arising mainly from the light absorption properties of the thick aluminum gate contact. Finally, we introduce new devices designed explicitly for optical investigations, featuring an evaporated gold (or gold and titanium) gate contact as thin as 5 nm, and the first results of DLOS characterization.

6.1 Effect of light on GaN/AlGaN test structures

In this first section we briefly summarize the main principles of optical transitions in charge exchange mechanisms, and we present the concept of the DLOS method. We describe the experimental approach and we analyze the data measured on simple GaN/AlGaN samples, in order to characterize the buffer defects responsible for vertical breakdown.

6.1.1 The DLOS experiment

When a semiconductor device is exposed to light, the photons of the optical radiation can interact with the electrons in the solid material. The motion of the electrons can be described by the hamiltonian H

$$H = -\frac{e\hbar}{i m^*} \vec{A} \cdot \nabla \tag{6.1}$$

where the vector potential of the electromagnetic field for monochromatic radiation is

$$\vec{A} = \vec{A}_0 \, \mathrm{e}^{i\left(\vec{k}\cdot\vec{r} - \omega t\right)}. \tag{6.2}$$

In the electric dipole approximation, we take the first order expansion of the exponential, therefore the hamiltonian Eq. (6.3) becomes simply

$$H = -\frac{e\hbar}{i m^*} \vec{A}_0 \cdot \nabla. \tag{6.3}$$

Electron emission from a trap can be modelled as the transition of the electron from a bound state (trapped, described by ψ_t) to a state in the conduction band (described by ψ_b), as introduced in Section 1.2.2. Applying time dependent perturbation theory, the probability that the electron moves from the trapped to the band state is given by the Fermi golden rule

$$P_\mathrm{tb} = \frac{2\pi}{\hbar} \left|\langle \psi_\mathrm{b} | H | \psi_\mathrm{t} \rangle\right|^2 \rho\left(E_\mathrm{b} - E_\mathrm{t} - \hbar\omega\right). \tag{6.4}$$

We introduce the *optical cross section*, which is defined as

$$\sigma_\mathrm{opt} = \frac{P_\mathrm{tb}}{\Phi_\mathrm{ph}}. \tag{6.5}$$

We note that the photon flux, Φ_ph, is proportional to the square modulus of the vector potential ($\Phi_\mathrm{ph} \propto |\vec{A}_0|^2 \, \hbar\omega$). In this way, the optical cross section does not depend on $\vec{A}$:

$$\begin{aligned} \sigma_\mathrm{opt} &\propto \frac{1}{\hbar\omega} \, |\langle \psi_\mathrm{b} | \hbar \frac{\partial}{\partial \vec{r}} | \psi_\mathrm{t} \rangle|^2 \, \rho\left(E_\mathrm{b} - E_\mathrm{t} - \hbar\omega\right) \\ &= \frac{1}{\hbar\omega} \, M_\mathrm{tb} \, \rho\left(E_\mathrm{b} - E_\mathrm{t} - \hbar\omega\right). \end{aligned} \tag{6.6}$$

Following the derivation of G. Lucovsky [99], we can make some assumptions in order to simplify Eq. (6.6). First, the matrix elements M_tb can be evaluated starting from the initial and final wavefunctions ψ_t and ψ_b. In the case of a defect located inside the semiconductor material, we can describe the bound state with a wavefunction of the kind

$$\psi_\mathrm{t}(r) = \frac{1}{\sqrt{2\pi a}} \frac{\mathrm{e}^{-r/a}}{r} \tag{6.7}$$

with $a = \sqrt{2 m_\mathrm{t} E_\mathrm{t}}/\hbar$, that can be derived from the assumption of a delta function potential. Furthermore, we can use the parabolic approximation to express the density of states $\rho(E)$:

$$\rho(E) = \frac{1}{2\pi^2} \left(\frac{2m^*}{\hbar^2}\right)^{3/2} \sqrt{E}. \tag{6.8}$$

This assumption is valid around the minimum of the conduction band edge, and for photon energies that do not largely exceed $E_\mathrm{t}^\mathrm{opt}$, the optical activation energy of the defect. The Lucovsky model for the optical cross section therefore reduces Eq. (6.6) to

$$\sigma_\mathrm{opt} \propto \frac{(\hbar\omega - E_\mathrm{t}^\mathrm{opt})^{3/2}}{(\hbar\omega)^3}. \tag{6.9}$$

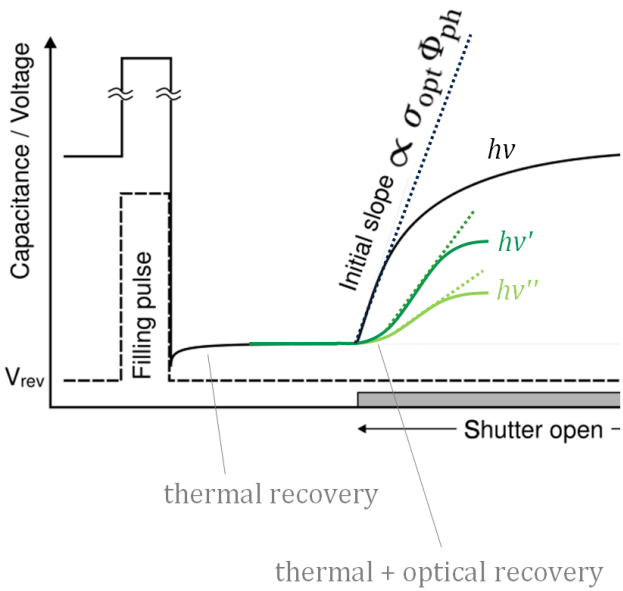

Figure 6.1. Illustration of the DLOS experiment. The optical cross section is extracted from the initial slope of the transients under optical exposure (adapted from [100]).

This model can be applied in the analysis of experimental data measured during exposure to monochromatic light. We consider the recovery transient of current (or capacitance) after a certain stress has been applied to the device. Under stress conditions the traps capture electrons, that are then emitted during recovery. The rate of emission under exposure depends on temperature and on the energy of the optical radiation. We have discussed the characteristic time constant for non–radiative transitions in the previous chapters. The rate of emission due to optical radiation is instead

$$\alpha(\hbar\omega) = \sigma_{\mathrm{opt}}(\hbar\omega)\,\Phi_{\mathrm{ph}}(\hbar\omega), \tag{6.10}$$

which gives rise to exponential transients of the kind

$$I(\mathrm{t}) \propto \mathrm{e}^{\alpha(\hbar\omega)\,t}. \tag{6.11}$$

For this reason, as a first approximation, the initial slope of the transient, normalized to the photon flux, is proportional to the optical cross section. From a series of measurements at various values of photon energies, we can therefore extract the optical cross section as a function of energy. This approach is very similar to the deep level transient spectroscopy, with the difference that the temperature is kept as low as possible to minimize thermal emission, and the parameter to be varied is the photon energy. For this reason, it has been named *deep level optical spectroscopy* (DLOS) [33, 101]. The experimental procedure is illustrated in Fig. 6.1. As shown in the figure, a solution to minimize the impact of thermal emission is to wait a short time before turning on the light, so that the trap states with small thermal activation energy

emit all their electrons already in dark conditions. At this point, only the states with larger optical activation energy contribute to the recovery transient measured during exposure. The optical cross section can be therefore extracted in an accurate way. At this point, the Lucovsky model of Eq. (6.9) can be used to evaluate the optical activation energy of the trap states, E_t^{opt}, and consequently to give an interpretation of the identity or possible origin of the defect.

6.1.2 C and Mg impurities characterized with O–DLTS

We apply the DLOS method to GaN/AlGaN structures grown on silicon. They have a circular Schottky contact on top, with a diameter of 100 µm that leaves a large area of the AlGaN exposed to the light. We investigate two kind of GaN buffers, intentionally doped with carbon (with a density of about 10^{16} cm^{-3}) and magnesium (10^{19} cm^{-3}). We bring the devices very close to vertical breakdown, applying about 400 V between the top and bottom contacts. In this way, it is possible to generate a vertical leakage current by photogeneration, by exposing the structure to monochromatic light. We observe the maximum effect when the photon energy is the same

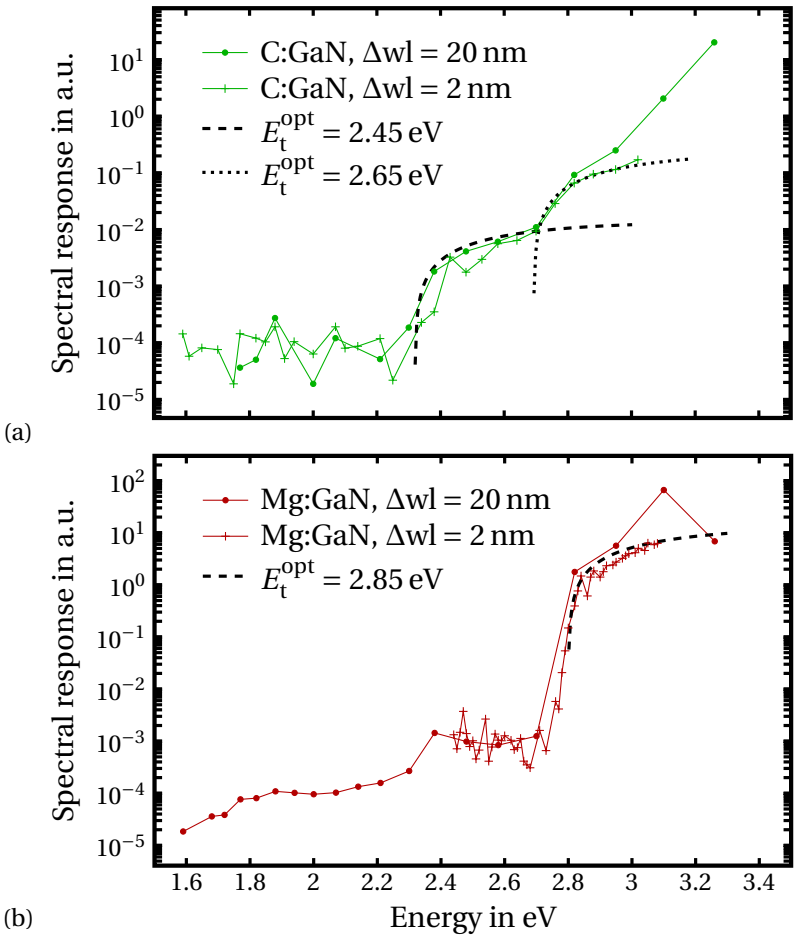

Figure 6.2. Results of the DLOS experiment on GaN/AlGaN devices with carbon–doped (a) and magnesium–doped GaN buffer (b).

as that of the bandgap, i.e., 3.39 eV. In addition, we expect to see a "shoulder" to the main peak at energies corresponding to the optical activation energy of the trap states, that contribute to the leakage current by emitting electrons at $\hbar\omega = E_t^{opt}$. The trap energy can be extracted with a fit to the data according to Eq. (6.9).

The spectra of the two investigated samples are shown in Fig. 6.2. We extract the spectral response of the structure under illumination, given in arbitrary units, which is proportional to the optical cross section. In fact, the normalization obtained by dividing dI/dt through the photon flux would be correct also in absolute values only if the complete light beam was absorbed by the active area of the device. Since its dimensions are much smaller than that of the beam, it is not possible to completely focus the light onto it. As a consequence, only a fraction of the photons actually illuminates the sample, therefore we can correct our results only for the relative difference of the photon flux within the energy range used. Nevertheless, a fit to the data with the Lucovsky model can give us a good estimate of the optical energy E_t^{opt} of the active defects.

As we can see in Fig. 6.2a, in the carbon–doped sample we can fit two contributions from states with optical activation energy of 2.45 eV and 2.65 eV. Such defects are usually associated to the gallium vacancy in the GaN buffer [34, 35]. The carbon related contribution could be at the upper limit of the energy used for this experiment, as it has been found in other measurements to be around 3.3 eV.

On the other hand, the magnesium–doped sample shows a large shoulder at 2.85 eV, which has in fact been related in literature to the magnesium impurity in GaN [34, 101].

6.2 Effect of light on MIS structures

We next investigate the effect of monochromatic illumination on the impedance characteristic of MIS structures. For comparison, we use both SiC and GaN–based devices. They have similar bandgap energy, namely 3.23 eV (equivalent to a wavelength of 384 nm) for 4H–SiC and 3.39 eV (or 365 nm) for GaN. We expect the largest impact to happen when the photon energy equals or slightly exceeds that of the bandgap, which is large enough for the photons to generate minority carriers. At smaller energies only photoionization takes place, which means that electrons trapped in defect states can be emitted by means of optical radiation.

6.2.1 Exposed CV characteristics of SiC devices

For the first investigations about the impact of light onto MIS devices, we use 4H–SiC MIS samples structured in two different ways. Regular devices have a planar geometry, with an aluminum gate contact as the top layer above the MIS structure. Other devices instead are designed differently, without the thick metal layer above the active area of the device. As we will

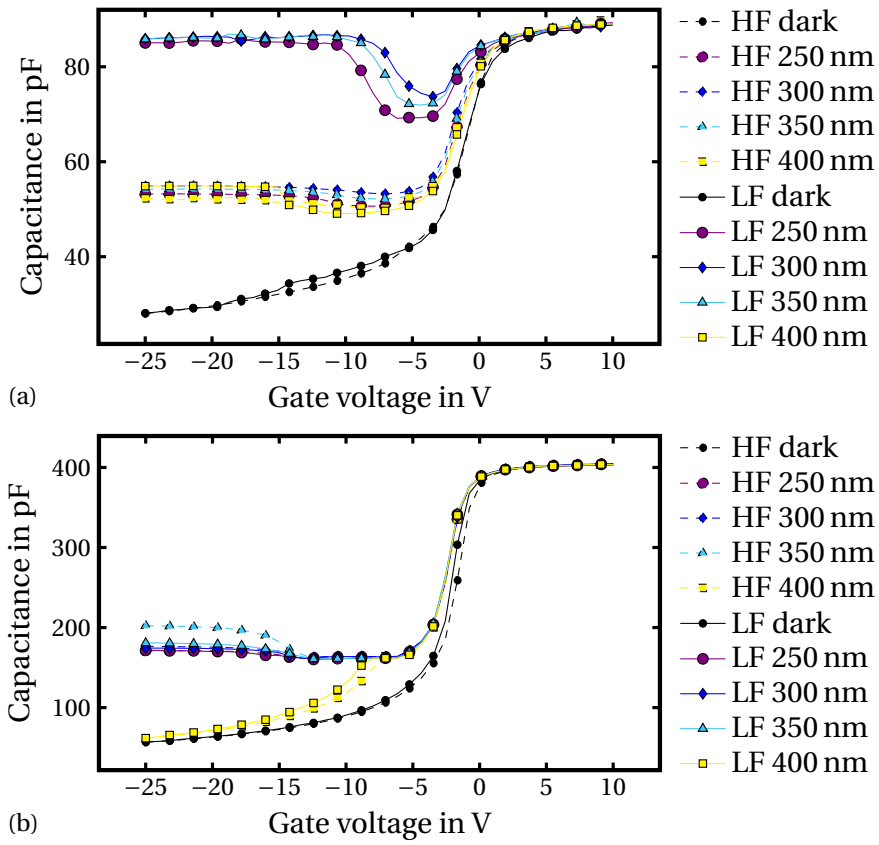

Figure 6.3. Exposed CV curves of SiC MIS structures: optimized (a) and regular devices (b). The curves labeled with "HF" have been measured at 100 kHz, those with "LF" at 100 Hz. The bandpass of the monochromator is 20 nm.

prove in this Section, these devices are optimized to maximize the absorption of optical radiation in the SiC.

In Fig. 6.3a we can see the CV curves of the optimized SiC device under exposure to monochromatic light. In this case, when the photon energies match that of the bandgap, minority carriers are created. In this way, at 100 kHz we can measure the high frequency curve limit instead of the deep depletion curve [38]. At 100 Hz the number of generated minority carriers is enough to build the inversion layer at the SiC/dielectric interface, thus shielding the depletion region in the bulk and making the capacitance rise to C_{diel}. We note that a photon energy lower than the bandgap does not allow for the creation of enough minority carriers, although it will still impact capture and emission processes.

The regular devices instead do not show the same results: the inversion layer cannot be formed by photogeneration, even if the photon energy exceeds that of the bandgap and the frequency is low. We can see in Fig. 6.3b that a certain amount of minority carriers is created, but the effect is considerably smaller. The result does not change even by using the low resolution grating, which allows a higher light power by increasing the bandpass of the monochromator.

This is due to the presence of the gate contact on top of the device, an aluminum layer with a thickness slightly smaller than 1 µm, which absorbs almost completely the incident radiation. Experiments with different angles of radiation did not change the outcome considerably. We must conclude that such contacts unfortunately block most of the light, therefore shielding the active area of the device from illumination.

6.2.2 Exposed CV characteristics of GaN devices

Next, we investigate the impedance characteristics of GaN/SiN MIS samples under exposure to light. The test structures have a planar design and a circular shape with an aluminum contact that does not cover entirely the device, thus leaving a certain amount of SiN surface exposed to the optical radiation. In this way, even if the thickness of the aluminum layer is the same as for the SiC regular devices, we can see the impact of light on the capacitance– and conductance–voltage characteristics, as shown in Fig. 6.4.

Differently than in SiC MIS structures, the light causes a negative shift of the impedance curves, and just a very slight increase of capacitance at reverse bias. The increase of capacitance can be explained by the shrinking of the depletion region, due to the presence of minority carriers at the GaN/SiN interface. However, it seems that the major effect is the recombination of the generated holes with the electrons in trapping centres, which results in a large negative drift [40]. In other words, optical radiation causes the photoionization of defects that would not emit the trapped electron at the applied gate bias in dark conditions, because they are located below the Fermi level.

We also note that, at energies lower than that of the bandgap, a ledge appears in the CV curve and a second peak in the conductance characteristics. These are probably related to

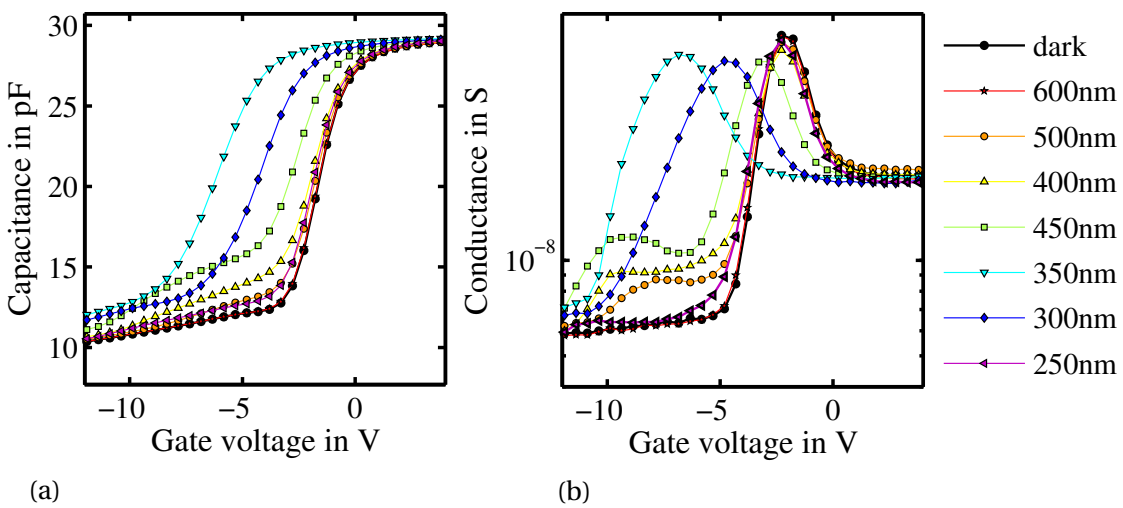

Figure 6.4. Capacitance (a) and conductance (b) curves of the standard GaN/SiN MIS structures, in dark conditions and under exposure to monochromatic light.

a specific defect type, whose photoionization energy matches the wavelength used. The fact that the bias range where this effect is visible is in depletion suggests that these trap states are located in the buffer. We study the effect of exposure to monochromatic light at different wavelengths in more detail with the DLOS experiment in the next section.

6.3 Effect of light on GaN/AlGaN MIS–HEMTs

In this section we present the DLOS investigations on fully processed GaN/AlGaN MIS–HEMTs, the challenges that we have found, the solutions and the first results. The main problem has been the shielding effect of the thick aluminum gate contact, which prevented the light to properly illuminate the device. For this reason, new test structures have been fabricated choosing a more suitable material and realizing a the thinnest layer possible for contacting. Finally, we report and interpret the DLOS spectra measured on the new devices.

6.3.1 DLOS on standard MIS–HEMTs

Our goal with the DLOS experiment is to characterize the defect levels with large activation energy present in our devices, and try to understand the impact of the defects at the AlGaN/SiN interface. In order to do so, we compare the DLOS spectra with and without a filling pulse at positive gate voltage. As we have discussed in the previous chapters, applying a forward gate bias results in electron trapping at the interface we are interested in. With the DLOS experiment we are going to evaluate the impact of light on the recovery from such a stress. We must note that, due to the broad distribution of time constants, we would always observe a combination of thermal and optical emission, at all temperatures and during the whole transient. However, we are going to analyze the recovery transients with the method described in Section 6.1.1 and extract the spectral response of our test structures under different values of recovery voltage.

In the first place, we must take into account that the application of any read out voltage different from zero results in a V_{th} drift of the device (see the description of the hysteresis effect in Section 3.2.2). The challenging feature is that the drift would be different when the same stress/recovery pattern is used more than once (see again Fig. 3.15b). This is problematic for the DLOS experiment because we need to repeat the filling pulse and the recovery for all different values of light energy in order to have a well–resolved spectrum. The solution used here is to repeat ten times a full sweep of gate voltage from depletion to 0 V, until the voltage shift approaches saturation. In this way, the conditions of the devices are always approximately the same at the beginning of every cycle of stress/recovery.

We measure the drain current of the MIS–HEMTs, performing the so–called current–DLOS (I–DLOS) experiment. We apply a constant voltage between the drain and the source contact of 2 V. The recovery transients are shown in Fig. 6.5 for a read out voltage of –20 V, which is one of the gate bias points where the effect of the light is largest. Unfortunately, we observe that the

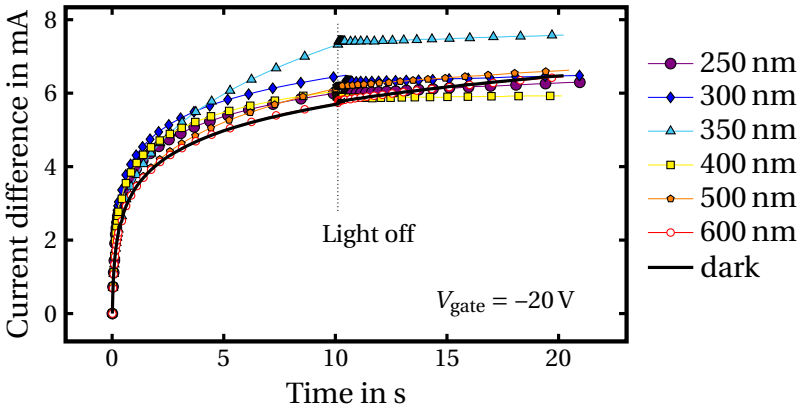

Figure 6.5. I–DLOS transients of the standard GaN/AlGaN/SiN MIS–HEMTs at a read out voltage of –20 V, in dark conditions and under exposure to monochromatic light. The initial value of current is subtracted for better comparison. Unfortunately, the difference between the various photon energies used is very small.

impact of light is much smaller than that of the drift due to the applied gate bias. In fact, only the curve at 350 nm, the one matching the energy of the bandgap, results in a clear increase of drain current with respect to the transient measured in dark conditions. As a consequence, the extraction of the optical cross section gives a very poor and noisy spectrum. The cause has been found to be the thick aluminum contact on top of the active area, which almost entirely absorbs the optical radiation. For this reason, we prepared new test structures dedicated to experiments with light, as presented in the next section.

6.3.2 Thin gold contacts on MIS–HEMTs for optical characterization

A proper choice of the metal to realize the top contact can be made after evaluating the absorption coefficient, α, of the material. According to the Beer–Lambert law, the intensity of an electromagnetic wave propagating in a medium decays as

$$I(x) = I_0 \, \mathrm{e}^{-\alpha(\hbar\omega)x} \tag{6.12}$$

where x is the distance and α depends linearly on the extinction coefficient κ, i.e., the imaginary part of the complex reflective index.

Fig. 6.6 shows the absorption coefficient of aluminum, gold and titanium as a function of the photon wavelength. As we can see, α is almost one order of magnitude larger for aluminum with respect to the other two metals. In fact, Al is one of the most reflecting materials and is used to make the gratings of monochromators, where maximum reflectance over a broad range of wavelengths is required. On the other hand, gold and titanium are both good choices to realize a gate contact that could transmit part of the optical radiation to the device underneath. Referring to monochromatic light with a wavelength of 350 nm, we can calculate the ratio be-

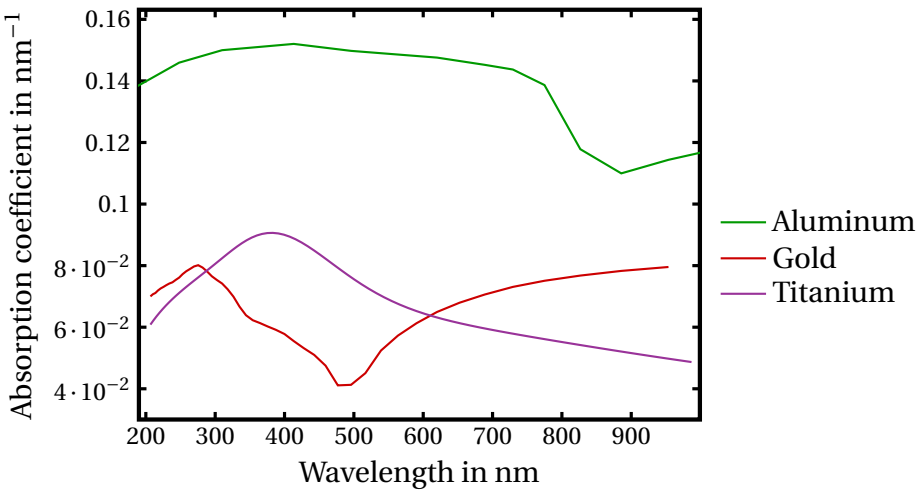

Figure 6.6. The absorption coefficient of aluminum, gold and titanium as a function of the wavelength [102–104].

tween the intensity of the incident light and that after 1 nm of metal in the three cases. The results are reported in Table 6.1.

While gold and titanium let through more than 90% of the incident light, for aluminum the percentage is 85%. A layer of aluminum 50 nm thick is already enough to bring the percentage of transmitted light to lower than 1%. It is therefore clear that our first devices, featuring several hundreds of nanometers of aluminum on top, are not the ideal test structures for optical investigations. The impact of light we measured in the previous section is probably due to the very small SiN area that is not covered by the gate.

The gate contact of the new test structures has been realized by evaporation of gold and, to ensure a better adhesion to the SiN, with an additional layer of titanium between the gold and the AlGaN. Four wafers with different layer thicknesses have been fabricated, summarized in Table 6.2 together with the estimate of the transmitted to incident light ratio at 350 nm.

Most of the devices on all wafers can be successfully contacted with the needles of the probe station, even though care must be taken in the process. The device to device variation in the contact quality is quite large, giving rise to a variation in the saturation drain current measurement that can reach 20%. However, we can use a single test structure for a full DLOS ex-

Material	α in nm^{-1}	I/I_0
Aluminum	0.144	0.85
Titanium	0.089	0.92
Gold	0.063	0.94

Table 6.1. Absorption coefficient at 350 nm and the ratio between incident and transmitted light through 1 nm of material.

Layer thickness in nm		
Titanium	Gold	I/I_0
0	5	0.73
0	20	0.28
3	5	0.56
3	20	0.22

Table 6.2. Composition and thickness of the gate contact of the four type of MIS–HEMTs dedicated to optical experiments. The ratio between incident and transmitted light at 350 nm is calculated as well.

periment. In fact, we perform a series of ten identical voltage sweep between every read out transient under exposure, which enables us to bring the device always to the same conditions prior to the measurement.

The transients measured at a read out voltage of –20 V are shown in Fig. 6.7. By comparison with Fig. 6.5, it is clear that the effect of light on the new structures is much larger. This allows the proper execution of I–DLOS investigations, that are the object of the next section.

6.3.3 DLOS on MIS–HEMTs with thin gold contacts

The large impact of light on the I–DLOS transients allows us to extract the spectral response of the device, which is directly proportional to the optical cross section. In general, we obtain an increase of the spectral response with the photon energy, with few clear "shoulders" that can be fitted with the Lucovsky model. The energy range of our setup goes from 2 eV to about 5 eV, which is still below the 6.2 eV bandgap of the SiN material.

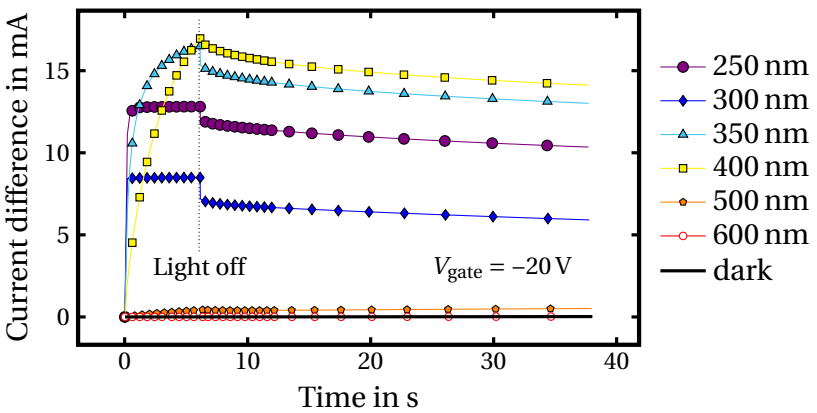

Figure 6.7. I–DLOS transients of the MIS–HEMTs with a 5 nm gold layer as the gate contact, under dark conditions and under monochromatic light exposure. The initial value of the current is subtracted for better comparison.

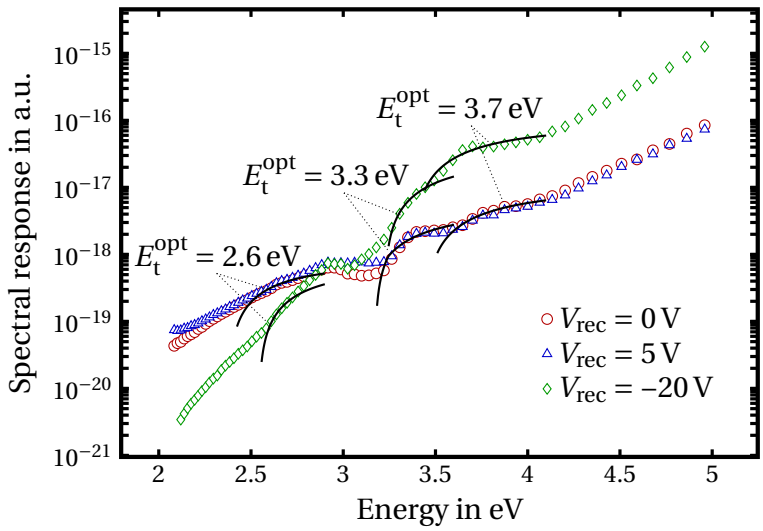

Figure 6.8. Result of the I–DLOS experiment on the GaN/AlGaN MIS–HEMTs with a 5 nm gold layer as the gate contact, at different values of read out voltage. The Lucovsky model has been used for the fit of the three defect states.

Fig. 6.8 shows the result of the I–DLOS experiment without the positive bias filling pulse, at the read out voltages of 0 V, 5 V (spill–over conditions) and –20 V (depletion conditions). The shape of the spectral response at 0 V and 5 V is basically the same. We can distinguish three trap–related "shoulders". At –20 V we see the same trap levels, but the magnitude of the one at low energy is larger. Since the measurement in depletion is the most sensitive to buffer traps, these defects are probably located in the GaN bulk.

The three states have optical activation energies of 2.6 eV, 3.3 eV and 3.7 eV. The defect with E_t^{opt} = 2.6 eV has been measured extensively in literature, as well as in the carbon–doped samples in Section 6.1.2, and it is usually related to the gallium vacancy in the GaN buffer [105]. The level at 3.3 eV is also often observed in MOCVD grown structures and is likely due to the carbon substitutional defect in the GaN [105, 106]. The last trap state at energy 3.7 eV might be located in the AlGaN layer. In fact, its origin has been suggested to be the carbon substitutional defect in the AlGaN material [35, 106].

We investigate the effect of a filling pulse at positive gate bias, namely 5 V for 10 s. When the read out voltage is 0 V, the difference with and without filling pulse is just a slight modification of the spectrum at low energy, around 2 eV, as shown in Fig. 6.9a. However, this is indeed too small to perform a Lucovsky fit. The other three states at 2.6 eV, 3.3 eV and 3.7 eV are still present.

In depletion conditions, the presence of the filling pulse results in a clearer additional level at low energies. The fit to the data in Fig. 6.9b suggests a trap with optical activation energy of 2.3 eV. Such a defect has been measured previously [105, 106], and it has been related to the access region when a SiN passivation is used. Under this assumption, this would be the

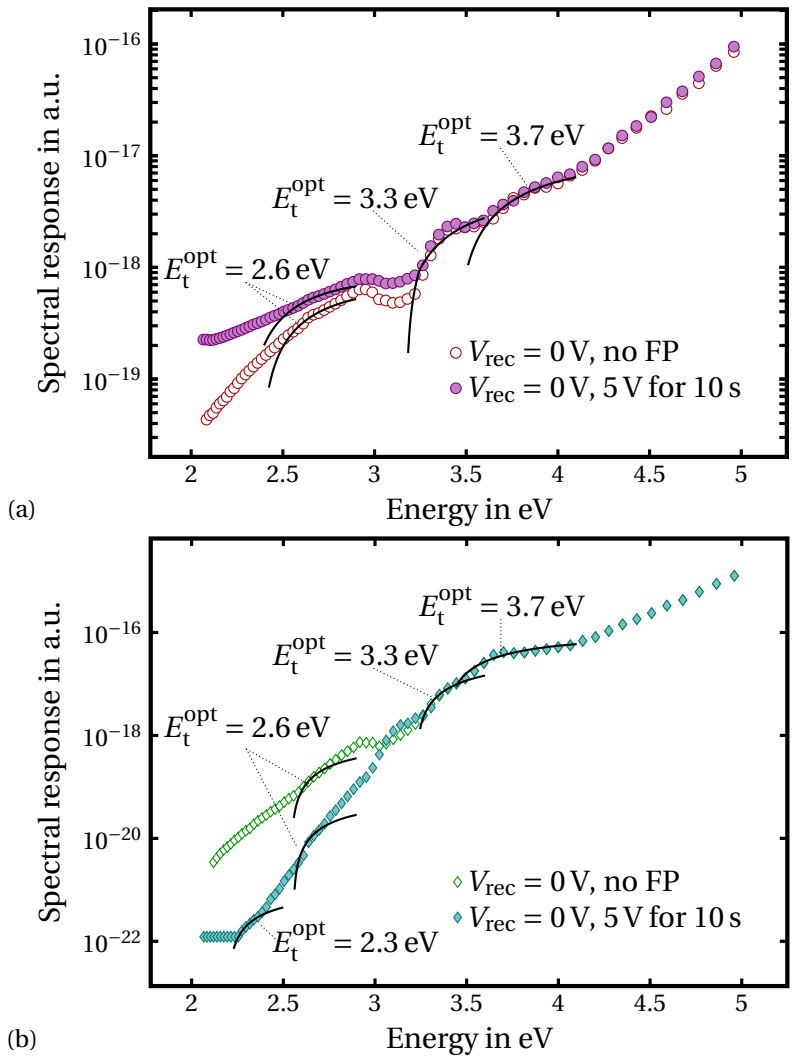

Figure 6.9. Result of the I–DLOS experiment on the GaN/AlGaN MIS–HEMTs with a 5 nm gold layer as the gate contact, with and without a forward gate bias filling pulse. The read out voltages used are 0 V (a) and –20 V (b).

fingerprint of a defect state at the AlGaN/SiN interface. The fact that this level arises only when a filling pulse at forward gate bias is used confirms this hypothesis.

In conclusion, the I–DLOS experiment has been successfully performed on structures with a thin gold gate contact, allowing the extraction of the optical energy of several active trap levels. The comparison of the spectra at various read out biases and after different filling pulses can aid the identification of the defects, as well as their location inside the device.

7

Conclusions

IN THIS WORK we have addressed the problem of characterizing the defects at the interface between the AlGaN barrier and the dielectric in composite GaN/AlGaN/SiN MIS–HEMTs. Such states act as trapping centres for electrons, causing severe threshold voltage shifts that compromise correct device operation.

The first result of this thesis is that most of the well–known, established methods for interface trap characterization based on the analysis of the impedance characteristics are inappropriate for GaN/AlGaN devices. In fact, while these techniques are used successfully on silicon structures, several approximations do not hold true for GaN–based samples. This is mainly due to the response of the barrier in the composite GaN/AlGaN stack.

Secondly, we have developed an accurate method for characterizing the defects at the interface with the dielectric, based on the study of the device response to a forward bias DC stress applied to the gate. The fundamental approach is the same as that already in use for bias temperature instability investigations on silicon MOSFETs. We have optimized such techniques for our test structures, taking into account their high level of instability and their sensitivity to the measurement parameters. A series of experiments of this kind at various temperatures has allowed us to extract the density of interface traps as a function of their activation energy for electron trapping.

We have found that the GaN/AlGaN/SiN devices with a standard interface have a rather high density of trap levels (10^{13} cm^{-2} eV^{-1}). The most important feature of such defects is their broadly distributed activation energy. In fact, the density of traps per unit area and energy does not fall below 5×10^{12} cm^{-2} eV^{-1} in a continuous range from 0.1 eV to 0.8 eV, with a slight increase at the lower extrema. This results can be explained by the disordered nature of the AlGaN/SiN interface, that is characterized by a non–stoichiometric, nanometer–thick interlayer between the two materials. Here, the point defects might have a number of slightly different microscopical arrangements, giving rise to a broad distribution of activation energies for charge trapping.

On the other hand, MIS–HEMTs that undergo a plasma cleaning process involving fluorine of the AlGaN surface before the deposition of the dielectric exhibit unique charge trapping behavior. In fact, in this case we have measured a larger density of traps, namely 8×10^{13} cm^{-2} eV^{-1}, with activation energies normally distributed around 0.32 eV. As a consequence, the trapping transients are very fast and threshold voltage shifts saturate within one second. This results in a stable device behavior that has never been observed before. The fundamental change with respect to the structures with a standard interface suggests that the fluorination process passivates the defects at the AlGaN surface and substitutes them with another kind of trap level, characterized by a well–defined activation energy and a larger density per unit area and energy.

Finally, we have established a setup and developed an improved design for test structures for combined electrical and optical experiments, aimed to investigate trap levels with large activation energies. The first results indicate the presence of several trap states that have been observed previously by other authors, mainly related to vacancies and impurities in the GaN or the AlGaN. Furthermore, we have observed a defect level with optical activation energy of 2.3 eV that could be located at the AlGaN/SiN interface, as is visible only after the application of a positive gate bias stress.

Outlook

This thesis offers different methods for the characterization of interface traps at the AlGaN/dielectric interface of GaN–based devices, that can be used to extend our knowledge about such defects. For example, further experiments on various test structures fabricated with different process treatments, together with physical–chemical investigations, would be helpful to understand the elements involved in the creation and the passivation of the trap states. This would constitute a step forward towards the identification of the root cause of these defects.

Furthermore, the results on the standard AlGaN/SiN interface can be complemented by additional measurements at lower temperatures and better time resolution. This would clarify whether the observed increase of density of traps around 0.1 eV is just the tail of a normal distribution.

Finally, the optical investigations have just been started during the final phase of this thesis. Further DLOS experiments and other combinations of electrical and optical excitation can be performed on any test structure with a suitable gate contact. With these techniques it is possible to study capture and emission events caused by the interaction of the system with phonons (non–radiative transitions), as well as with photons (optical transitions), thereby characterizing the electronic as well as the optical activation energy of the defects. In this way, it will be possible to achieve a complete picture of the charge exchange transitions taking place at the defect sites.

Bibliography

[1] C. Wood and D. E. Jena, Eds., *Polarization Effects in Semiconductors: From Ab Initio Theory to Device Applications*. Springer, 2007.

[2] D. Marcon, "Reliability study of power gallium nitride based transistors," Ph.D. dissertation, Katholieke Universiteit Leuven, 2011.

[3] F. Fornetti, "Characterisation and performance optimisation of GaN HEMTs and amplifiers for radar applications," Ph.D. dissertation, University of Bristol, 2010.

[4] O. Ambacher, "Growth and applications of group III–nitrides," *Journal of Physics D: Applied Physics*, vol. 31, no. 20, p. 2653, 1998.

[5] R. Chierchia, "Strain and crystalline defects in epitaxial GaN layers studied by high–resolution X–ray diffraction," Ph.D. dissertation, Universiy of Bremen, 2007.

[6] S. Pearton, *GaN and Related Materials II*, ser. Optoelectronic properties of semiconductors and superlattices. Taylor & Francis, 2000.

[7] "University Wafer, Inc. Educational supplies," http://www.universitywafer.com/, accessed October 2016.

[8] K. F. Brennan and A. S. Brown, *Semiconductor Heterostructures*. John Wiley & Sons, Inc., 2003, pp. 14–83.

[9] S. R. Lee, D. D. Koleske, K. C. Cross, J. A. Floro, K. E. Waldrip, A. T. Wise, and S. Mahajan, "In situ measurements of the critical thickness for strain relaxation in AlGaN/GaN heterostructures," *Applied Physics Letters*, vol. 85, p. 6164, 2004.

[10] J. P. Ibbetson, P. T. Fini, K. D. Ness, S. DenBaars, J. Speck, and U. Mishra, "Polarization effects, surface states, and the source of electrons in AlGaN/GaN heterostructure field effect transistors," *Applied Physics Letters*, vol. 77, p. 250, 2000.

[11] R. Vetury, N. Q. Zhang, S. Keller, and U. K. Mishra, "The impact of surface states on the DC and RF characteristics of AlGaN/GaN HFETs," *IEEE Transactions on Electron Devices*, vol. 48, no. 3, pp. 560–566, Mar 2001.

[12] Z. H. Feng, R. Zhou, S. Y. Xie, J. Y. Yin, J. X. Fang, B. Liu, W. Zhou, K. J. Chen, and S. J. Cai, "18–GHz 3.65–W/mm enhancement–mode AlGaN/GaN HFET using fluorine plasma ion implantation," *IEEE Electron Device Letters*, vol. 31, no. 12, pp. 1386–1388, Dec 2010.

[13] Y. Uemoto, M. Hikita, H. Ueno, H. Matsuo, H. Ishida, M. Yanagihara, T. Ueda, T. Tanaka, and D. Ueda, "Gate injection transistor (GIT): A normally–off AlGaN/GaN power transistor using conductivity modulation," *IEEE Transactions on Electron Devices*, vol. 54, no. 12, pp. 3393–3399, Dec 2007.

[14] T. Oka and T. Nozawa, "AlGaN/GaN recessed MIS–gate HFET with high–threshold–voltage normally–off operation for power electronics applications," *IEEE Electron Device Letters*, vol. 29, no. 7, pp. 668–670, July 2008.

[15] P. A. Laplante, Ed., *Comprehensive Dictionary of Electrical Engineering, Second Edition*. CRC Press, Taylor & Francis Group, 2005.

[16] J. A. Del Alamo and J. Joh, "GaN HEMT reliability," *Microelectronics Reliability*, vol. 49, no. 9–11, pp. 1200–1206, 2009.

[17] G. Meneghesso, G. Verzellesi, F. Danesin, F. Rampazzo, F. Zanon, A. Tazzoli, M. Meneghini, and E. Zanoni, "Reliability of GaN high–electron–mobility transistors: state of the art and perspectives," *IEEE Transactions on Device and Materials Reliability*, vol. 8, no. 2, pp. 332–343, June 2008.

[18] D. A. Joh and J. A. Del Alamo, "A current–transient methodology for trap analysis for GaN high electron mobility transistors," *IEEE Transactions on Electron Devices*, vol. 58, pp. 132–140, 2011.

[19] A. Santarelli, R. Cignani, G. P. Gibiino, D. Niessen, P. A. Traverso, C. Florian, D. M. M. P. Schreurs, and F. Filicori, "A double–pulse technique for the dynamic I/V characterization of GaN FETs," *IEEE Microwave and Wireless Components Letters*, vol. 24, no. 2, pp. 132–134, Feb 2014.

[20] D. Bisi, M. Meneghini, C. de Santi, A. Chini, M. Dammann, P. Brückner, M. Mikulla, G. Meneghesso, and E. Zanoni, "Deep–level characterization in GaN HEMTs – part I: Advantages and limitations of drain current transient measurements," *IEEE Transactions on Electron Devices*, vol. 60, no. 10, pp. 3166–3175, Oct 2013.

[21] C. Y. Hu and T. Hashizume, "Non–localized trapping effects in AlGaN/GaN heterojunction field–effect transistors subjected to on–state bias stress," *Journal of Applied Physics*, vol. 111, no. 8, 2012.

[22] C. Ostermaier, P. Lagger, M. Alomari, P. Herfurth, D. Maier, A. Alexewicz, M. A. di Forte-Poisson, S. L. Delage, G. Strasser, D. Pogany, and E. Kohn, "Reliability investigation of the degradation of the surface passivation of InAlN/GaN HEMTs using a dual gate structure," *Microelectronics Reliability*, vol. 52, no. 9–10, pp. 1812–1815, 2012.

[23] E. Zanoni, M. Meneghini, G. Meneghesso, D. Bisi, I. Rossetto, and A. Stocco, "Reliability and failure physics of GaN HEMT, MIS-HEMT and p–gate HEMTs for power switching applications: Parasitic effects and degradation due to deep level effects and time–dependent breakdown phenomena," in *IEEE Workshop on Wide Bandgap Power Devices and Applications*, Nov 2015, pp. 75–80.

[24] D. Marcon, G. Meneghesso, T. L. Wu, S. Stoffels, M. Meneghini, E. Zanoni, and S. Decoutere, "Reliability analysis of permanent degradations on AlGaN/GaN HEMTs," *IEEE Transactions on Electron Devices*, vol. 60, no. 10, pp. 3132–3141, Oct 2013.

[25] A. M. Stoneham, "Non–radiative transitions in semiconductors," *Reports on Progress in Physics*, vol. 44, no. 12, p. 1251, 1981.

[26] B. H. Brandsen and C. J. Joachain, *Physics of atoms and molecules*. Pearson Prentice Hall, 1983.

[27] T. Grasser, "Stochastic charge trapping in oxides: From random telegraph noise to bias temperature instabilities," *Microelectronics Reliability*, vol. 52, no. 1, pp. 39–70, 2012.

[28] T. Zhu and R. A. Oliver, "Unintentional doping in GaN," *Physical Chemistry Chemical Physics*, vol. 14, pp. 9558–9573, 2012.

[29] P. Bogusławski, E. L. Briggs, and J. Bernholc, "Amphoteric properties of substitutional carbon impurity in GaN and AlN," *Applied Physics Letters*, vol. 69, no. 2, pp. 233–235, 1996.

[30] C. H. Seager, A. F. Wright, J. Yu, and W. Götz, "Role of carbon in GaN," *Journal of Applied Physics*, vol. 92, no. 11, pp. 6553–6560, 2002.

[31] A. F. Wright, "Substitutional and interstitial carbon in wurtzite GaN," *Journal of Applied Physics*, vol. 92, no. 5, pp. 2575–2585, 2002.

[32] D. V. Lang, "Deep–level transient spectroscopy: A new method to characterize traps in semiconductors," *Journal of Applied Physics*, vol. 45, no. 7, pp. 3023–3032, 1974.

[33] A. Chantre, G. Vincent, and D. Bois, "Deep–level optical spectroscopy in GaAs," *Physical Review B*, vol. 23, pp. 5335–5359, May 1981.

[34] A. M. Armstrong, "Investigation of deep level defects in GaN:C, GaN:Mg and pseudomorphic AlGaN/GaN films," Ph.D. dissertation, Ohio State University, 2006.

[35] A. R. Arehart, "Investigation of electrically active defects in GaN, AlGaN, and AlGaN/GaN high electron mobility transistors," Ph.D. dissertation, Ohio State University, 2009.

[36] Z. Q. Fang, B. Claflin, D. C. Look, D. S. Green, and R. Vetury, "Deep traps in AlGaN/GaN heterostructures studied by deep level transient spectroscopy: Effect of carbon concentration in GaN buffer layers," *Journal of Applied Physics*, vol. 108, no. 6, 2010.

[37] A. R. Arehart, A. A. Allerman, and S. A. Ringel, "Electrical characterization of n–type $Al_{0.30}Ga_{0.70}N$ Schottky diodes," *Journal of Applied Physics*, vol. 109, no. 11, p. 114506, 2011.

[38] E. H. Nicollian and J. R. Brews, *MOS physics and technology*. Wiley Interscience Publications, 1982.

[39] X. Liu, H. C. Chin, L. S. Tan, and Y. C. Yeo, "In situ surface passivation of gallium nitride for metal–organic chemical vapor deposition of high–permittivity gate dielectric," *IEEE Transactions on Electron Devices*, vol. 58, no. 1, pp. 95–102, Jan 2011.

[40] B. L. Swenson and U. K. Mishra, "Photoassisted high–frequency capacitance–voltage characterization of the Si_3N_4/GaN interface," *Journal of Applied Physics*, vol. 106, no. 6, p. 064902, 2009.

[41] T. Marron, S. Takashima, Z. Li, and T. P. Chow, "Impact of annealing on ALD Al_2O_3 gate dielectric for GaN MOS devices," *Physica Status Solidi C*, vol. 9, no. 3-4, pp. 907–910, 2012.

[42] M. Miczek, C. Mizue, T. Hashizume, and B. Adamowicz, "Effects of interface states and temperature on the C–V behavior of metal/insulator/AlGaN/GaN heterostructure capacitors," *Journal of Applied Physics*, vol. 103, no. 10, p. 104510, 2008.

[43] C. Mizue, Y. Hori, M. Miczek, and T. Hashizume, "Capacitance–voltage characteristics of Al_2O_3/AlGaN/GaN structures and state density distribution at Al_2O_3/AlGaN interface," *Japanese Journal of Applied Physics*, vol. 50, p. 021001, 2011.

[44] H. A. Shih, M. Kudo, and T. K. Suzuki, "Analysis of AlN/AlGaN/GaN metal–insulator–semiconductor structure by using capacitance–frequency–temperature mapping," *Applied Physics Letters*, vol. 101, no. 4, pp. 0 435 011–0 435 014, 2012.

[45] R. Yeluri, B. L. Swenson, and U. K. Mishra, "Interface states at the SiN/AlGaN interface on GaN heterojunctions for Ga– and N–polar material," *Journal of Applied Physics*, vol. 111, no. 4, pp. 0 437 181–5, 2012.

[46] M. Capriotti, P. Lagger, C. Fleury, M. Oposich, O. Bethge, C. Ostermaier, G. Strasser, and D. Pogany, "Modeling small–signal response of GaN–based metal–insulator–semiconductor high electron mobility transistor gate stack in spill–over regime: effect of barrier resistance and interface states," *Journal of Applied Physics*, vol. 117, no. 2, 2015.

[47] P. Lagger, M. Reiner, D. Pogany, and C. Ostermaier, "Comprehensive study of the complex dynamics of forward bias induced threshold voltage drifts in GaN based MIS–HEMTs by stress/recovery experiments," *IEEE Transactions on Electron Devices*, vol. 61, no. 4, pp. 1022–1030, April 2014.

[48] A. Guo and J. A. del Alamo, "Positive–bias temperature instability (PBTI) of GaN MOSFETs," in *IEEE International Reliability Physics Symposium*, April 2015, pp. 6C.5.1–6C.5.7.

[49] M. Tapajna, R. J. T. Simms, M. Faqir, M. Kuball, Y. Pei, and U. K. Mishra, "Identification of electronic traps in AlGaN/GaN HEMTs using UV light–assisted trapping analysis," in *IEEE International Reliability Physics Symposium*, May 2010, pp. 152–155.

[50] G. Koley, V. Tilak, L. Eastman, and M. Spencer, "Slow transients observed in AlGaN/GaN HFETs: effects of SiN_x passivation and UV illumination," *IEEE Transactions on Electron Devices*, vol. 50, no. 4, pp. 886–893, april 2003.

[51] P. Lagger, P. Steinschifter, M. Reiner, M. Stadtmüller, G. Denifl, A. Naumann, J. Müller, L. Wilde, J. Sundqvist, D. Pogany, and C. Ostermaier, "Role of the dielectric for the charging dynamics of the dielectric/barrier interface in AlGaN/GaN based metal–insulator–seminconductor structures under forward gate bias stress," *Applied Physics Letters*, vol. 105, no. 3, p. 033512, 2014.

[52] P. Lagger, C. Ostermaier, G. Pobegen, and D. Pogany, "Towards understanding the origin of threshold voltage instability of AlGaN/GaN MIS-HEMTs," in *International Electron Device Meeting*, 2012, pp. 13.1.1–13.1.4.

[53] B. Kaczer, T. Grasser, J. Martin-Martinez, E. Simoen, M. Aoulaiche, P. J. Roussel, and G. Groeseneken, "NBTI from the perspective of defect states with widely distributed time scales," in *IEEE International Reliability Physics Symposium*, April 2009, pp. 55–60.

[54] M. Reiner, P. Lagger, G. Prechtl, P. Steinschifter, R. Pietschnig, D. Pogany, and C. Ostermaier, "Modification of native surface donor states in AlGaN/GaN MIS–HEMTs by fluorination: Perspective for defect engineering," in *IEEE International Electron Device Meeting*, 2015, pp. 35.5.1–35.5.4.

[55] S. A. Kukushkin, A. V. Osipov, V. N. Bessolov, B. K. Medvedev, V. K. Nevolin, and K. A. Tcarik, "Substrates for epitaxy of gallium nitride: new materials and techniques," *Reviews on Advanced Materials Science*, vol. 17, pp. 1–32, 2008.

[56] M. N. Polyanskiy, "Refractive index database," http://refractiveindex.info, accessed June 2016.

[57] *HF2 User Manual*, Zurich Instruments AG, Revision 30817, June 2015.

[58] *Agilent Impedance Measurement Handbook*, 4th ed., Agilent Technologies Inc., September 2013.

[59] *Spectral Irradiance*, Newport Corporation, Oriel Product Training, 2006.

[60] *Monochromators and Spectrographs*, Newport Corporation, Oriel Product Training, 2006.

[61] *Fiber Optics*, Newport Corporation, Photonics Technical Note Nr. 21, 2006.

[62] *Thorlabs SM1PD2A Photodiode specifications sheet*, Thorlabs, Rev. D, November 2012.

[63] E. H. Nicollian and A. Goetzberger, "The Si–SiO_2 interface: Electrical properties as determined by the metal–insulator–silicon conductance technique," *The Bell System Technical Journal*, vol. XLVI, no. 6, pp. 1055–1133, July–August 1966.

[64] H. El-Sissi and R. S. C. Cobbold, "Numerical calculation of the ideal C/V characteristics of nonuniformly doped MOS capacitors," *Electronics Letters*, vol. 9, pp. 594–596, 1973.

[65] L. Terman, "An investigation of surface states at a silicon/silicon oxide interface employing metal–oxide–silicon diodes," *Solid-State Electronics*, vol. 5, no. 5, pp. 285–299, 1962.

[66] R. Engel-Herbert, Y. Hwang, and S. Stemmer, "Comparison of methods to quantify interface trap densities at dielectric/III-V semiconductor interfaces," *Journal of Applied Physics*, vol. 108, no. 12, p. 124101, 2010.

[67] R. Stradiotto, G. Pobegen, C. Ostermaier, and T. Grasser, "Characterization of charge trapping phenomena at III–N/dielectric interfaces," *Solid-State Electronics*, vol. 125, pp. 142–153, 2016, extended papers selected from ESSDERC 2015.

[68] E. Bury, B. Kaczer, H. Arimura, M. Luque, L. Ragnarsson, P. Roussel, A. Veloso, S. Chew, M. Togo, T. Schram, and G. Groeseneken, "Reliability in gate first and gate last ultra–thin–EOT gate stacks assessed with CV–eMSM BTI characterization," in *IEEE International Reliability Physics Symposium*, April 2013, pp. GD.3.1–GD.3.5.

[69] T. Grasser, P.-J. Wagner, P. Hehenberger, W. Goes, and B. Kaczer, "A rigorous study of measurement techniques for negative bias temperature instability," *IEEE Transactions on Device and Materials Reliability*, vol. 8, no. 3, pp. 526–535, 2008.

[70] H. Reisinger, U. Brunner, W. Heinrigs, W. Gustin, and C. Schlünder, "A comparison of fast methods for measuring NBTI degradation," *IEEE Transactions on Device and Materials Reliability*, vol. 7, no. 4, pp. 531–539, 2007.

[71] B. Kaczer, T. Grasser, P. J. Roussel, J. Martin-Martinez, R. O'Connor, B. J. O'Sullivan, and G. Groeseneken, "Ubiquitous relaxation in BTI stressing – new evaluation and insights," in *Proceedings of the International Reliability Physics Symposium*, 2008, pp. 20–27.

[72] G. Pobegen and T. Grasser, "Efficient characterization of threshold voltage instabilities in SiC nMOSFETs using the concept of capture-emission-time maps," *Materials Science Forum*, vol. 740–742, pp. 757–760, 2013.

[73] T. Aichinger, M. Nelhiebel, S. Einspieler, and T. Grasser, "In situ polyheater – A reliable tool for performing fast and defined temperature switches on chip," *IEEE Transactions on Device and Materials Reliability*, vol. 10, pp. 3–8, 3 2010.

[74] W. Shockley and W. T. Read, "Statistics of the recombination of holes and electrons," *Physical Review*, vol. 87, pp. 835–842, 1952.

[75] R. N. Hall, "Electron–hole recombination in germanium," *Physical Review*, vol. 87, pp. 387–387, 1952.

[76] K. Huang and A. Rhys, "Theory of light absorption and non–radiative transitions in F–centres," *Proceedings of the Royal Society of London A: Mathematical, Physical and Engineering Sciences*, vol. 204, no. 1078, pp. 406–423, 1950.

[77] C. H. Henry and D. V. Lang, "Nonradiative capture and recombination by multiphonon emission in GaAs and GaP," *Physical Review B*, vol. 15, pp. 989–1016, Jan 1977.

[78] W. B. Fowler, J. K. Rudra, M. E. Zvanut, and F. J. Feigl, "Hysteresis and Franck–Condon relaxation in insulator–semiconductor tunneling," *Physical Review B*, vol. 41, pp. 8313–8317, Apr 1990.

[79] T. Grasser, "Analytic modeling of the bias temperature instability using capture/emission time maps," in *IEEE International Electron Device Meeting*, 2011, pp. 27.4.1–27.4.4.

[80] T. Grasser, H. Reisinger, P.-J. Wagner, F. Schanovsky, W. Goes, and B. Kaczer, "The time dependent defect spectroscopy (TDDS) for the characterization of the bias temperature instability." in *IEEE International Reliability Physics Symposium*, 2010, pp. 2A.2.1–2A.2.10.

[81] M. Kirton and M. Uren, "Noise in solid-state microstructures: a new perspective on individual defects, interface states and low-frequency (1/f) noise," *Advances in Physics*, vol. 38, no. 4, pp. 367–486, 1989.

[82] G. Pobegen, T. Aichinger, M. Nelhiebel, and T. Grasser, "Understanding temperature acceleration for NBTI," in *IEEE International Electron Device Meeting*, 2011, pp. 27.3.1–27.3.4.

[83] G. Pobegen and T. Grasser, "On the distribution of NBTI time constants on a long, temperature accelerated time scale," *IEEE Transactions on Electron Devices*, vol. 60, no. 7, pp. 2148–2155, 2013.

[84] A. A. Istratov and O. F. Vyvenko, "Exponential analysis in physical phenomena," *Review of Scientific Instruments*, vol. 70, no. 2, pp. 1233–1257, 1999.

[85] W. Von der Linden, "Maximum-entropy data analysis," *Applied Physics A*, vol. 60, no. 2, pp. 155–165, 1995.

[86] P. J. Steinbach, R. Ionescu, and C. R. Matthews, "Analysis of kinetics using a hybrid maximum-entropy/nonlinear-least-squares method: Application to protein folding," *Biophysical Journal*, vol. 62, pp. 2244–2255, 2002.

[87] E. T. Jaynes, "Information theory and statistical mechanics," *Physical Review*, vol. 106, pp. 620–630, May 1957.

[88] H. Reisinger, T. Grasser, W. Gustin, and C. Schlünder, "The statistical analysis of individual defects constituting NBTI and its implications for modeling DC– and AC–stress," in *IEEE International Reliability Physics Symposium*, 2010, pp. 2A.1.1–2A.1.9.

[89] T. Grasser, H. Reisinger, P.-J. Wagner, and B. Kaczer, "Time–dependent defect spectroscopy for characterization of border traps in metal–oxide–semiconductor transistors," *Physical Review B*, vol. 82, p. 245318, Dec 2010.

[90] W. Goes, Y. Wimmer, T. El-Sayed, G. Rzepa, M. Jech, A. L. Shluger, and T. Grasser, "Modeling of oxide defects in semiconductor devices: Connecting first–principles with rate equations," 2016, (to be published).

[91] W. Primak, "Kinetics of processes distributed in activation energy," *Physical Review*, vol. 100, pp. 1677–1689, 1955.

[92] G. Pobegen, "Degradation of electrical parameters of power semiconductor devices – Process influences and modeling," Ph.D. dissertation, Vienna University of Technology, 2013.

[93] S. Makram-Ebeid and M. Lannoo, "Quantum model for phonon–assisted tunnel ionization of deep levels in a semiconductor," *Physical Review B*, vol. 25, pp. 6406–6424, May 1982.

[94] D. G. Truhlar and A. Kohen, "Convex arrhenius plots and their interpretation," *Proceedings of the National Academy of Sciences*, vol. 98, no. 3, pp. 848–851, 2001.

[95] V. Huard, M. Denais, and C. Parthasarathy, "NBTI degradation: From physical mechanisms to modelling," *Microelectronics Reliability*, vol. 46, no. 1, pp. 1–23, 2006.

[96] R. Stradiotto, G. Pobegen, C. Ostermaier, M. Waltl, A. Grill, and T. Grasser, "Characterization of interface defects with distributed activation energies in GaN–based MIS–HEMTs," *IEEE Transactions on Electron Devices*, 2016, in review.

[97] M. Reiner, G. Denifl, M. Stadtmueller, R. Pietschnig, and C. Ostermaier, "Through–layer XPS investigations of the Si_3N_4/AlGaN interface," *Physica Status Solidi B*, 2016, available online: http://dx.doi.org/10.1002/pssb.201600143.

[98] M. Reiner, R. Pietschnig, and C. Ostermaier, "Tracking the effect of adatom electronegativity on systematically modified AlGaN/GaN schottky interfaces," *ACS Applied Materials and Interfaces*, vol. 7, no. 41, pp. 23.124–23.131, 2015.

[99] G. Lucovsky, "On the photoionization of deep impurity centers in semiconductors," *Solid State Communications*, vol. 3, pp. 299–302, 1965.

[100] R. Zeisel, "Optoelectronic properties of defects in diamond and AlGaN alloys," Ph.D. dissertation, Munich University of Technology, 2001.

[101] W. Goetz, N. M. Johnson, and D. P. Bour, "Deep level defects in Mg–doped, p–type GaN grown by metalorganic chemical vapor deposition," *Applied Physics Letters*, vol. 68, p. 3470, 1996.

[102] H. Hagemann, W. Gudat, and C. Kunz, "Optical constants from the far infrared to the x–ray region: Mg, Al, Cu, Ag, Au, Bi, C, and Al_2O_3," *Journal of the Optical Society of America*, vol. 65, no. 6, pp. 742–744, Jun 1975.

[103] L. Gao, F. Lemarchand, and M. Lequime, "Comparison of different dispersion models for single layer optical thin film index determination," *Thin Solid Films*, vol. 520, no. 1, pp. 501–509, 2011.

[104] A. D. Rakić, A. B. Djurišić, J. M. Elazar, and M. L. Majewski, "Optical properties of metallic films for vertical–cavity optoelectronic devices," *Applied Optics*, vol. 37, no. 22, pp. 5271–5283, Aug 1998.

[105] A. R. Arehart, A. C. Malonis, C. Poblenz, Y. Pei, J. S. Speck, U. K. Mishra, and S. A. Ringel, "Next generation defect characterization in nitride HEMTs," *Physica Status Solidi C*, vol. 8, no. 7–8, pp. 2242–2244, 2011.

[106] A. Sasikumar, A. Arehart, S. A. Ringel, S. Kaun, M. H. Wong, U. K. Mishra, and J. S. Speck, "Direct correlation between specific trap formation and electric stress–induced degradation in MBE–grown AlGaN/GaN HEMTs," in *Reliability Physics Symposium (IRPS), 2012 IEEE International*, April 2012, pp. 2C.3.1–2C.3.6.

Curriculum Vitae

Roberta Stradiotto

Born on April 22, 1987 in San Vito al Tagliamento (PN)
Rudolfweg 1, 9524 Villach – Österreich
+43 677 621 959 37

Nationality: Italian
roberta.stradiotto@gmail.com
linkedin.com/in/stradiottoroberta

Education

2013 – 2016 *Doctoral program in technical sciences* at Vienna University of Technology, Institute for Microelectronics in Vienna, Austria

Thesis: *Characterization of electrically active defects at III–N/dielectric interfaces*

Supervisors: Prof. Tibor Grasser and Dr. Gregor Pobegen

2009 – 2013 *M.Sc. in Solid State Physics* at University of Trieste, Italy

Thesis: *Experimental characterization of negative bias temperature instability in power MOSFETs*

Supervisors: Prof. Luciano Bosisio and Dr. Gregor Pobegen

Relevant coursework: Condensed Matter Physics, Spectroscopies, Statistics, Computational Physics

2006 – 2009 *B.Sc. in Physics* at University of Trieste, Italy

Thesis: *Characterization of the Interaction Potential of Adsorbates on Oriented Monocrystal Surfaces with Scanning Tunneling Microscopy* Supervisors: Prof. Giovanni Comelli and Dr. Carlo Dri

Relevant coursework: Physics of Electronic Devices

Programming and software skills

Programming	Certified LabVIEW Associate Developer (CLAD)
	Python, LaTeX, Matlab, Fortran 95
Office Tools	Microsoft Office and Open Office tools
Operating Systems	Windows OS, Linux

Publications

- R. Stradiotto, G. Pobegen and M. Nelhiebel, *Impact of copper and aluminum power metallization on the negative bias temperature instability*, IEEE International Integrated Reliability Workshop (IIRW), 2012
- R. Stradiotto, G. Pobegen, C. Ostermaier, and T. Grasser, *On the fly characterization of charge trapping phenomena at GaN/dielectric and GaN/AlGaN/dielectric interfaces using impedance measurements*, IEEE European Solid–State Device Research Conference (ESSDERC), 2015
- R. Stradiotto, G. Pobegen, C. Ostermaier, and T. Grasser, *Characterization of charge trapping phenomena at III–N/dielectric interfaces*, Solid-State Electronics, vol. 125, pp. 142–153, 2016, extended papers selected from ESSDERC 2015
- R. Stradiotto, G. Pobegen, C. Ostermaier, Michael Waltl, Alexander Grill and T. Grasser, *Characterization of Interface Defects with Distributed Activation Energies in GaN–based MIS–HEMTs*, submitted to Transactions on Electron Devices (in review)
- 10+ talks and poster presentations in the course of the doctoral program

Language skills

Italian	mother tongue	German	B1 level
English	full professional proficiency		

Personal Interests

Austrian alpine club (ÖAV) affiliate
Mountain sports: hiking, climbing
Team sport player: volleyball, beach–volley, soccer
Kendo practitioner
Calligraphy amateur